2MW

Computational Study of Nonlinear Plasma Waves

by

Y. Matsuda

March 1974

SUIPR Report No. 567

NSF Grant GK 32788X
and
NASA Grant NGL 05-020-176

INSTITUTE FOR PLASMA RESEARCH
STANFORD UNIVERSITY, STANFORD, CALIFORNIA

COMPUTATIONAL STUDY OF NONLINEAR PLASMA WAVES

by

Y. Matsuda

NSF Grant GK 32788X

and

NASA Grant NGL 05-020-176

SU-IPR Report No. 567

March 1974

Institute for Plasma Research
Stanford University
Stanford, California 94305

COMPUTATIONAL STUDY OF NONLINEAR PLASMA WAVES

by

Y. Matsuda
Institute for Plasma Research
Stanford University
Stanford, California 94305

ABSTRACT

In this work, a low-noise plasma simulation model is developed, and applied to a series of linear and nonlinear problems associated with electrostatic wave propagation in a one-dimensional, collisionless, Maxwellian plasma, in the absence of magnetic field. It is demonstrated that use of the hybrid simulation model allows economical studies to be carried out in both the linear and nonlinear régimes with better quantitative results, for comparable computing time, than can be obtained by conventional particle simulation models, or direct solution of the Vlasov equation.

The characteristics of the hybrid simulation model itself are first investigated, and it is shown to be capable of verifying the theoretical linear dispersion relation at wave energy levels as low as 10^{-6} of the plasma thermal energy. Having established the validity of the hybrid simulation model, it is then used to study the nonlinear dynamics of a monochromatic wave, sideband instability due to trapped particles, and satellite growth. The simulations are performed in parameter ranges such that detailed quantitative comparison with available theories is possible. In particular, the transition from time-asymptotic amplitude oscillation to continuous Landau damping is investigated for a monochromatic wave as the initial wave amplitude is varied. The results,

which include a small nonlinear frequency shift, compare favorably with theory. The study of sideband instability confirms the applicability of quasilinear theory at short times, and parametric coupling theory in the time-asymptotic limit, and reproduces features analogous to those observed in laboratory experiments. The growth of a satellite wave in the presence of a large amplitude wave and a test wave is shown to be explicable by a simple theory involving slow modulation of the large amplitude wave.

It is concluded that the hybrid simulation model constitutes a reliable and economical tool for use in the study of plasma phenomena. It should be widely applicable to the testing of predictions of linear and nonlinear theories, and the description of more complicated situations which are not amenable to analysis.

CONTENTS

CONTENTS (Contd.)

TABLE

ILLUSTRATIONS

ILLUSTRATIONS (Contd.)

ILLUSTRATIONS (Contd.)

ILLUSTRATIONS (Contd.)

ILLUSTRATIONS (Contd.)

ILLUSTRATIONS (Contd.)

SYMBOLS

Symbol		Page where first used
	(1) Latin Alphabet	
a	size of a Gaussian cloud	32
a_i	fractional length of cloud occupying the i-th cell	28
a_{mn}	expansion coefficients of F_n	21
$a_{i,j}$	fractional area of cloud occupying the (i,j) cell	29
A	total area of cloud	29
A	dummy variable	54
A	quantity defined by Eq. (6.8)	136
$A_p^{(n)}$	Lagrangian coefficients	142
B	quantity defined by Eq. (6.8)	136
$\underset{\sim}{B}$	magnetic field vector	3
c	quantity defined by Eq. (6.3)	134
C_n	quantity defined by Eq. (2.21)	16
D	diffusion rate	61
e	magnitude of electron charge	24
E	electric field	4
E	dimensionless electric field	15
E	complete elliptic integral of the second kind	88
$\underset{\sim}{E}$	electric field vector	3
E_0	wave electric field amplitude	74
E_1	perturbed electric field	115
E_i	electric field at the i-th grid point	29

SYMBOLS (Contd.)

Symbol		Page where first used
E_n	electric field at the n-th time-step	24
E_n	dimensionless Fourier component of electric field	16
E_m	electric field of modulated wave	135
E_u	electric field of main wave	134
E_u	electric field defined by Eq. (6.8)	136
$\underset{\sim}{E}_{ij}$	electric field vector at the (i,j) grid point . .	29
E_p^n	$E(p\Delta x, n\Delta t)$	13
$\langle E_k \rangle$	electric field fluctuation amplitude	43
f	velocity distribution	4
f	dimensionless velocity distribution	15
$\tilde{f}$	smoothed velocity distribution	18
f_0	initial velocity distribution	40
f_1	perturbed velocity distribution	115
f_i	velocity distribution of the i-th particle species	3
f_j	mass of particle j	60
f_p^n	$f(p\Delta x, n\Delta t)$	12
$f_{p,q}^n$	$f(p\Delta x, q\Delta v, n\Delta t)$	13
$\langle f \rangle$	averaged velocity distribution	112
F	force	29
F	complete elliptic integral of the first kind . .	86
$\underset{\sim}{F}$	force vector	29
F_i	force on particle i	35

Symbol		Page where first used
F_j	velocity distribution defined by Eq. (3.6)	55
F_c	force in cloud plasma	40
F_p	force in point particle plasma	40
F_n	dimensionless transformed velocity distribution . .	16
F_{ij}	force on particle i due to particle j	33
g_m	constants	21
h	cell length	38
h_m	Hermite polynomials defined by Eq. (2.28)	19
H	particle size (one dimension)	28
H	Fourier transform of f	61
$\tilde{H}$	Fourier transform of $\tilde{f}$	61
$\tilde{H}_m$	quantity defined by Eq. (3.17)	61
i	$(-1)^{1/2}$	16
I_R^T	quantity defined by Eq. (4.3)	87
I_R^{UT}	quantity defined by Eq. (4.4)	87
$\underset{\sim}{J}$	current density	3
J_c	current density in cloud plasma	40
J_p	current density in point particle plasma	40
k	wavenumber	4
k_0	dimensionless fundamental wavenumber	16
k_0	wavenumber of the main wave	98
k_1	wavenumber of small amplitude wave	127
k_2	wavenumber of satellite wave	127

SYMBOLS (Contd.)

Symbol		Page where first used
k_ℓ	$k - 2\pi\ell/\Delta x$	41
k_m	maximum wavenumber in the system	52
k_B	Boltzmann constant	43
K	quantity defined by Eq. (2.66)	41
L	system length	33
L	dimensionless system length	16
$\mathcal{L}$	Lagrangian	36
m_e	electron mass	24
m_i	mass of the i-th particle species	3
n	number density	46
n_j	first order density of the j-th beam	54
N	number of simulation particles	9
N_e	number of electron sheets in (0,x)	6
N_i	number of ion sheets in (0,x)	6
N_j	zeroth order density of the j-th beam	54
N_s	number of time-steps after which the smoothing operation is repeated	64
N_T	number of trapped particles in a potential well .	120
q_i	charge of the i-th particle species	3
Q	$\exp\{-\pi F[(1-\kappa^2)^{1/2}]/F(\kappa)\}$	86
Q_0	$Q(\kappa_0)$	87
S	form factor	34
S	shape factor	34

Symbol		Page where first used
S_e	form factor defined by Eq. (2.66)	41
Si	function defined by Eq. (4.2)	87
t	time variable	3
t	dimensionless time variable	15
t_n	$n\Delta t$	12
T	temperature	43
v	velocity	4
v	dimensionless velocity	15
$\underset{\sim}{v}$	velocity vector	3
v_1	minimum velocity in the system	49
v_2	maximum velocity in the system	49
v_i	$i\Delta v$	141
v_i	velocity of the i-th particle species	10
$\underset{\sim}{v}_i$	velocity vector of the i-th particle species . .	10
v_j	first order velocity of the j-th beam	54
$v_{n+1/2}$	particle velocity at $\left(n + \frac{1}{2}\right)$th time-step	24
v_p	wave phase velocity	76
v_t	electron thermal velocity	15
$\langle v^n \rangle$	n-th order moment of f	141
$\langle \tilde{v}^n \rangle$	n-th order moment of $\tilde{f}$	141
V_j	zeroth order velocity of the j-th beam	54
w	particle velocity in wave frame	113
w*	velocity defined by Eq. (5.13)	112

SYMBOLS (Contd.)

Symbol		Page where first used
w_x	weighting function in coordinate-space	18
w_v	weighting function in velocity-space	18
$\langle w \rangle$	averaged velocity defined by Eqs. (5.10) and (5.12)	112
$\langle w_0 \rangle$	quantity defined by Eqs. (5.9) and (5.11)	112
W	Fourier transform of $w(v)/\Delta v$	61
W	first integral of motion	111
x	coordinate	4
x	dimensionless coordinate	15
$\underset{\sim}{x}$	coordinate vector	3
x_i	position of the i-th particle species	10
$\underset{\sim}{x}_i$	position vector of the i-th particle species . . .	10
x_n	particle position at the n-th time-step	24
x_n	position of a particle in the n-th potential well	120
x_p	$p\Delta x$	12
x_{Gi}	nearest grid point location	34
x_{n0}	initial position of the n-th potential well	120
X	particle trajectory	36
X_ℓ	basis functions	37
y	dimensionless reciprocal of velocity	16
z	$\omega/(2^{1/2}kv_t)$	56
Z	plasma dispersion function	40
Z_{mn}	transformed velocity distribution	19

Symbol		Page where first used
	(2) Greek Alphabet	
α	$[ekE(t)/m_e]^{1/2}$	87
α_j	quantity defined by Eq. (3.11)	56
α_n	generalized coordinates	37
β_j	quantity defined by Eq. (3.11)	56
β_L	$\gamma_L/(\partial\omega/\partial k)$	123
γ	damping rate	86
γ	sideband growth rate	123
γ_0	constant	124
γ_ℓ	generalized coordinates	37
γ_L	Landau damping rate	75
δ	variation	37
δ	beam spacing	55
δv	width of the bump in velocity distribution	119
$\delta\omega$	nonlinear frequency shift	92
δv_j	velocity increment from the j-th grid point	141
δx_i	particle position relative to x_{Gi}	34
$\delta(\ )$	Dirac delta-function	38
Δk	wavenumber separation between main and test waves	134
Δt	time-step	11
Δt	dimensionless time-step	18
Δv	velocity grid size	13
Δx	spatial grid size	11

SYMBOLS (Contd.)

Symbol		Page where first used
Δy	grid size in y-space	18
$\Delta\omega$	sideband peak frequency separation	123
Δv_i	velocity perturbation of particle i	65
Δx_i	displacement of particle i	65
ϵ	perturbation amplitude	65
ϵ_0	free space permittivity	3
ϵ_p	plasma permittivity	40
ζ	quantity defined by Eq. (5.7)	111
η	$1/\kappa$, trapping parameter	113
θ	phase modulation defined by Eq. (6.3)	134
κ	quantity defined by Eq. (2.66)	41
κ	trapping parameter	112
λ_0	wavelength of main wave	120
λ_B	$\omega/k\omega_B$	123
λ_D	electron Debye length	15
ξ	quantity defined by Eq. (5.7)	111
ξ_0	initial value of ξ	111
ξ_j	$j\delta/(2^{1/2}v_t)$	56
ρ	charge density	3
ρ_0	background charge density	39
ρ_i	charge assigned to the i-th grid point	28
ρ_i	particle charge distribution	32
ρ_c	charge of cloud	28

SYMBOLS (Contd.)

Symbol		Page where first used
ρ_c	charge density in cloud plasma	40
ρ_p	charge density in point particle plasma	40
$\rho_{i,j}$	charge assigned to the (i,j) grid point	29
ρ_p^n	$\rho(p\Delta x, n\Delta t)$	13
σ	surface charge density of sheet	6
τ	$1/\omega_B$	86
τ_d	delay time	119
τ_s	time defined by Eq. (3.21)	63
τ_R	recurrence time	59
ϕ	electrostatic potential	13
ϕ_p^n	$\phi(p\Delta x, n\Delta t)$	13
Φ_n	basis functions	37
ω	angular frequency	40
ω_0	frequency of main wave	111
ω_1	frequency of test wave	126
ω_2	frequency of satellite wave	126
ω_j	$\alpha_j + i\beta_j$	56
ω_p	plasma frequency	15
ω_B	bounce frequency	74
ω_L	linear frequency	85
ω_T	frequency defined by Eq. (5.20)	120
Ω	$\omega - kv_p$	121
Ω	quantity defined by Eq. (6.4)	134

ACKNOWLEDGMENTS

I would like, first of all, to thank Prof. F. W. Crawford, my research adviser, who has patiently guided and supported me in many ways such as suggesting many key ideas and helping organize this dissertation. It is also a pleasure to express my appreciation to Dr. S. A. Self for his helpful criticism during the course of this work and reading the manuscript, and to Prof. L. Padulo for reading and commenting on the manuscript. Thanks are also due to Dr. K. J. Harker, who helped me in resolving problems concerning satellite growth, and Dr. A. L. Brinca for stimulating discussions on sideband instability and other topics. I am grateful to Prof. O. Buneman for his invaluable advice in the area of computer simulation, and Dr. C. W. Barnes for introducing me to the subleties of computer techniques. I am much indebted to Ms. Jane Johnston, who expertly typed this dissertation. My final, deepest gratitude goes to my wife Kazuyo for her understanding and encouragement at every stage of this work.

1. INTRODUCTION

This dissertation is concerned with computer simulation of electron plasma waves in a Maxwellian plasma, in the absence of magnetic field. The aims of our simulations are, first, to develop an economical low-noise simulation technique, and second, to apply it to the study of linear and nonlinear wave phenomena in a one-dimensional plasma with periodic boundary conditions. In what follows, emphasis has been placed on simulations for wave and plasma parameters comparable with those assumed in available theories, and accessible in laboratory experiments.

There are two distinctly different approaches to the simulation of plasma dynamics: first is the use of a particle simulation model in which individual charged particles are followed, and second is direct numerical solution of the Vlasov equation describing the charged particle velocity distribution function. The particle simulation model has the disadvantage that the fluctuation level is usually several orders of magnitude higher than in an actual plasma. This stems from the fact that it is not feasible to follow on the computer the dynamics of as many particles as there are in a plasma. This fluctuation not only gives rise to nonphysical effects, but also makes it difficult to study linear and weakly nonlinear phenomena. This is particularly unfortunate since most of the nonlinear theories to date are based on an expansion method which is valid only in weakly nonlinear cases. Consequently, they cannot be clearly validated by computer simulation, nor vice versa. Direct solution of the Vlasov equation is subject to numerical instability associated with the free-streaming term in the Vlasov equation. This tends to limit application of the method to short-time simulations.

It will be shown in this work that a hybrid approach, combining features of the particle simulation model and Vlasov approach, can avoid the foregoing difficulties, and provide reliable results in both the linear and nonlinear régimes.

In Section 2, we review various types of particle simulation models, and consider numerical solution of the Vlasov equation. The hybrid simulation model is described and analyzed in Section 3, and results of test runs in the linear régime are presented to demonstrate the feasibility of high quality simulation. In Section 4, the nonlinear dynamics of a monochromatic plasma wave are studied as our first application of the model. Section 5 presents a comprehensive study of sideband instability in which a large amplitude wave and its sidebands interact through the trapped particles to cause growth of the sideband waves. In Section 6, satellite growth due to nonlinear interaction between the lower and upper sidebands is studied. Some conclusions on the validity and applicability of the hybrid simulation approach are given in Section 7.

2. COMPUTER APPLICATIONS TO PLASMA PHYSICS

2.1 The Vlasov Equation and Simulation Approaches

There are two ways of approaching problems in plasma physics by use of computers. One is to use the Vlasov equation, describing the velocity distribution function of smeared-out charges, combined with the Maxwell equations. The other is to use a particle simulation approach dealing with discrete charges, combined with the Newton equation and the Maxwell equations.

The Vlasov equation,

$$\frac{\partial f_i}{\partial t} + \underset{\sim}{v} \cdot \frac{\partial f_i}{\partial \underset{\sim}{x}} + \frac{q_i}{m_i} (\underset{\sim}{E} + \underset{\sim}{v} \times \underset{\sim}{B}) \cdot \frac{\partial f_i}{\partial \underset{\sim}{v}} = 0 , \tag{2.1}$$

coupled with the Maxwell equations,

$$\begin{aligned} \nabla \times \underset{\sim}{B} &= \underset{\sim}{J} + \frac{\partial \underset{\sim}{E}}{\partial t} , \qquad \nabla \cdot \underset{\sim}{B} = 0 , \\ \nabla \times \underset{\sim}{E} &= - \frac{\partial \underset{\sim}{B}}{\partial t} , \qquad \nabla \cdot \underset{\sim}{E} = \frac{\rho}{\epsilon_0} , \end{aligned} \tag{2.2}$$

and equations for current and charge densities,

$$\underset{\sim}{J} = \sum_i \int q_i \underset{\sim}{v} f_i \, d\underset{\sim}{v} , \qquad \rho = \sum_i \int q_i f_i \, d\underset{\sim}{v} , \tag{2.3}$$

is capable of describing the collective behavior of collisionless plasmas. Here, f_i is the distribution function of the i-th charged particle species, $\underset{\sim}{E}$ and $\underset{\sim}{B}$ are the electric and magnetic fields, including both time-varying and static fields, q_i and m_i are the particle charge and mass, and ϵ_0 is the permittivity of free space. It is important to note that the Vlasov equation does not include

discrete particle encounters and thermal fluctuations, whereas discrete charge models automatically include such effects.

In the Vlasov approach, the major task is to solve Eqs. (2.1)-(2.3) numerically, subject to appropriate initial and boundary conditions. This line has been pursued by Knorr,[1] Kellogg,[2] and Armstrong.[3] These authors solved the Vlasov equation,

$$\frac{\partial f_i}{\partial t} + v \frac{\partial f_i}{\partial x} + \frac{q_i}{m_i} E \frac{\partial f_i}{\partial v} = 0 \ , \tag{2.4}$$

and the Poisson equation,

$$\frac{dE}{dx} = \frac{1}{\epsilon_0} \sum_i \int q_i f_i dv \ , \tag{2.5}$$

in the study of Landau damping,[1,3] and the two-stream instability at large amplitudes,[2] in a one-dimensional plasma. However, all of these workers encountered the serious computational difficulty which stems from the nature of the Vlasov equation, i.e., the tendency to develop steep gradients in phase-space as time increases. To appreciate this, consider the following simplified equation,

$$\frac{\partial f}{\partial t} + v \frac{\partial f}{\partial x} = 0 \ , \tag{2.6}$$

which describes free-streaming particles. By taking a single Fourier component of f, it is seen from Eq. (2.6) that the distribution function always has a part of the form, exp (ikvt). This represents velocity-space oscillation which becomes finer and finer as time increases. It is due to conversion of the space oscillations of the initial distribution function into velocity oscillations by the shear motion in phase-space.

Since the gradient of the velocity distribution function increases with time, a progressively finer grid in phase-space will be required for accurate computation. This is the case for the difference method used by Kellogg.[2] In the case of the expansion method used by Knorr[1] and Armstrong,[3] the development of large derivatives of f requires a large number of expansion terms to be used. The number of grid points, or the number of expansion terms allowable, is limited by computer capacity and economic considerations. The finite grid size, or truncated expansion, consequently sets limits on the elapsed time during which the simulation is accurate.

Direct solution of the Vlasov equation gives accurate quantitative results in both the linear and nonlinear régimes only until it approaches the limit mentioned above. The particle simulation model, on the other hand, is free from such time limitations, and is therefore better suited for nonlinear problems.

Computer simulation seems to have been introduced into the field of plasma physics by Buneman, who used the charge sheet model to solve a nonlinear problem.[4] In particular, he followed the development of electron-ion two-stream instability to show that rapid randomization of the initially coherent streaming energy takes place in a cold collisionless plasma. Soon afterwards, Dawson investigated the thermalization and ergodic behavior of a system of charge sheets and found that statistical mechanics can be applied to the system.[5] He then studied the properties of the one-dimensional plasma in thermal equilibrium, finding good agreement with theoretical results based on statistical mechanics. Since then, the simulation model has been improved and

applied to a wide variety of plasma problems which are not analytically tractable. Computer codes have been written for both electrostatic and electromagnetic cases, with or without external magnetic field, and in one, two, or three dimensions. Relativistic effects have also been included.

In the charge sheet model, electrons or ions are considered to form infinitesimally thin charge sheets, extending to infinity in two dimensions, and moving only in the direction perpendicular to the plane of the sheet. They are assumed to pass freely through each other. Such a charge sheet generates electric field, E, which is discontinuous at the sheet position, and takes constant values on each side, as shown in Fig. 2.1. For a given boundary value, the electric field created by many charge sheets can be calculated at any point by a simple algorithm. For example, suppose the electric field to be given at $x = 0$. The algorithm used to find the electric field at x is

$$E(x) = E(0) + \frac{\sigma}{\epsilon_0} (N_i - N_e) , \qquad (2.7)$$

where N_i and N_e are the number of ion and electron sheets in the interval $(0,x)$, and σ is the (positive) surface charge density of the sheet (see Fig. 2.2). Note that the electric field is discontinuous at the sheet position, and is not defined by Eq. (2.7). The electric field at the sheet position is taken at the middle of the jump shown by a cross in Fig. 2.2. Using the electric field thus computed, the Newton equation of motion for a sheet is integrated to find its position and velocity after a small time-step. From the new distribution of the charge sheets, the electric field can again be calculated, and

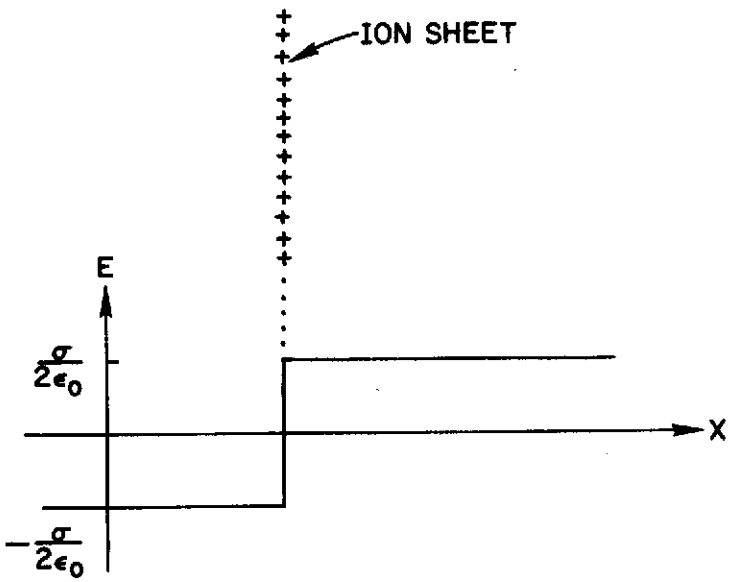

FIG. 2.1. Electric field generated by an isolated charge sheet. σ is the surface charge density.

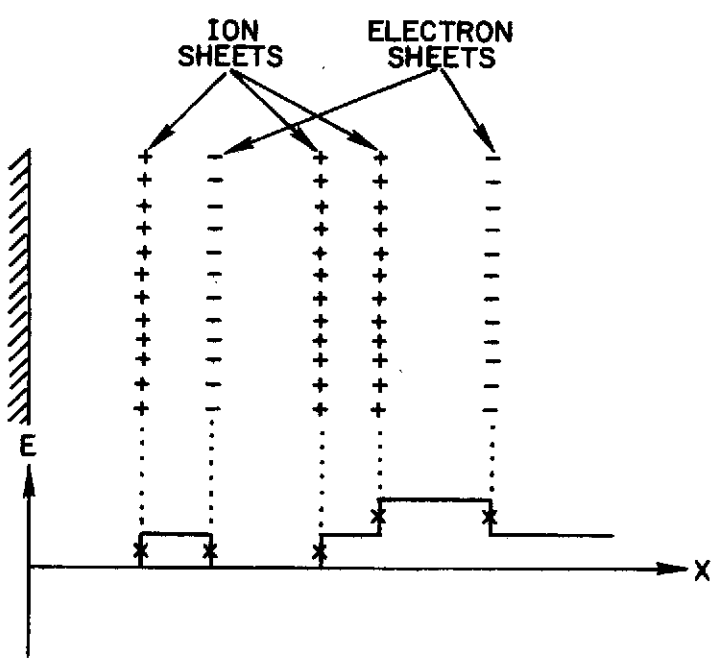

FIG. 2.2. Electric field calculated by Eq. (2.1). $E(0) = 0$ is assumed.

substituted in the Newton equation. Starting with a given initial distribution of charge sheets, the behavior of the system can thus be followed in time. When a particle leaves one end of the system, it is reintroduced at the other end, with the same velocity that the particle had upon leaving the system. This imposes a periodic boundary condition. Another condition sometimes used is that of a reflecting boundary: a particle rebounds elastically at the ends of the system. This boundary condition can be used for study of standing waves.

In simulations of phenomena occurring on time scales for which only electron motions need be considered, the positive ions behave as an immobile neutralizing background. There are two ways of treating the ions in this case. One is to place ion sheets equidistantly in space. The other is to spread the positive charge uniformly.[5] In the latter case, the electric field resulting from equally spaced electron sheets is as shown in Fig. 2.3.

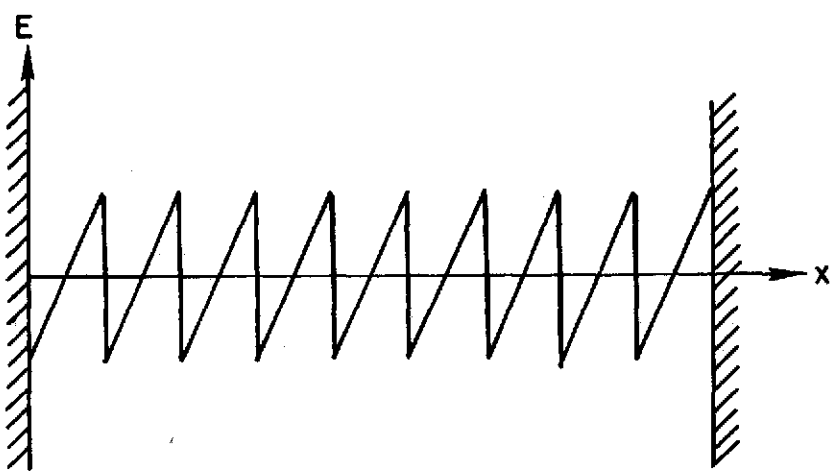

FIG. 2.3. Electric field resulting from equally spaced electron sheets and uniformly distributed positive ion charge.

Simple as it is in principle, the sheet model described above is capable of simulating a wide variety of electrostatic, one-dimensional problems. However, since the number of particles that can be handled on modern computers is still many orders of magnitude smaller than the numbers of charged particles in experimental plasmas, the fluctuations appearing in the averaged quantities, such as the electric field and mean particle velocity, are much larger in a simulation model than in the plasma simulated. The fluctuation amplitudes can be reduced by increasing the number of simulation particles, N , but they decrease only as $N^{-1/2}$. Consequently, the energy of the fluctuations in a simulation plasma is typically many orders of magnitude higher than that in the plasma simulated. Since the enhanced fluctuations may cause nonphysical or exaggerated effects, considerable effort has been made to reduce the fluctuations without increasing the number of particles. This topic will be discussed in Section 2.3 in connection with various more sophisticated models developed from the simple charge sheet model just described.

In two-dimensional problems, infinitely long charged rods are postulated, instead of charge sheets, to allow simulation in two dimensions. In three dimensions, the particles are represented by point charges. The electric fields created by isolated rod and point particles are shown in Fig. 2.4.

In electromagnetic problems, for which the time-varying magnetic field is important, a model must be employed which properly solves the equation of charge particle motion, including a Lorentz force term,

$$\frac{d\underset{\sim}{v}_i}{dt} = \frac{q_i}{m_i}\left(\underset{\sim}{E} + \underset{\sim}{v}_i \times \underset{\sim}{B}\right) , \qquad \frac{d\underset{\sim}{x}_i}{dt} = \underset{\sim}{v}_i , \tag{2.8}$$

and the Maxwell equations [Eq. (2.2)], where subscript i denotes the particle species. The current and charge densities are obtained from knowledge of the positions and velocities of the particles.

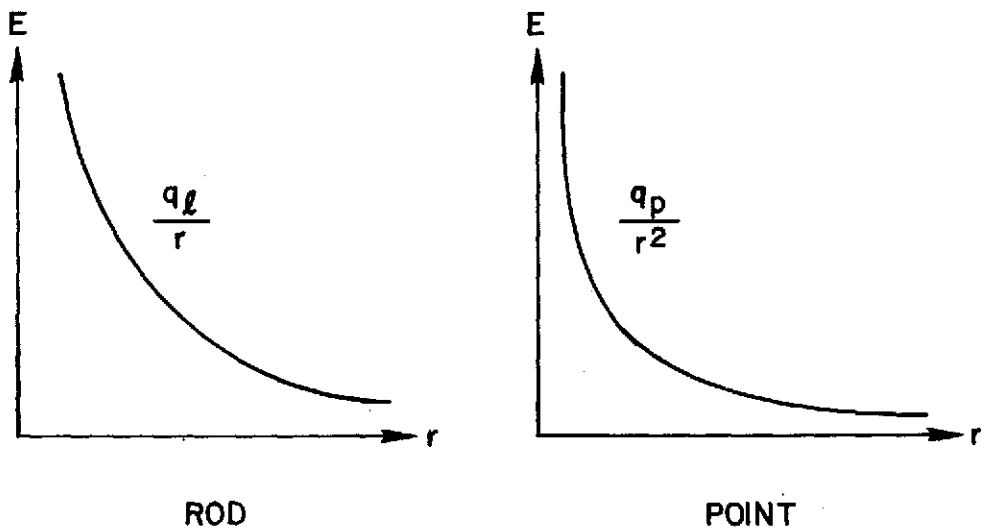

FIG. 2.4. Electric field, E , vs. radial distance, r.
(a) Rod charge. q_ℓ is charge per unit length.
(b) Point charge. q_p is charge.

In what follows, we shall restrict ourselves to electrostatic phenomena, and concentrate on a one-dimensional model without external magnetic field. Therefore, we need only consider the one-dimensional equation of motion,

$$\frac{dv_i}{dt} = \frac{q_i}{m_i} E , \qquad \frac{dx_i}{dt} = v_i , \tag{2.9}$$

and the Poisson equation,

$$\frac{dE}{dx} = \frac{\rho}{\epsilon_0} . \tag{2.10}$$

Having considered the two approaches, it is an attractive possibility to develop a method which possesses the desirable features of both of them. Specifically, it should provide a very low fluctuation level, and retain particle discreteness effects, so that it will be possible to study both small amplitude waves and large amplitude nonlinear phenomena. Such a 'hybrid' approach has been proposed by Denavit.[6] The main purpose of our work has been to develop this method, and to apply it to the study of nonlinear phenomena associated with large amplitude electron plasma waves. Section 3 is devoted to analytical and numerical study of its characteristics.

Various methods of solving the Vlasov equation are described in Section 2.2. Detailed descriptions of a variety of particle simulation models are given in Section 2.3.

2.2 Solution of the Vlasov Equation

2.2.1 Finite Difference Methods

Since the Vlasov equation is a partial differential equation, probably the most straightforward approach is to approximate it by a finite difference equation, and to solve it numerically on a computer. This is simple, because it is a direct integration scheme, but lengthy, because a large number of grid points are necessary.

The Vlasov equation is nonlinear since the electric field, E, is a function of the distribution function, f. It is a hyperbolic equation with variable coefficients. From the theory of numerical analysis, it is known that a finite difference method for a linear, hyperbolic, partial differential equation with constant coefficients is stable for appropriate choice of grid size, Δt and Δx, and convergent to the

exact solution in the limit $\Delta t \to 0$, $\Delta x \to 0$. However, there is no guarantee of stability or convergence in the nonlinear, variable coefficient case.

Consider the difference equation corresponding to Eq. (2.6) on a grid with $x_p = p\Delta x$, $t_n = n\Delta t$, where p and n are integers, and $f_p^n = f(x_p, t_n)$. A simple difference approximation to Eq. (2.6) is obtained by the substitutions

$$\frac{\partial f}{\partial t} \to \frac{f_p^{n+1} - (f_{p+1}^n + f_{p-1}^n)/2}{\Delta t} , \qquad \frac{\partial f}{\partial x} \to \frac{f_{p+1}^n - f_{p-1}^n}{2\Delta x} . \tag{2.11}$$

This yields

$$f_p^{n+1} = \frac{f_{p+1}^n + f_{p-1}^n}{2} - \frac{\Delta t}{\Delta x} v \left(\frac{f_{p+1}^n - f_{p-1}^n}{2} \right) , \tag{2.12}$$

which is known to be stable for $|v\Delta t/\Delta x| < 1$.[7] The error in this scheme is of second order in Δt and Δx . It should be noted that the stability criterion is derived assuming that the coefficient, i.e. v is constant, so this must be considered as a local condition in velocity-space.

A popular method of calculation, because it gives higher order accuracy, is the "leap-frog" scheme given by

$$f_p^{n+1} = f_p^{n-1} - \frac{\Delta t}{\Delta x} v \left(f_{p+1}^n - f_{p-1}^n \right) , \tag{2.13}$$

which has the same stability condition $|v\Delta t/\Delta x| < 1$. The error in this scheme is of third order in Δt and Δx . However, this has the disadvantage of being a three-time-level equation. A similar leap-frog scheme is used for advancing particles in the particle simulation models described in Section 2.3.

The nonlinear term, $E\partial f/\partial v$, in the Vlasov equation can be treated in a similar way to the $v\partial f/\partial x$ term. However, when the $E\partial f/\partial v$ term is included, the difference equation may not be stable, even if the free-streaming part is approximated by a stable difference scheme. In studying two-stream instability for electrons streaming through mobile ions, Kellogg used a stable difference scheme for Eq. (2.6), but did not succeed in finding a stable scheme for Eq. (2.4), because of the effects of the nonlinear term, $E\partial f/\partial v$.[2] Various more sophisticated schemes have been pursued to minimize and suppress the effects of the numerical instability, including smoothing of the distribution function, and have been used successfully.[8,9] However, no general method of circumventing this instability has been established; it depends very much on the nature of the problem under study.

The difference equation for the Poisson equation [Eq. (2.5)] is

$$E^n_{p+1} = E^n_p + \frac{\Delta x}{\epsilon_0} \sum_i \Delta v \sum_q f^n_{p,q} \quad , \tag{2.14}$$

where Δv is the velocity grid spacing, $E^n_p = E(p\Delta x, n\Delta t)$, $f^n_{p,q} = f(p\Delta x, q\Delta v, n\Delta t)$, and the subscript i in f , denoting particle species, has been suppressed. For certain boundary conditions, it is convenient to solve

$$\frac{d^2\phi}{dx^2} = - \frac{\rho}{\epsilon_0} \quad , \tag{2.15}$$

where $E = - d\phi/dx$. A difference approximation to Eq. (2.15) is

$$\phi^n_{p+1} - 2\phi^n_p + \phi^n_{p-1} = - \frac{(\Delta x)^2}{\epsilon_0} \rho^n_p \quad . \tag{2.16}$$

The solutions of Eqs. (2.14) and (2.16) are straightforward, and cause no numerical instability.

It is worth noting that the difference schemes mentioned above are "explicit" schemes, i.e., all the variables at the n-th time-step are expressed in terms of the variables at the (n-1)th time-step, or earlier. In an "implicit" scheme, a variable at the n-th time-step is expressed in terms of other variables at the same time-step and earlier. The use of the implicit scheme may make the difference equations stable, but since a set of simultaneous linear equations has to be solved at every time-step it may be prohibitively expensive.

2.2.2 Transform Methods

Transform methods constitute an obvious alternative to the finite difference method. Transformation of the variables to a different set offers the possibility of avoiding some of the difficulties encountered in the finite difference method. Expansion in terms of orthonormal eigenfunctions is a well-known mathematical technique, Fourier transformation being one of the simplest and most extensively used.

Among the advantages of using the transform method are the elimination of the partial derivatives in x and v, and of integration in v. The resulting algebraic operations are much simpler to deal with numerically than differentiations and integrations. Another advantage is a relief from numerical instability. This depends on the choice of transformation, and there is a possibility that a different type of numerical instability is introduced. The transform method reduces Eqs. (2.4) and (2.5) to a set of ordinary differential equations in

time, or to a simpler set of partial differential equations, depending on the transformation employed. The ordinary differential equations can be solved much more easily than the partial differential equations. Even when one of the partial differentiations is left in the equations, they are easier to handle from a numerical stability point of view than the original equations.

In the following, three methods will be described. They are the Fourier-Fourier method, the Fourier-Hermite method, and the Power Series Expansion method. For simplicity, we shall consider a one-dimensional, electrostatic, homogeneous plasma, without externally applied fields, and assume that the ions form an immobile, neutralizing, background charge. For the rest of the present subsection, we shall use dimensionless units for length, velocity, time, etc. Equations (2.4) and (2.5) can then be written as

$$\frac{\partial f}{\partial t} + v \frac{\partial f}{\partial x} - E \frac{\partial f}{\partial v} = 0 , \qquad \frac{dE}{dx} = (1 - \int f dv) , \tag{2.17}$$

where x is in units of the Debye length, λ_D , v is in units of the thermal velocity, v_t , t is in units of the reciprocal of the plasma frequency, $1/\omega_p$, and E and f are also dimensionless variables.

Fourier-Fourier Expansion[1,10]: The distribution function, f , is expanded in a Fourier series in x , and Fourier transformation in v is carried out according to the following relations

$$f(x,v,t) = \frac{1}{2\pi} \sum_{n=-\infty}^{\infty} \exp(ink_0 x) \int_{-\infty}^{\infty} dy \exp(-ivy)\, F_n(y,t) \ ,$$

$$F_n(y,t) = \int_{-\infty}^{\infty} dv \exp(ivy) \frac{1}{L} \int_0^L dx \exp(-ink_0 x)\, f(x,v,t) \ , \tag{2.18}$$

where $k_0 = 2\pi/L$, and L is the length of the system. The electric field, E , is expanded in a Fourier series in x ,

$$E(x,t) = \sum_{n=-\infty}^{\infty} E_n(t) \exp(ink_0 x) \ ,$$

$$E_n(t) = \frac{1}{L} \int_0^L E(x,t) \exp(-ink_0 x) dx \ . \tag{2.19}$$

By use of Eqs. (2.18) and (2.19), we obtain from Eq. (2.17)

$$\frac{\partial}{\partial t} F_n(y,t) + nk_0 \frac{\partial}{\partial y} F_n(y,t) - \frac{y}{k_0} C_n(y,t) = 0 \ ,$$

$$- ink_0 E_n(t) = F_n(0,t) \ , \tag{2.20}$$

where $C_n(y,t)$ is defined by

$$C_n(y,t) = \sum_{m=-\infty}^{\infty} \frac{1}{m} F_m(0,t)\, F_{n-m}(y,t) \ . \tag{2.21}$$

Equations (2.20) and (2.21) constitute the system of equations which is to be solved on the computer. Note that the integral over the distribution function in the Poisson equation [Eq. (2.17)] has disappeared. The electric field component E_0 is not determined uniquely by these

equations, but is determined by the boundary conditions. For a periodic system without external excitation, we may put $E_0 = 0$.

Equation (2.20) may be solved by integration along characteristics given by

$$t - t' = \frac{1}{nk_0} (y - y') \ . \tag{2.22}$$

These are straight lines in the (t,y) plane, as shown in Fig. 2.5.

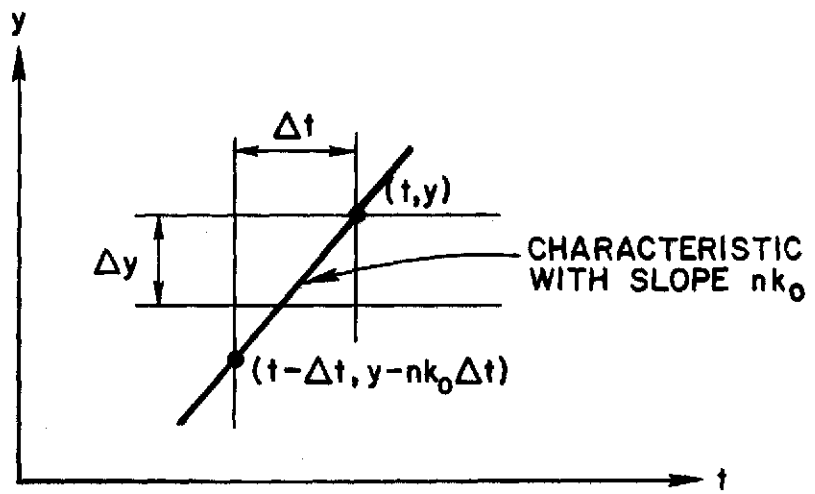

FIG. 2.5. Characteristics of Eq. (2.20) in the (t,y) plane.

The simplest numerical scheme is given by

$$F_n(y,t) = F_n(y - nk_0\Delta t,\ t - \Delta t)$$

$$+ \frac{\Delta t}{k_0} (y - nk_0\Delta t)\ C_n(y - nk_0\Delta t,\ t - \Delta t) \ . \tag{2.23}$$

For an improved approximation, we may use the iterative formula,[11]

$$F^{(s+1)}(y,t) = F(y - nk_0\Delta t,\ t - \Delta t)$$

$$+ \frac{\Delta t}{2k_0}\left[(y - n\Delta t)\, C_n(y - nk_0\Delta t,\ t - \Delta t) + yC_n^{(s)}(y,t)\right], \qquad (2.24)$$

where superscript s denotes the number of iterations carried out. Equation (2.24) is obtained by replacing the last term in Eq. (2.23) by the average of the values of C_n at the grid points (t,y) and $(t - \Delta t,\ y - nk_0\Delta t)$. Note that values of y in Eqs. (2.23) and (2.24) are chosen to fall at the grid points. Values of $y - nk_0\Delta t$ do not fall at the grid points unless Δy and Δt are chosen such that $\Delta y = k_0\Delta t$. Therefore, some interpolation scheme must generally be used.

Since it is not feasible to include an infinite number of terms in Eq. (2.18) in the calculations, nor to cover the whole y-space, the Fourier expansion is truncated at n_m, and a cut-off for $F_n(y,t)$ is introduced at $y = \pm y_m$. This is equivalent to a smoothing of the distribution function, $f(x,v,t)$, expressed by

$$\tilde{f}(x,v,t) = \int_{-\infty}^{\infty} w_v(v')dv' \int_{-\infty}^{\infty} w_x(x')f(x + x',\ v + v',\ t)dx' \qquad (2.25)$$

where $\tilde{f}(x,v,t)$ is the smoothed distribution function, and $w_x(x)$ and $w_v(v)$ are weighting functions given by

$$w_x(x) = 1 + 2\sum_{n=1}^{n_m} \cos nk_0x\ , \qquad w_v(v) = \frac{1}{\pi v}\sin y_m v\ . \qquad (2.26)$$

The choice of the cut-off values, n_m and y_m must be made so that the half-widths of the weighting functions are small compared with characteristic lengths and velocities in the plasma. The truncations do not cause numerical instability.[10]

Fourier-Hermite Expansion[3,10,12,13]: Instead of the Fourier transform in velocity used in the previous method, a Gram-Charlier series in velocity may be introduced,

$$f(x,v,t) = \sum_{n=-\infty}^{\infty} \sum_{m=0}^{\infty} \exp(ink_0 x) \exp\left(-\frac{v^2}{2}\right) h_m(v) Z_{mn}(t) , \qquad (2.27)$$

where the $h_m(v)$ are the orthonormal set of Hermite polynomials defined by

$$h_m(v) = \frac{(-1)^m \exp(v^2/2)}{[(2\pi)^{1/2} m!]^{1/2}} \frac{d^m}{dv^m} \exp\left(-\frac{v^2}{2}\right) . \qquad (2.28)$$

Again $k_0 = 2\pi/L$, and L is the length of the system. Electric field is expanded in a Fourier series according to Eq. (2.19). Substitution of Eqs. (2.19) and (2.27) in Eq. (2.17), and use of the recursion relations and orthogonality properties of Hermite polynomials and of Fourier series, yields

$$\frac{d}{dt} Z_{mn}(t) + ink_0 \left[m^{1/2} Z_{m-1,n}(k) + (m+1)^{1/2} Z_{m+1,n}(t) \right]$$

$$+ m^{1/2} \sum_{q=-\infty}^{\infty} E_{n-q}(t) Z_{m-1,q}(t) = 0 ,$$

$$(m = 1,2,3,\ldots;\ n = 0, \pm 1, \pm 2, \ldots) , \qquad (2.29)$$

$$\frac{d}{dt} Z_{0n}(t) + ink_0 Z_{1n}(t) = 0 , \qquad (n = 0, \pm 1, \pm 2, \ldots) , \quad (2.30)$$

$$E_n(t) = \frac{i(2\pi)^{1/4}}{nk_0} Z_{0n}(t) , \qquad (n \neq 0) , \quad (2.31)$$

where we have put $E_0(t) = 0$. The condition for reality of $f(x,v,t)$ requires that

$$Z_{mn}(t) = Z^*_{m,-n}(t) . \quad (2.32)$$

Combination of Eqs. (2.29)-(2.31) provides a set of nonlinear, ordinary differential equations for the $Z_{mn}(t)$. These may be solved step by step, typically by the Runge-Kutta method, or some improved technique.[14]

As in the Fourier-Fourier method, the infinite series expressed by Eqs. (2.19) and (2.27) have to be truncated. However, unlike the Fourier-Fourier method, the truncation of the infinite series [Eqs. (2.27)] in velocity-space causes serious difficulties. Truncation of the Fourier series can be justified provided that the perturbation amplitude is small. However, suppose that the Gram-Charlier series is truncated at $m = M$. From inspection of Eq. (2.29), it is clear that the expression for dZ_{mn}/dt depends on $Z_{m+1,n}(t)$. The truncation consequently introduces serious inaccuracy, and therefore instability, when $Z_{M+1,n}(t)$ becomes large. Since $Z_{Mn}(t)$ is large by the time $t = M^{1/2}/(nk_0)$, the results of the computation are valid only for shorter times. This imposes a severe limitation on the usefulness of this method. A few attempts have been made to remove it, and the reader is referred to the relevant literature.[3,10,13]

Power Series Expansion[15]: Consider an expansion of $F_n(y,t)$ in Eq. (2.18) in powers of y, given by

$$F_n(y,t) = \sum_{m=0}^{\infty} a_{mn} g_m y^m \exp\left(-\frac{y^2}{2}\right) , \tag{2.33}$$

where the g_m are arbitrary. The exponential factor improves the convergence of the series if it is truncated in the y-direction. Substituting Eq. (2.33) into Eq. (2.20), and collecting equal powers of y, gives

$$\frac{d}{dt} a_{mn} - nk_0\left[\frac{g_{m-1}}{g_m} a_{m-1,n} - (m+1)\frac{g_{m+1}}{g_m} a_{m+1,n}\right]$$

$$- \frac{g_{m-1}}{k_0 g_m} \sum_{q=-\infty}^{\infty} a_{0q} a_{m-1,n-q} = 0 , \tag{2.34}$$

$$(n = 0, \pm 1, \pm 2, \ldots; \; m = 0, 1, 2, \ldots) .$$

This equation can be solved in a similar way to Eq. (2.29) obtained in the Fourier-Hermite method. It should be noted that the coefficients a_{mn} may be shown to be equal to the Z_{mn} in the Fourier-Hermite method except for a complex factor.[15]

In the numerical integration, Joyce et al. have encountered the difficulty associated with the truncation of the infinite series in velocity space that was found in the Fourier-Hermite method.[15] However, they found that numerical solution of the linearized version of Eq. (2.34) gave a very regular pattern for the amplitudes a_{mn} for large m, as shown in Fig. 2.6. The coefficients seem to be sampled points of a

continuous function in m. This would lead to a guess that the $(m_{max} + 1)$ coefficient may be extrapolated by polynomials, and that it may be possible to close the system expressed by Eq. (2.34). This method turned out to work well for the linear Vlasov equation, but Joyce et al. found that for nonlinear cases its success depends on the problems treated. Thus, although there is improvement over the Fourier-Hermite method, in the sense that it stabilizes the integration scheme, the method is still not satisfactory for simulations carried to long times.

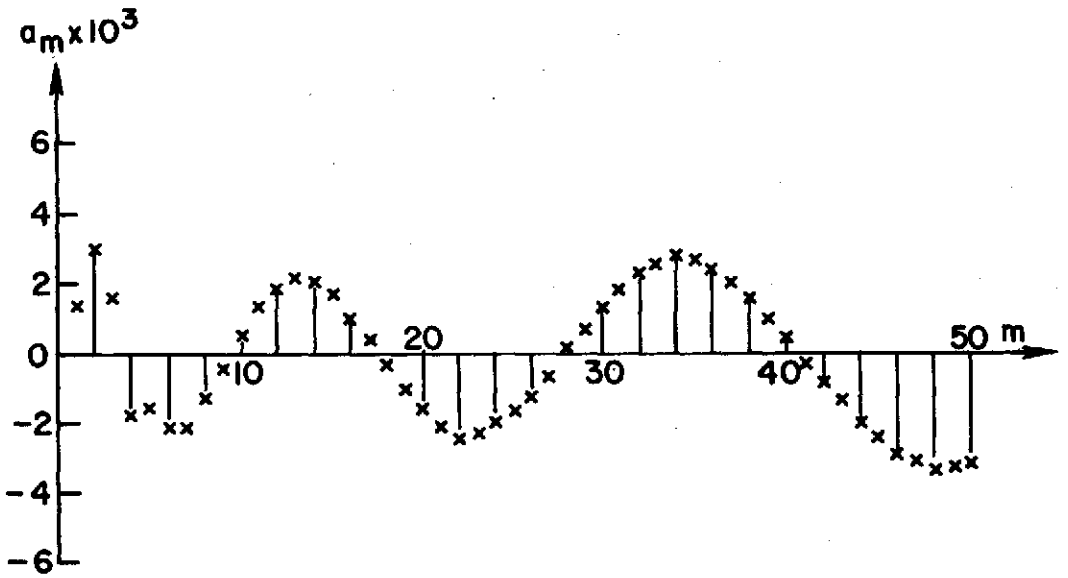

FIG. 2.6. An example of amplitude a_{mn} vs. m. (Adapted from Fig. 1 of Ref. 15.).

2.3 Particle Simulation Model

A number of authors have developed schemes which reduce the high level of fluctuations characteristic of the electrostatic sheet model, without affecting the collective behavior of the plasma.[16-26] The reduction of fluctuations in these schemes is achieved by smoothing the interaction forces between the charge sheets. The smoothing reduces the short wavelength fluctuations arising from discontinuities in the electric field generated by the sheets, but leaves collective phenomena associated with long wavelengths unaffected. Since the smoothing may modify the physics of the plasma, and perhaps introduce spurious effects, it is important to examine very closely the detailed behavior of the model. In this section, we shall describe various electrostatic plasma models incorporating smoothing procedures, and discuss some of the physical consequences of the smoothing relevant to the hybrid approach to be treated in Section 3. All of these schemes can be used for multi-dimensional simulations, with or without an externally applied magnetic field, but the discussion here will concentrate on the one-dimensional case without magnetic field.

2.3.1 Zero-Size-Particle and Nearest-Grid-Point Method

In this method, instead of treating the space variable, x, as a continuous variable when computing the electric field, the system is divided into an arbitrary number of cells, and the electric field is computed only at grid points corresponding to the centers of the cells. The charge distribution from which the electric field is calculated, through the Poisson equation, is obtained by accumulating the charge of all the sheets in each cell at the center, regardless of their

positions within the cell. In advancing in time, all of the particles in one cell are accelerated by the electric field defined at the grid point, regardless of their positions. Note, however, that the particle position is not discretized, but is a continuous variable. This scheme was used by Burger et al. in a study of randomization mechanisms in a collisionless plasma.[16] Hockney applied it in a two-dimensional simulation of anomalous plasma diffusion across a static magnetic field, using a charge rod model.[17,18]

In one dimension, the electric field calculation is quite simple. The charge distribution on the grid points is obtained by counting the number of electron and ion sheets separately in individual cells, multiplying them by the surface charge density, and subtracting the results. The electric field at a given grid point is then taken at the middle of the jump in electric field occurring at that grid point. When ions can be assumed to be immobile, equal numbers of ion sheets are assigned to each cell, and only the number of electron sheets needs to be counted.

Advancing particles in time through the Newton equation may be done by the leap-frog scheme. In one dimension this may be written, for an electron sheet, as

$$v_{n+1/2} = v_{n-1/2} - \frac{e}{m_e} E_n \Delta t , \qquad x_{n+1} = x_n + v_{n+1/2} \Delta t , \qquad (2.35)$$

where $v_{n+1/2}$ and $v_{n-1/2}$ denote the velocities of the sheet at a half time-step ahead of, and behind, the n-th time-step, respectively, x_n and E_n are the sheet position and electric field at the n-th

time-step, m_e and e are electron mass and charge (magnitude), and Δt is the time-step. This scheme is widely used because of its high order accuracy $[0\{(\Delta t)^3\}]$.

The ZSP-NGP scheme not only reduces fluctuations, but also makes the computation much faster than for the simple sheet or rod model. Furthermore, the gain in computational speed is made by using integer, rather than floating-point, arithmetic on the computer. In most computers the integer addition and subtraction are faster than the floating-point addition and subtraction. Since the main part of the algorithm can be written in terms of additions and subtractions, computing time can be saved by normalizing and expressing the particle positions and velocities, and the charge and electric field, in terms of integers. The reader is referred to the relevant papers for more details.[27,28]

The reduction of fluctuations can be understood as follows: the interaction force between a charge sheet located at a grid point, and another sheet separated by distance, x, will be as shown in Fig. 2.7(a). The method eliminates forces acting in close encounters, whereas in the simple sheet model there is no zero-force region. This helps to reduce collisional effects, and fluctuations at short wavelengths, but does not affect the collective behavior due to long range forces.

The force between two charge rods is illustrated in Fig. 2.7(b). It is a function varying in steps. At large separations, it is a good approximation to the force between two line charges. At close separations, however, the force vanishes, as in the one-dimensional case, whereas the force between two line charges would tend to infinity.

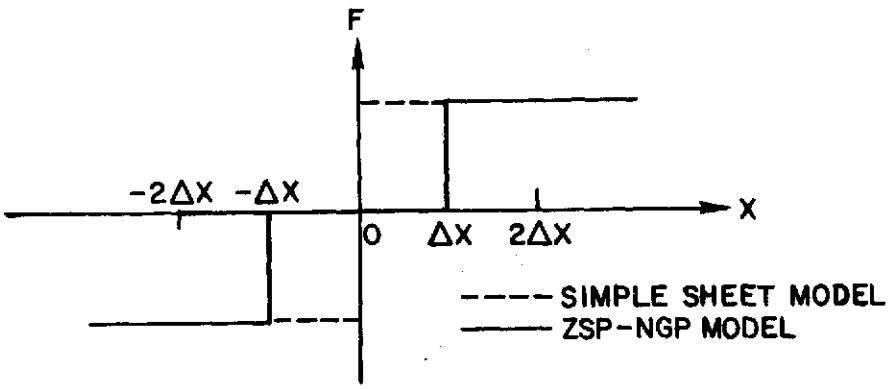

FIG. 2.7(a). Interaction force in ZSP-NGP model, between a charge sheet at a grid point, and another sheet at distance x apart. (Adapted from Fig. 5 of Ref. 29.).

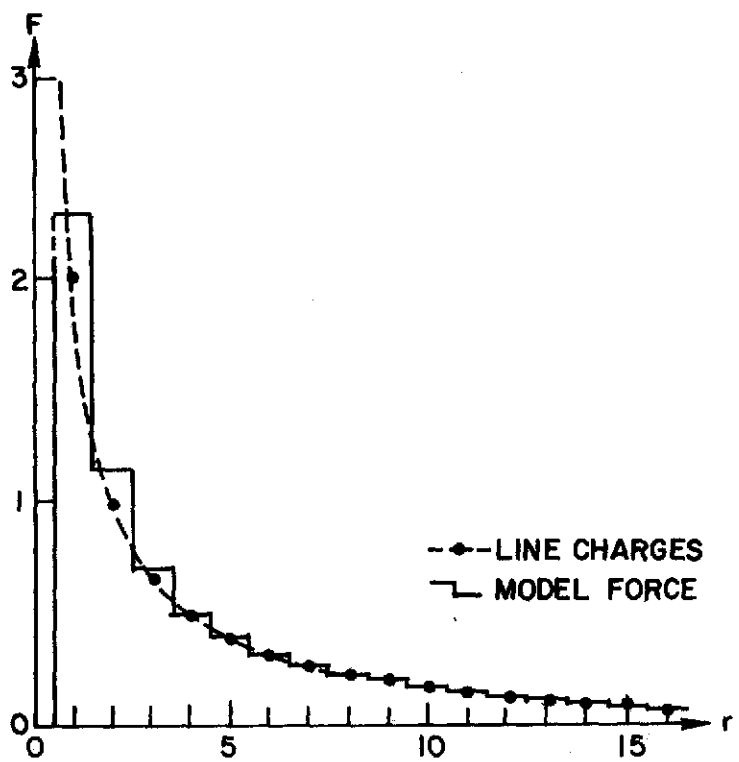

FIG. 2.7(b). Interaction force in ZSP-NGP model, between two charge rods distance r apart. r is in units of cell size h . (Adapted from Fig. 1 of Ref. 17.).

Although the ZSP-NGP method has been used successfully,[16-18] the stepped force law shown in Fig. 2.7 may not be accurate enough, and the zero-force region may smooth out small amplitude oscillations, even for long wavelengths. The discontinuity in the electric field still produces undesirable enhanced fluctuations. One way to relieve these difficulties is to increase the number of particles and to use a finer grid. In practice, however, it is not always feasible to increase the number of particles and grid points to a satisfactory level. The finite-size particle models which we shall discuss next have been developed to overcome these difficulties, particularly in the simulation of high density plasmas. We shall describe the Cloud-in-Cell method, Particle-in-Cell method, Gaussian Cloud method, Multipole Expansion method, and Lewis' method.

2.3.2 Cloud-in-Cell and Particle-in-Cell Methods

It is natural to introduce the idea of charged particles of finite dimensions, for the purpose of improving upon the ZPS-NGP method. In the Cloud-in-Cell method, the discontinuities are mitigated by considering clouds of uniformly distributed charge which are assumed to be tenuous, and to be able to pass through one another.[19] The center of the charge cloud is taken to be the particle coordinate, and a spatial grid is used for computing field quantities. Key features of the method are the prescription for determining the amount of charge to be assigned to the grid points (charge-sharing), and the force on a cloud from field quantities on the grid points (force-sharing). The charge is distributed to neighboring cell centers (grid points) in proportion to the areas the cloud occupies in the cells. The charge

density on the grid points thus accumulated is used to compute the electric field. The force on a cloud is calculated by averaging the contributions from the neighboring grid points with weightings proportional to the areas in the corresponding cells occupied by the cloud. For example, in the one-dimensional case shown in Fig. 2.8(a), the

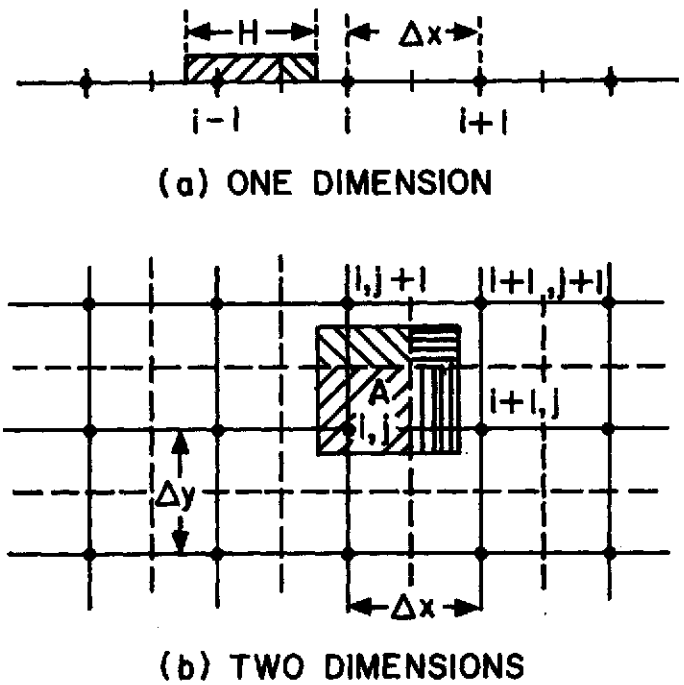

FIG. 2.8. Finite-size particle located in a grid. Shading shows assignment of charge density to grid points in CIC model.
(a) Δx is cell size. H is particle size.
(b) Δx and Δy are cell sizes. A is area of a particle.

charge assigned to each grid point is given by

$$\rho_i = \rho_c\left(\frac{a_i}{H}\right), \qquad \rho_{i+1} = \rho_c\left(\frac{a_{i+1}}{H}\right), \qquad a_i + a_{i+1} = H \ , \qquad (2.36)$$

where ρ_c is the charge density of the cloud, H denotes the size of the cloud, and a_i represents the portion of the cloud occupying the i-th cell. The extension to the two-dimensional case is shown in Fig. 2.8(b). The charge assigned to each grid point is given by

$$\rho_{i,j} = \rho_c\left(\frac{a_{i,j}}{A}\right), \qquad \rho_{i+1,j} = \rho_c\left(\frac{a_{i+1,j}}{A}\right),$$

$$\rho_{i+1,j+1} = \rho_c\left(\frac{a_{i+1,j+1}}{A}\right), \qquad \rho_{i,j+1} = \rho_c\left(\frac{a_{i,j+1}}{A}\right), \tag{2.37}$$

$$a_{i,j} + a_{i+1,j} + a_{i+1,j+1} + a_{i,j+1} = A,$$

where A denotes the area of the cloud, and $a_{i,j}$ represents the portion of the cloud occupying (i,j) cell.

The cloud size may be either larger or smaller than, or equal to, the cell size. It is chosen so that the particle dynamics can be adequately represented for the problem of interest. This will be clear from Fig. 2.9, which shows the density assigned to grid point i for clouds of various sizes moving in the x-direction. As the cloud size increases beyond the cell size, the resolution decreases, because the cloud density is held constant over a distance larger than the shortest resolvable wavelength, i.e. the cell width.

The force on the cloud is given by,

$$F = \rho_c \sum_i \frac{a_i}{H} E_i \qquad \text{(one dimension)}$$

$$\underset{\sim}{F} = \rho_c \sum_{i,j} \frac{a_{i,j}}{A} \underset{\sim}{E}_{ij} \qquad \text{(two dimensions)} \tag{2.38}$$

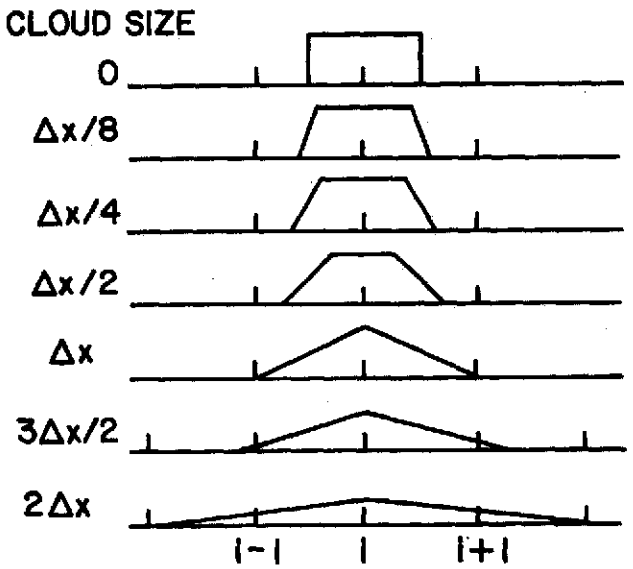

FIG. 2.9. Sketch of charge density assigned to grid point i as a finite-size particle moves in x-direction. The size varies from 0 to $2\Delta x$. The horizontal axis represents the position of the center of the cloud. (Adapted from Fig. 3 of Ref. 19.).

where E_i (or $\underline{E}_{ij}$) is the electric field at the grid points (see Fig. 2.8). This force-sharing scheme produces no self-force if it is used together with the charge-sharing scheme just described. If this charge-sharing scheme were not followed, the force averaging could lead to incorrect acceleration of clouds.[19,29]

The interaction force between a cloud fixed at a grid point, and another cloud is plotted as a function of separation in Fig. 2.10. It will be noted that the interaction is much smoother than in the ZSP-NGP method, and that the zero-force region is eliminated. The CIC scheme consequently produces less collisional effects than the simple sheet

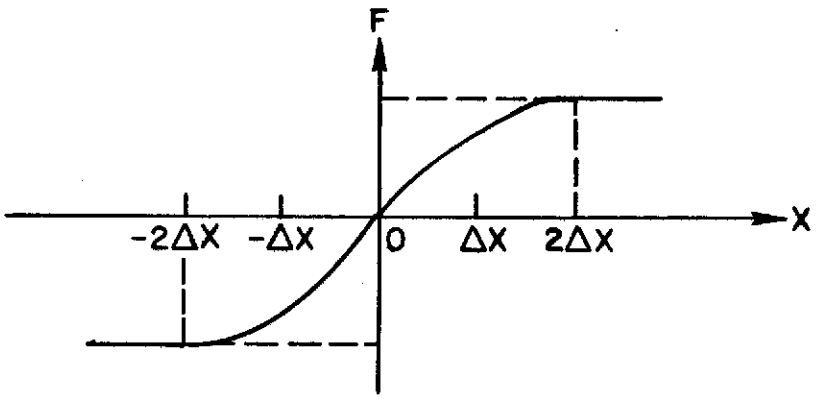

FIG. 2.10(a). Interaction force in CIC model, between a cloud at a grid point and another cloud at distance x apart. [H = Δx]. (Adapted from Fig. 6 of Ref. 29.).

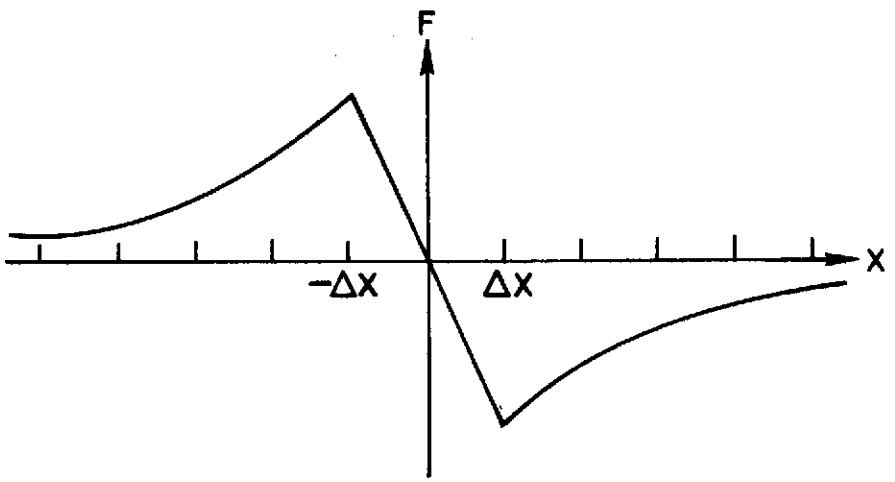

FIG. 2.10(b). Interaction force in CIC model, between a positive charge cloud at a grid point and a negative charge cloud, at distance x apart but with the same y coordinate. [H_x = Δx]. (Adapted from Fig. 4 of Ref. 19.).

model, and is better able to simulate small amplitude oscillations. It has been observed by Birdsall and Fuss that the CIC method, combined with the leap-frog algorithm, greatly improves the energy conservation over the ZSP-NGP method for the same number of simulation particles.[19]

In the Particle-in-Cell method, proposed by Morse and Nielson, the charge is assigned to each cell by distributing the charge of a particle between the nearest two cells according to a linear interpolation.[20,21] The electric field is then calculated from the resulting charge distribution on the grid points, in the same way as in the ZSP-NGP and CIC methods. The force on a particle is obtained by calculating the electric field at the particle position by linear interpolation between the nearest two cell centers. It is easily seen that this scheme is a special case of the CIC scheme, with the particle size equal to the cell size.

2.3.3 Gaussian Cloud Method

Instead of a uniform charge distribution, in this method a cloud is supposed to have a Gaussian charge distribution,

$$\rho_i(x) = \frac{\rho_c}{(2\pi a)^{1/2}} \exp\left[-\frac{(x - x_i)^2}{2a^2}\right], \qquad (2.39)$$

where x_i is the position of the center of the cloud i, and a represents the one-dimensional size of the cloud.

To compute the electric field from a given distribution of charge, it is convenient to work in Fourier-transformed space rather than in coordinate-space, i.e. in k-space rather than x-space. The Poisson

equation then simplifies to an algebraic form, and is handled more easily. The Fast-Fourier-Transform technique can be used to speed up the computation.[30]

A model proposed by Dawson et al. makes use of the foregoing ideas in the following way.[22] The electric field generated by a Gaussian cloud is obtained by the Fourier transform,

$$E(x) = \int E(k)\, \exp(ikx)dk \ , \tag{2.40}$$

where $E(k)$ is given by

$$ikE(k) = \frac{4\pi\rho_c}{(2\pi)^{1/2}} \exp\left[- \frac{k^2a^2}{2} + ikx_i \right] . \tag{2.41}$$

The force on particle i due to particle j is then given by

$$\begin{aligned} F_{ij} &= \int E_j(x)\rho_i(x)dx \\ &= 2\rho_c^2 i \int \frac{1}{k} \exp[ik(x_i - x_j) - k^2a^2]dk \ . \end{aligned} \tag{2.42}$$

The integral over k-space is replaced by the finite sum

$$F_{ij} = 2\rho_c^2 \sum_{k_{min}}^{k_{max}} \frac{1}{k} \exp(-k^2a^2) \sin k(x_i - x_j) \ , \tag{2.43}$$

where $k = 2\pi n/L$, n is an integer, and L is the length of the system. To advance particle i in time, the total force on it is calculated by summing the contributions from all other particles, and is assumed to be constant during a time-step. The leap-frog scheme may be used in this model.[23] As will be shown in Section 2.3.6, the

fluctuations with short wavelengths can be reduced substantially below those in the simple sheet model as the value of a increases.

2.3.4 Multipole Expansion Method

The multipole expansion scheme was developed by Kruer and Dawson.[24] It was used by Denavit and Kruer, and compared with numerical solutions of the Vlasov equation for two-stream instability and sideband instability.[11] Close agreement was obtained between the results of the two methods. Consider a charge cloud with an arbitrary charge distribution and a spatial grid. The location of the center of the particle is defined by

$$x_i = x_{Gi} + \delta x_i \ , \tag{2.44}$$

where x_{Gi} is the nearest grid point location, and δx_i is the particle coordinate relative to x_{Gi}. The Fourier transform of the cloud charge density, $\rho_i(x)$, of particle i is

$$\begin{aligned} \rho_i(k) &= \int \rho_i(x) \exp(-ikx)dx \\ &= S(k) \exp(-ikx_{Gi}) \exp(-ik\delta x_i) \ , \end{aligned} \tag{2.45}$$

where $S(k)$ is the form factor, which is the Fourier transform of the shape factor given by

$$S(x - x_i) = \rho_i(x) \ . \tag{2.46}$$

Assuming $k\delta x_i \ll 1$, we may expand $\rho_i(x)$ as follows

$$\rho_i(k) = S(k) \exp(-ikx_{Gi})(1 - ik\delta x_i + \ldots) \ . \tag{2.47}$$

This is equivalent to replacing the particle centered somewhere in the cell by a particle centered at the nearest grid point, plus a dipole there and higher-order multipole terms. Summing over a collection of particles, and inverse Fourier-transforming the Poisson equation, yields the electric field at the grid point.

To compute the force on a particle, given by

$$F_i = \int E(x)\rho_i(x)dx \ , \tag{2.48}$$

we expand $\rho_i(x)$ as follows

$$\begin{aligned} \rho_i(x) &= S(x - x_i) \\ &= S(x - x_{Gi} - \delta x_i) \\ &= S(x - x_{Gi}) - \delta x_i S'(x - x_{Gi}) + \ldots \ , \end{aligned} \tag{2.49}$$

where S' denotes a derivative with respect to x. Integrating by parts yields

$$F_i = \int E(x)S(x - x_{Gi})dx + \delta x_i \int E'(x)S(x - x_{Gi})dx + \ldots\ldots \ . \tag{2.50}$$

Physically, this means that the force on a particle may be represented by its monopole times the electric field, plus the dipole moment times the derivative of the field, plus higher-order contributions.

The scheme just outlined is valid only if $k_{max}\delta x_i \ll 1$. In order for this to be satisfied, the particle size, H, has to be larger than the cell size, Δx, because $\delta x_i \leq \Delta x/2$ and $k_{max} H \sim 1$. In practice, the expansion is truncated at the dipole term, and a particle size of several cell-lengths is necessary, i.e., if the particle size is comparable to the cell size the simulated behavior of short wavelength

perturbation is likely to be inaccurate. When the short wavelength components are not important, it may be adequate to use this scheme even for $H \sim \Delta x$.

2.3.5 Lewis' Method

In the simulation of plasma phenomena, it is important to check whether the model conserves energy. If there is no external excitation, the total energy of the system should remain substantially constant during the simulation run. Otherwise, it is to be suspected that nonphysical effects are being introduced. There is no guarantee that the models described so far are energy-conserving. Lewis has presented a general method for deriving numerical approximation schemes which guarantee energy conservation.[25,26] It is based on a Lagrangian formulation via Hamilton's variational principle. The CIC method is closely related to a special case of the algorithms based on this formulation. The Lewis method serves to establish both the theoretical basis for the use of various models in plasma simulation, and to provide an alternative viewpoint on the problems involved. We shall outline the method and show how the energy-conserving version of the CIC scheme is derived by Lewis.

For simplicity, we consider a one-dimensional, electrostatic plasma with no externally applied fields and neutralizing immobile ions. The Lagrangian for this system is

$$\mathcal{L} = \int dx'dv'f(x',v',0)\left\{\frac{m_e\dot{X}^2}{2} + e\phi(X,t)\right\} + \frac{1}{8\pi}\int dx E^2(x,t) \ , \qquad (2.51)$$

where $X[= X(x',v',t)]$ describes particle trajectories as functions of

the time, t, initial position, x', and velocity, v', the dot denotes differentiation with respect to t, $f(x,v,0)$ is the initial distribution function, ϕ is the electrostatic potential, and $E = -\partial\phi/\partial x$. We approximate ϕ and X by finite series

$$\phi(x,t) = \sum_{n=1}^{N_1} \alpha_n(t)\Phi_n(x) , \qquad X(x',v',t) = \sum_{\ell=1}^{N_2} \gamma_\ell(t)X_\ell(x',v') , \tag{2.52}$$

where $\Phi_n(x)$ and $X_\ell(x',v')$ are linearly independent basis functions, and $\Phi_n(x)$ must satisfy the boundary conditions. Substitution of Eq. (2.52) into Eq. (2.51) provides a new Lagrangian which is a function of the generalized coordinates, α_n, γ_ℓ, and the generalized velocities, $\dot{\gamma}_\ell$. Applying Hamilton's principle,

$$\delta \int_{t_1}^{t_2} \mathfrak{L}\, dt = 0 , \tag{2.53}$$

for arbitrary variation of α_n and γ_ℓ, we obtain the Euler-Lagrange equations,

$$\frac{d}{dt}\left(\frac{\partial \mathfrak{L}}{\partial \dot{\gamma}_\ell}\right) - \frac{\partial \mathfrak{L}}{\partial \gamma_\ell} = 0 , \qquad \frac{\partial \mathfrak{L}}{\partial \alpha_n} = 0 . \tag{2.54}$$

These are the equations which describe energy-conserving numerical approximation schemes. It remains to specify functions Φ_n and X_ℓ.

Let the initial distribution function be a sum of the Dirac delta-functions,

$$f(x,v,0) = \sum_i \delta(x - x_i)\, \delta(v - v_i) \ , \tag{2.55}$$

where x_i and v_i are the initial position and velocity of the i-th particle. Choosing a set of X_ℓ-functions as

$$X_\ell(x',v') = \begin{cases} 1 & (x' = x_\ell,\ v' = v_\ell) \ , \\ 0 & (\text{otherwise}) \ , \end{cases} \tag{2.56}$$

implies that the initial conditions on the $\gamma_\ell(t)$ are

$$\gamma_\ell(0) = x_\ell \ , \qquad \dot{\gamma}_\ell(0) = v_\ell \ . \tag{2.57}$$

Clearly, $\gamma_\ell(t)$ is the position of the ℓ-th particle at time t. To obtain an energy-conserving version of the CIC scheme, it is convenient to take $\Phi_n(x)$ to be

$$\Phi_n(x) = \begin{cases} \frac{1}{h}[x - (n-1)h] & [(n-1)h \le x \le nh], \\ \frac{1}{h}[(n+1)h - x] & [nh \le x \le (n+1)h], \\ 0 & [\text{otherwise}] \ , \end{cases} \tag{2.58}$$

where $h = L/(N_1+1)$, and L is the system length. With this set of functions, $\alpha_n(t)$ is the value of potential at $x = nh$.

Substituting Eqs. (2.56) and (2.58) into the Euler-Lagrange equations [Eq. (2.54)] gives

$$m_e \ddot{\gamma}_\ell = e \sum_i \alpha_i(t) \Phi_i'[\gamma_\ell(t)] \ , \tag{2.59}$$

$$-\frac{\alpha_{n+1}(t) - 2\alpha_n(t) + \alpha_{n-1}(t)}{h^2} = \frac{\rho_0}{\epsilon_0} - \frac{e}{\epsilon_0 h}\sum_{\ell} \Phi_n[\gamma_\ell(t)] \ , \quad (2.60)$$

where $\Phi_i'(x) \equiv (d/dx)\Phi_i(x)$, and ρ_0 is the background charge density. Equation (2.59) is the equation of motion for the ℓ-th particle and Eq. (2.60) is the central difference approximation for the Poisson equation. It is seen that Eq. (2.60) is identical to the approximation for the Poisson equation in the CIC method. Equation (2.59) differs from the equation of motion in the CIC method only in that a piecewise linear function is used in place of $\Phi_i'[\gamma_\ell(t)]$. The CIC method consequently does not conserve energy. Equations (2.59) and (2.60) are the energy-conserving version of the CIC scheme. It should be noted that the energy conserving feature of this method is realized only in the limit of a vanishingly short time-step. In practice, the time-step is small but finite, so the energy conservation is not exact.

2.3.6 Finite-Size Particle and Spatial Grid Effects

In this section, we shall consider the effects of introducing finite-size particles, and a spatial grid into simulation models. We shall follow the analyses given by Langdon[31] and Birdsall[29] and consider, first, how longitudinal plasma oscillations are affected, and second, how the fluctuations are reduced.

In general, finite particle size enters the analysis via the form factor, S(k), i.e. the Fourier transform of the shape factor of the charged particle distribution, S(x) ,

$$S(k) = \int dx S(x) \exp(-ikx), \quad (2.61)$$

Using the form factor $S(k)$, the charge density, current density, and force in the finite-size particle model can be written as,

$$\rho_c(k,t) = S(k)\rho_p(k,t) \ , \qquad J_c(k,t) = S(k)J_p(k,t) \ ,$$

$$F_c(k,t) = S(-k)F_p(k,t) \ , \tag{2.62}$$

where subscript p in ρ_p , J_p , and F_p is affixed to emphasize that they are for a system of point particles. These relations suggest that the theory of finite-size particles may be obtained by multiplying the charge in the point particle theory by $S(k)$. This is indeed so for the longitudinal plasma permittivity: for a one-dimensional plasma with finite-size cloud, we have

$$\epsilon_p(k,\omega) = 1 + S^2(k)\frac{\omega_p^2}{k}\int \frac{\partial f_0/\partial v}{\omega - kv}\, dv \ , \tag{2.63}$$

where Landau's prescription applies regarding analytic continuation.

For a Maxwellian velocity distribution, and CIC-type finite-size particles, Eq. (2.63) becomes

$$\epsilon_p(k,\omega) = 1 - \frac{S^2(k)}{2k^2\lambda_D^2} Z'\left(\frac{\omega}{2^{1/2}kv_t}\right) \ ,$$

$$S(k) = \frac{\sin\,(kH/2)}{(kH/2)} \ , \tag{2.64}$$

where H is the size of the cloud, and Z' denotes the first derivative of the plasma dispersion function.[32] For a Gaussian cloud, such as is used in the Gaussian Cloud method, the form factor becomes

$$S(k) = \exp(-k^2a^2/2) \ . \tag{2.65}$$

Note that in the limit of vanishing size, S(k) tends to unity and the point particle theory, i.e. the simple sheet model, is retrieved.

We have obtained solutions of the dispersion relation $[\epsilon_p(k,\omega) = 0]$ for point particles, and for finite-size particles. They are plotted in Fig. 2.11. It is clear that the long wavelength oscillations are little affected, while the short wavelength oscillations are strongly modified.

When spatial grid effects are taken into account, the permittivity is given by[31]

$$\epsilon_p(k,\omega) = 1 - \frac{1}{2K^2\lambda_D^2} \sum_{\ell} |S_e(k_\ell)|^2 \frac{\kappa}{k_\ell} Z'\left(\frac{\omega}{2^{1/2}|k_\ell| v_t}\right),$$

$$S_e(k) = S(k) \frac{\sin(k\Delta x/2)}{(k\Delta x/2)}, \qquad K = k \frac{\sin(k\Delta x/2)}{(k\Delta x/2)},$$

$$\kappa = k \frac{\sin k\Delta x}{k\Delta x}, \qquad k_\ell = k - \ell \frac{2\pi}{\Delta x}, \tag{2.66}$$

where ℓ is integer.

This dispersion relation has been studied in detail by Langdon,[31] who has shown that small values of $\lambda_D/\Delta x$ lead to instability. This is due to the coupling between waves with different wavelengths through the spatial grid. He has also shown that when $\lambda_D/\Delta x \geq 1$, the instability is negligible, and the $\ell = 0$ term in the summation in Eq. (2.66) is dominant. The result of our computation for dispersion characteristics with both finite-size effects and spatial grid effects taken in account is shown in Fig. 2.11. Only the $\ell = 0$ term has been retained in Eq. (2.66). It will be seen that the spatial grid exerts an additional

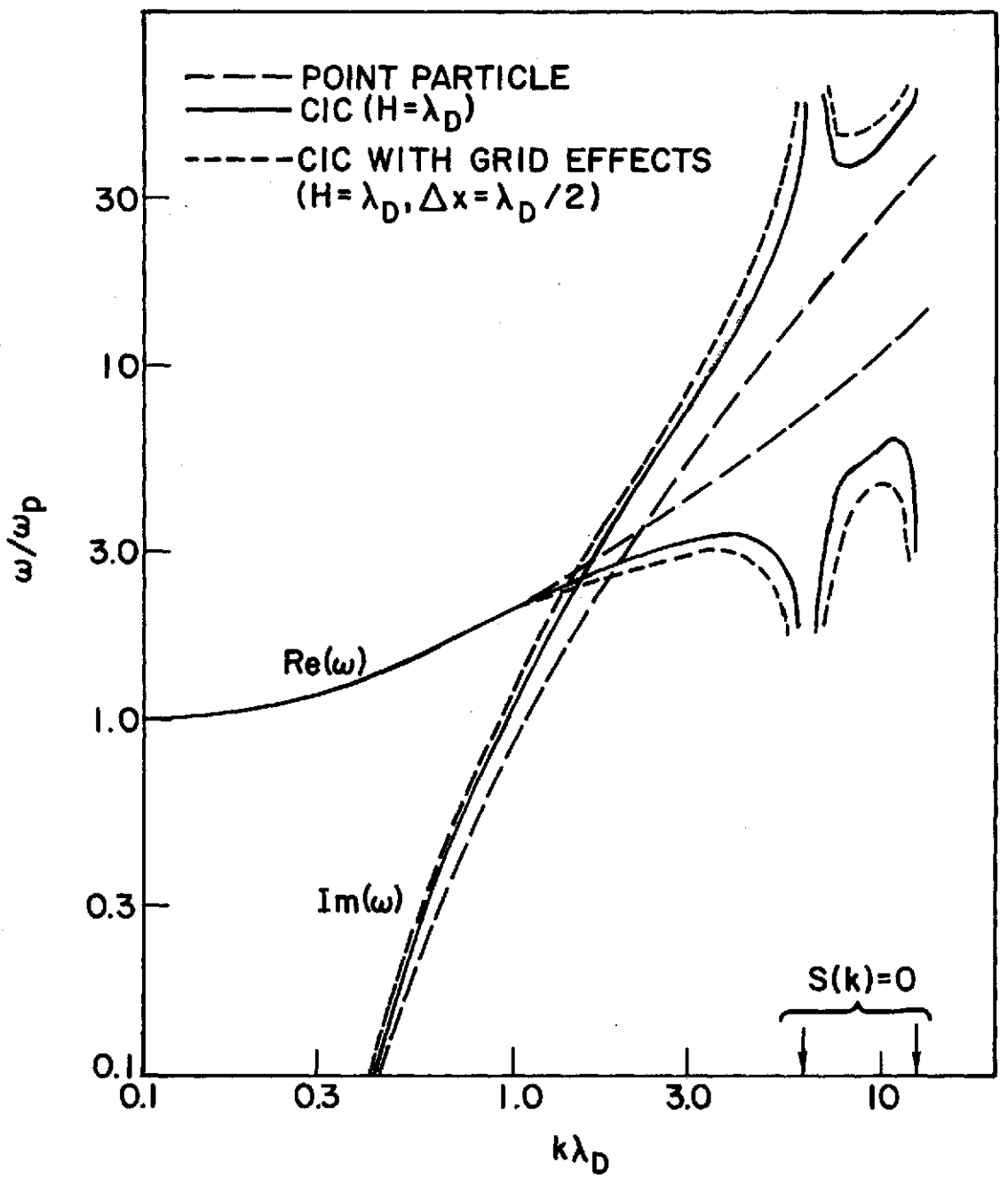

FIG. 2.11. Solutions of dispersion relation, [Eq. (2.66)].

smoothing effect on the dispersion characteristics, modifying the behavior of short wavelength oscillations in a similar way to finite-size effects, leaving the collective behavior at long wavelengths almost unchanged.

Finally, we turn our attention to the thermal fluctuation spectrum. The fluctuation spectrum of the electric field in k-space for a point particle plasma is

$$\frac{\langle E_k^2 \rangle}{8\pi} = \frac{k_B T}{2} \left(\frac{1}{1+k^2\lambda_D^2} \right) , \tag{2.67}$$

where k_B is the Boltzmann constant, and T is the temperature of the plasma. Neglecting the coupling between perturbations due to the grid, the fluctuation spectrum for a cloud plasma in a gridded system is given by[33]

$$\frac{\langle E_k^2 \rangle}{8\pi} = \frac{k_B T}{2} \left(\frac{\kappa^2}{K^2} \right) \left(\frac{1}{\kappa/k + K^2\lambda_D^2/S_e^2(k)} \right) , \tag{2.68}$$

where κ , K , and S_e are given in Eq. (2.66). In Fig. 2.12, the spectrum computed from Eq. (2.68) is plotted for the CIC finite-size particle model, and for the Gaussian Cloud model in a gridless system ($\Delta x \to 0$). The thermal fluctuation spectrum for the point particle plasma [Eq. (2.67)] is also shown for comparison. Note that the comparison in Fig. 2.12 is for the same number of particles. The reduction of fluctuations in the short wavelength part of the spectrum is apparent. An interesting feature of the plots is that the CIC spectrum has zero-energy holes, corresponding to modes satisfying $S(k) = 0$, while the Gaussian Cloud model does not.

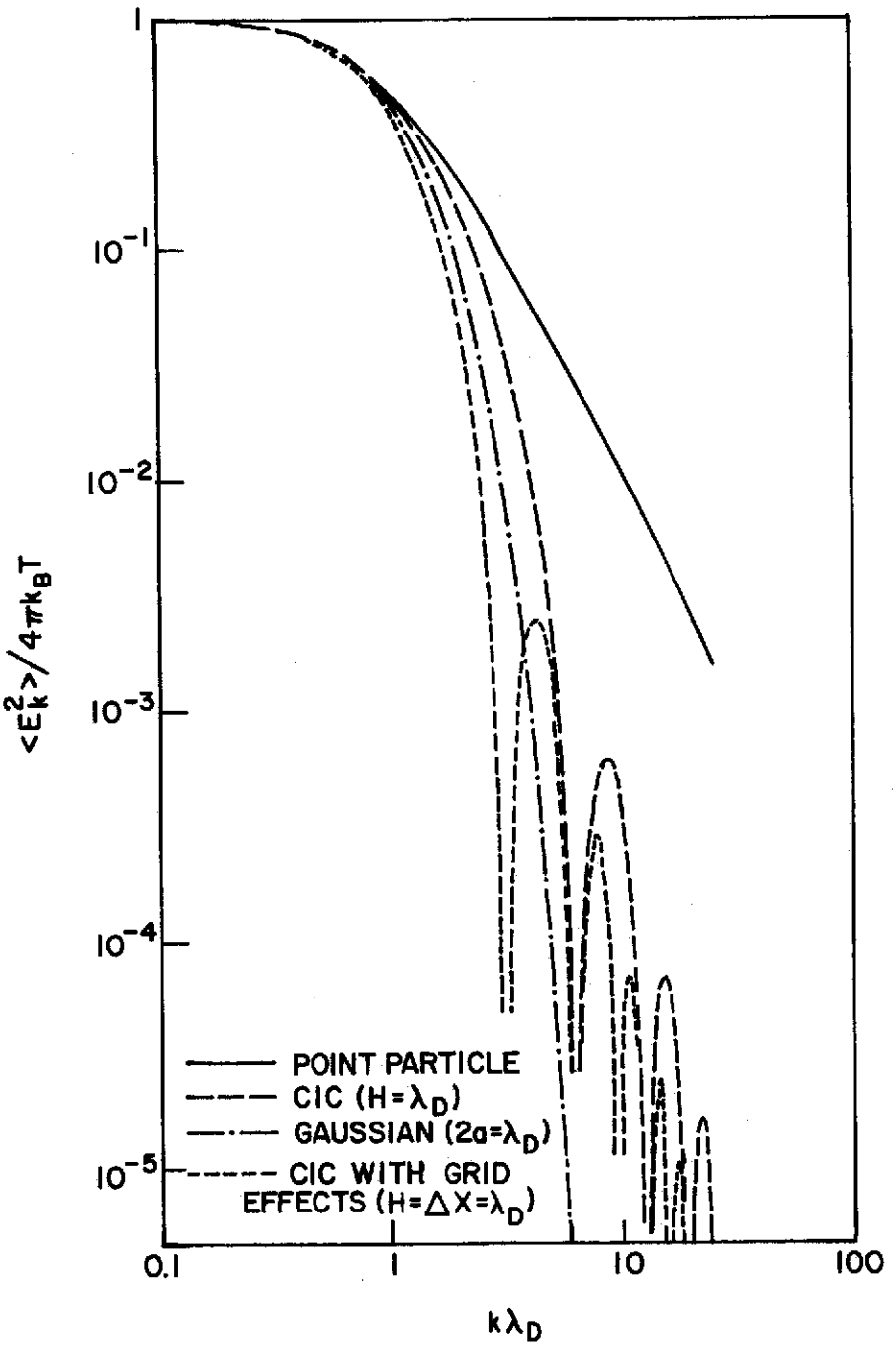

FIG. 2.12. Fluctuation spectrum of electric field. [Eq. (2.68)].

The modification due to spatial grid effects in the CIC model is also shown in Fig. 2.12. It will be seen that introducing a spatial grid reduces the short wavelength fluctuations further, and creates additional holes in the spectrum.

The analytical results of Eqs. (2.66) and (2.68) were verified by Okuda in computer studies of the CIC model.[34] Okuda also performed a series of simulations to study the numerical instability due to a spatial grid,[35] and confirmed that the simulation is stable when the Debye length is comparable to, or larger than, the grid size, as predicted by Langdon.[31]

It is evident from the foregoing considerations that finite-size particle models are capable of simulating the collective behavior of plasma, with reduced fluctuation level, by choosing appropriate particle and grid sizes. However, the reduction in the fluctuations in these methods is not more than about 10 dB below the simple sheet model. It is consequently still very noisy compared with the practical plasmas being simulated. In Section 3, we shall describe a method which provides a fluctuation level several orders of magnitude lower than the finite-size particle models.

3. LOW-NOISE HYBRID APPROACH

3.1 Comparison between the Vlasov and Particle Simulation Approaches

Before describing the hybrid approach used in our work, it is convenient to compare here the two basic approaches to computer solution of plasma problems discussed in Section 2. We shall do so by considering how well the plasma dynamics can be represented, and how easy the computer solution is to accomplish.

3.1.1 Plasma Dynamics

The Vlasov approach brings into question the validity of the Vlasov equation itself: the Vlasov equation is a description of a plasma which is correct only to lowest order in the plasma parameter, $(n\lambda_D^3)^{-1}$, where n is the number density, and λ_D is the electronic Debye length.[36] As a consequence, it describes collective effects due to long-range Coulomb forces, but does not include particle discreteness effects such as particle-particle encounters. Since its solution contains no thermal fluctuations of macroscopic quantities, such as the electric field, charged particle density, etc., the behavior of very small amplitude waves can be simulated in a quantitatively accurate manner.

In contrast, the particle simulation model, or 'particle code' as it is often termed, incorporates the full dynamics of particles and waves, including discreteness effects. However, fluctuations are at an unrealistically high level, since the number of particles that a computer can handle is many orders of magnitude less than in typical plasmas. These large fluctuations can obscure the small amplitude oscillations described by linear theory. Hence, quantitative results are not easily

available in the linear régime, even though the qualitative behavior agrees with theory; the particle code is better suited to simulation in the nonlinear régime, where the ratio (wave field energy/particle thermal energy) $\gtrsim$ 0.01. In this respect, it should be noted that the expansion methods discussed in Section 2.2.2 may limit the amplitude of the perturbations that can be handled in order to assure the rapid convergence of the expanded series. It should also be noted that the expansion methods impose a restriction on the class of perturbations that can be treated. For example, in the Fourier-Hermite method of Section 2.2.2, the velocity distribution function is automatically an entire function of velocity.[3] Consequently, the problem must be such that the distribution function is describable in terms of an entire function of velocity; we could not consider the evolution of a delta-function distribution.

3.1.2 Ease of Computation

From the computational point of view, it is much more difficult to solve the Vlasov equation numerically than to solve the Newton equation. Numerical instability such as is encountered in the finite difference method, and the Fourier-Hermite method, is difficult to overcome. Solution of the Newton equation is not subject to this difficulty. In addition, the algorithm for solving the Vlasov equation is more complicated and lengthy than for the Newton equation.

One point of practical importance is that the Vlasov approach enables different effects to be studied separately. For example, the linearized Vlasov equation can be solved to study linear behavior alone. The effects of nonlinearity can then be assessed by adding the nonlinear

terms. The effect of free-streaming particles can also be studied independently. This feature of the Vlasov approach helps materially in understanding the physics of plasmas.

The particle code requires a very large computer memory to store information on the positions and velocities of the particles, and on the field variables, since it follows the motion of the particles step-by-step in time. Even with modern, large, high-speed computers, simulations in three dimensions may not be economically feasible, since the number of particles that is needed, to maintain the same level of fluctuations as in one dimension, has to be increased as N^3 .

In contrast, the Vlasov approach needs much smaller computer memory for the time-varying field quantities on the grid points, or the time-varying expansion coefficients, since the velocity distribution carries information on the charged particles in highly compact form.

To ease the computational difficulties, some combination of the two approaches would clearly be desirable. This is provided by the hybrid approach to be described next. It is a particle simulation model in the sense that the motions of a large number of particles are followed in time. The particles do not keep their identities, however, and there are similarities to the Vlasov approach in that the value of the velocity distribution function is defined on a grid in phase-space, as in the finite difference methods described in Section 2.2.1.

3.2 Hybrid Approach

Our model is constructed using the CIC model described in Section 2.3.2. In addition to the usual spatial grid, we introduce a grid in velocity-space, and represent the particles by points in

(x-v) phase-space as shown in Fig. 3.1. The phase-space is consequently covered with a rectangular grid of dimensions Δx, Δv. The velocity grid extends from v_1 to v_2, where v_1 and v_2 are chosen such that the numbers of particles with velocities in the intervals $v < v_1$ or $v > v_2$ are negligible.

In the work of Denavit,[6] the Lewis variational method[25,26] was used to construct a model. In the Denavit model, finite-size particles are chosen to have a triangular spatial distribution, instead of the uniform charge distribution of the CIC model. The numerical scheme based on that model turned out to be more complicated, therefore more time-consuming, than our model. In addition, although his scheme is energy-conserving, it does not conserve momentum, whereas the CIC scheme is formulated in such a way as to conserve momentum.[31] The non-conservation of momentum indicates the existence of self-force, i.e., a particle is effected by the force due to the field that is created by itself, which is nonphysical. The energy-conserving feature of the Denavit scheme may not be very useful in practice, since energy conservation is exact only in the limit of a vanishingly small time-step.

In creating a plasma with a Maxwellian velocity distribution, our model employs the following method. The particles are equally divided into a number of velocity groups. All the particles in one group are assumed to have the same velocity, v, and mass and charge are assigned to them in proportion to $\exp(-v^2/2v_t^2)$, where v_t is the electron thermal velocity. This is shown schematically in Fig. 3.1. Since the charge-to-mass ratio is the same for all of the particles, the acceleration is also the same. One of the advantages of this method of

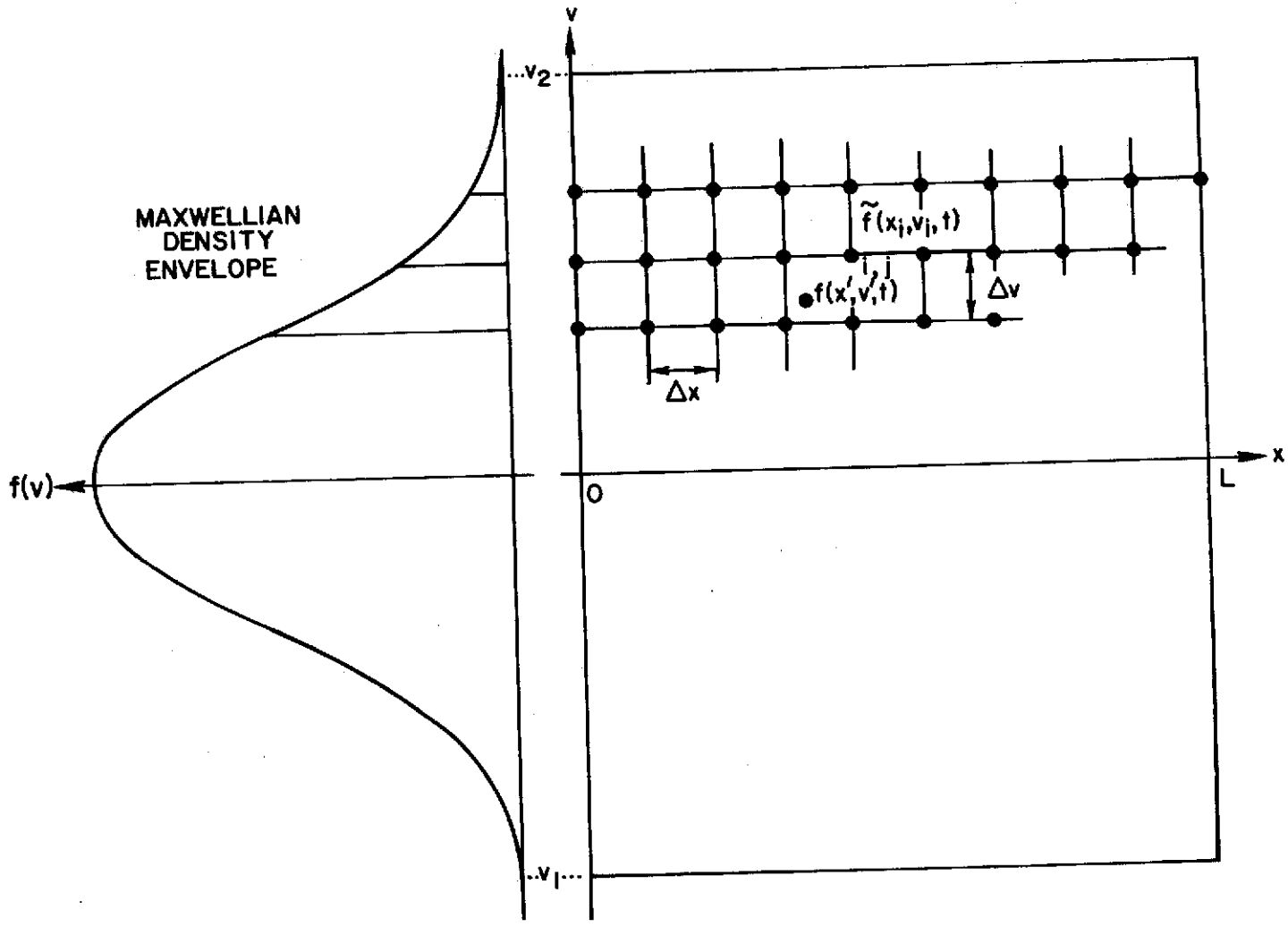

FIG. 3.1. Phase-space covered with a rectangular grid, and a Maxwellian velocity distribution approximated by beams.

generating a Maxwellian distribution by weighted particles is that improved resolution is provided in the tail of the velocity distribution, compared with a Maxwellian distribution with identical particles.

The system is set up at time $t = 0$ using the quiet start technique to be described below, and proceeds as in a CIC model. After a certain number of time-steps, the distribution function is reconstructed at the grid points by periodic smoothing, and is interpreted as representing a distribution of new discrete particles. The motions of these particles are followed until the next reconstruction.

With these procedures in mind, we shall describe the quiet start technique, and the periodic smoothing, which are essential parts of the hybrid approach. As proposed by Denavit, they are used to achieve a very low fluctuation level, and to allow the model to be applied to a wide range of linear and nonlinear problems.

3.2.1 Quiet Start

The quiet start technique, proposed by Byers, is a method of eliminating macroscopic fluctuations in a particle code at early stages of evolution.[37] This is done by placing the particles only on the equilibrium trajectories in phase-space at time $t = 0$. As an example, consider an electrostatic, one-dimensional problem with a periodic boundary condition, in which the equilibrium particle trajectories are straight lines, $v = \text{const}$. At time $t = 0$, the particles are loaded uniformly at the grid points in phase-space, as shown in Fig. 3.1. We shall assume that the particles are of finite extent, as in the CIC method of Section 2.3.2, with extension equal to the spatial grid size, Δx. Since the charges are distributed uniformly in

space, there is no macroscopic electric field at $t = 0$. We easily see that at subsequent times the phase-space looks the same as at $t = 0$, except that the centers of the finite-size particles are shifted in the x-direction by distances depending on their velocities. Thus, there continues to be no macroscopic electric field unless a perturbation is applied.

In principle, the quiet start technique provides a noiseless system. In practice, round-off errors due to the finite number of digits representing the numbers in the computer introduce some fluctuations. However, this level is many orders of magnitude lower than that in the particle codes. Typically, we have obtained about 60 dB reduction. This is quiet enough to study linear plasma behavior, and compare its features with theoretical predictions.

Although the quiet start technique works well at early times, it eventually causes wave growth; it ceases to be effective after a time, $2\pi/(k_m \Delta v)$, where k_m is the maximum wavenumber possible in the system.[6] This breakdown occurs because the velocity distribution of the particles is being replaced by a set of discrete beams. Such a system is subject to streaming instability, to be described in Section 3.3, even if the envelope of the beam density is Maxwellian.[38] Periodic smoothing may by used to combat this instability.

3.2.2 Periodic Smoothing

Periodic smoothing constitutes a periodic averaging of the distribution function in phase-space.[6] It can be expressed by

$$\tilde{f}(x,v,t) = \iint f(x',v',t) w_x(x - x') w_v(v - v') dx' dv' \,, \qquad (3.1)$$

where w_x and w_v are weighting functions for coordinate- and velocity-space, $\tilde{f}$ is the averaged distribution function, and the integration is over the whole of phase-space. The averaging process expressed by Eq. (3.1) causes diffusion of the distribution function. The weighting functions are chosen so that this diffusion quenches the streaming instability without introducing other undesirable effects. Specific forms of the weighting functions, and their derivation, are given in the Appendix.

In particle models with a phase-space grid such as that shown in Fig. 3.1, the integral in Eq. (3.1) reduces to a sum over the collection of particles, and we want to find the averaged distribution function, $\tilde{f}$, at the phase-space grid points. If $f(x',v',t)$ is taken to be the mass of a finite-size particle, the center of which is located at (x',v') at time t, then Eq. (3.1) implies that the value of $\tilde{f}$ at the (i-j) grid point, (x_i,v_j), is obtained by distributing the mass of each particle among the neighboring grid points according to the weighting prescribed by w_x and w_v. This is a reconstruction of the distribution function from a given distribution of particles. In this model, the reconstructed distribution function is defined only at the grid points, and is interpreted as the new particle mass located at each grid point. Their motions are governed by the Newton equation, as in other particle codes. Reconstruction of the distribution function does not need to be done every time-step. It is simply done frequently enough to suppress the streaming instability, as described in Section 3.3.

3.3 Streaming Instability and Recurrence Phenomenon

In this section we shall discuss two phenomena associated with the use of the quiet start technique: streaming instability, and possibility of recurrence of the initial state.

3.3.1 Streaming Instability

Treating each beam as a continuous fluid of charged particles, neglecting collisions, and linearizing the one-dimensional fluid equations for electrons, yields

$$\frac{\partial v_j}{\partial t} + V_j \frac{\partial v_j}{\partial x} = - \frac{e}{m_e} E \ , \qquad \frac{\partial n_j}{\partial t} + N_j \frac{\partial v_j}{\partial x} + V_j \frac{\partial n_j}{\partial x} = 0 \ , \quad (3.2)$$

where N_j, V_j, n_j, and v_j are zeroth and first order densities and velocities for the j-th beam. Assuming a solution of the form $A(x,t) = A(\omega,k) \exp[-i(\omega t - kx)]$ for the first order quantities, we have

$$- i\omega v_j + ikV_j v_j = - \frac{e}{m_e} E \ , \qquad - \omega n_j + k v_j N_j + k V_j n_j = 0 \ . \quad (3.3)$$

Coupling Eq. (3.3) with the Poisson equation,

$$ikE = - \frac{e}{\epsilon_0} \sum_j n_j \ , \quad (3.4)$$

yields the following dispersion relation for longitudinal oscillations of the beam system

$$1 = \frac{e^2}{m_e \epsilon_0} \sum_j \frac{N_j}{(\omega - kV_j)^2} \ , \quad (3.5)$$

where we have assumed that the positive ions form an immobile neutralizing background.

We introduce $F_j(V)$ by

$$\delta F_j(V_j) = N_j(V_j) , \qquad V_j - V_{j-1} = \delta , \tag{3.6}$$

where the beams are spaced with equal velocity difference, δ . Equation (3.5) can now be written as

$$1 = \omega_p^2 \, \delta \sum_j \frac{F_j}{(\omega - kV_j)^2} , \tag{3.7}$$

where ω_p is the electron plasma frequency. Dawson has shown that, in the limit $\delta \to 0$, Eq. (3.7) may be written as the sum of an integral and a singular term,[38]

$$1 = \frac{\omega_p^2}{k} \, \mathcal{P} \int \frac{F(V)}{\omega - kV} \, dV - \frac{\pi \omega_p^2}{k^2} \, F' \left(\frac{\omega}{k}\right) \cot \left(\frac{\pi \omega}{\delta k}\right)$$

$$+ \frac{\pi^2 \omega_p^2 F(\omega/k)}{\delta k^2 \sin^2(\pi\omega/\delta k)} , \tag{3.8}$$

where $\mathcal{P}$ denotes the Cauchy principal part of the integral, and $F' = dF/dV$.

In order for Eq. (3.8) to have a solution, the second and third terms on the right hand side have to be finite when $\delta \to 0$. This requirement on the third term yields

$$\text{Im } \omega \simeq \pm \frac{k\delta}{2\pi} \ln \delta , \tag{3.9}$$

which demonstrates the existence of unstable modes. Substitution of

this, and use of a Maxwellian velocity distribution $F(V) = \exp(-V^2/2v_t^2)/(2\pi)^{1/2}v_t$, in Eq. (3.8) gives finally,

$$\frac{4\pi^2}{(2\pi)^{1/2}}\left(\frac{v_t}{\delta}\right)\exp\left(-z^2 \pm i\,\frac{2\pi\omega}{\delta k}\right) = 1 + k^2\lambda_D^2 + zZ(z) \,, \qquad (3.10)$$

where Z is the plasma dispersion function,[32] with $z = \omega/(2^{1/2}kv_t)$. The positive sign in Eq. (3.10) is to be used for $\mathrm{Im}\,\omega > 0$, and the negative sign for $\mathrm{Im}\,\omega < 0$.

The dispersion relation expressed by Eq. (3.10) has two complex conjugate roots for each value of k . Writing $\omega_j = \alpha_j + i\beta_j$, $\xi_j = j\delta/(2^{1/2}v_t)$ yields

$$\alpha_j = \frac{k\delta}{2\pi}\tan^{-1}\left(\frac{\xi_j\,\mathrm{Im}\,Z(\xi_j)}{1 + k^2\lambda_D^2 + \xi_j\,\mathrm{Re}\,Z(\xi_j)}\right) + kj\delta \,,$$

$$\beta_j = \pm\frac{k\delta}{2\pi}\left\{\ln\left(4\pi^2 v_t/2^{1/2}\pi\delta\right) - \xi_j^2 \right. \qquad (3.11)$$

$$\left. - \frac{1}{2}\ln\left(\left[1 + k^2\lambda_D^2 + \xi_j\,\mathrm{Re}\,Z(\xi_j)\right]^2 + \left[\mathrm{Im}\,Z(\xi_j)\right]^2\right)\right\} .$$

Each value of j denotes a particular beam, so there are clearly two modes for each beam. These are the normal modes of the many-beam system, with a Maxwellian envelope, for a given wavenumber k . Any small amplitude macroscopic behavior can be expressed as a weighted sum of these modes. Equation (3.11) is valid only in the limit $\delta \to 0$. Note that β_j vanishes as $\delta \to 0$.

Figure 3.2 is a computer simulation of the behavior of the streaming instability. The total electric field energy is plotted against time for two cases. In both, the total field energy starts

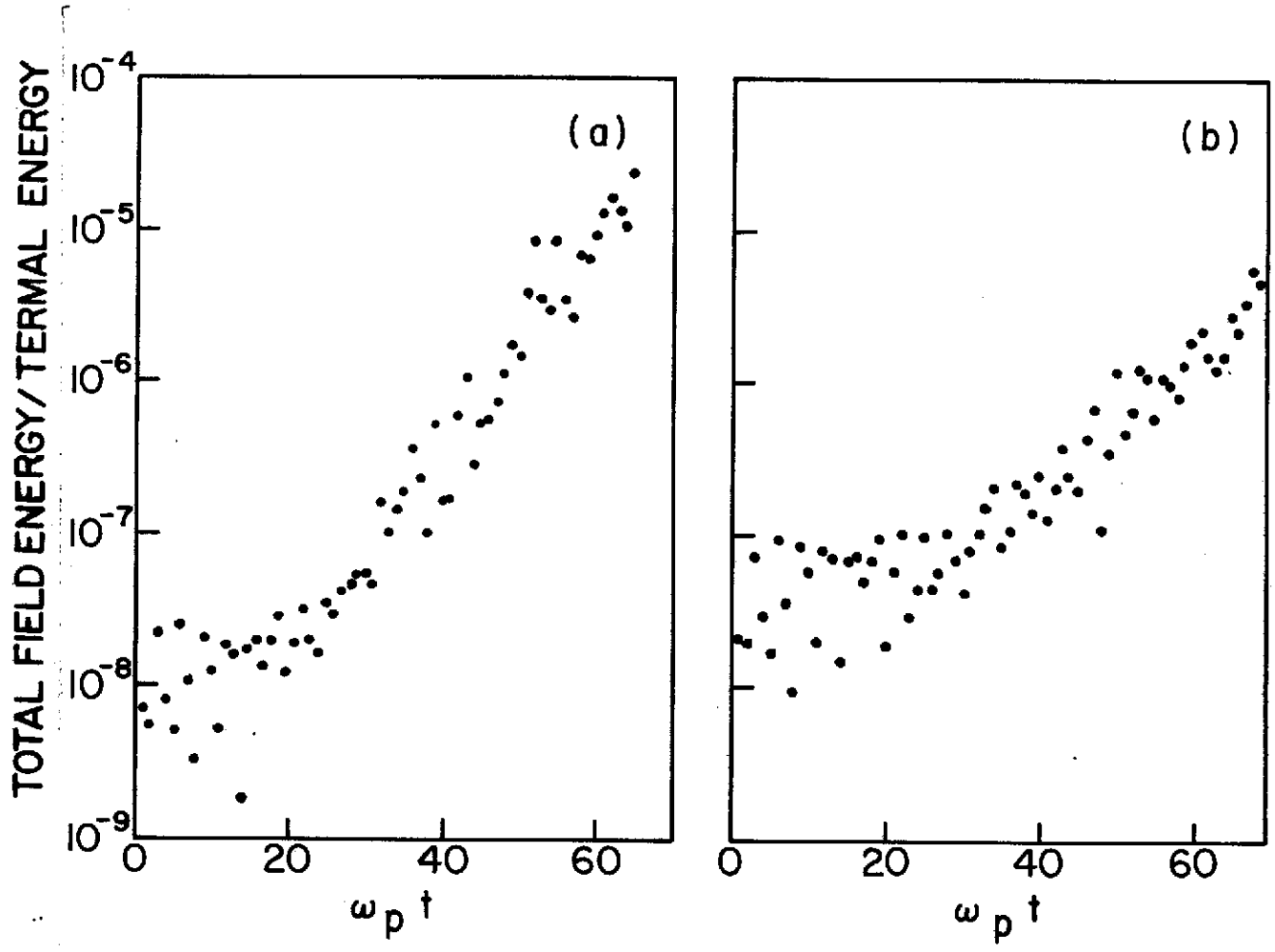

FIG. 3.2. Streaming instability. [L = 128 Δx, H = $\Delta x = \lambda_D$, $\delta = \Delta v$, $v_1 = -4v_t$, $v_2 = 4v_t$, $\omega_p \Delta t = 0.25$]
(a) $\delta = v_t/8$, 8192 particles, 64 beams.
(b) $\delta = v_t/16$, 16384 particles, 128 beams.

growing almost exponentially after a certain period of time. The observed growth rate is about $0.09\omega_p$ for $\delta = v_t/8$, and about $0.05\omega_p$ for $\delta = v_t/16$. From these results, we may conclude that it is possible to carry out simulations at early times during which the field energy associated with wave phenomena of interest is much larger than the total energy of the fluctuating fields. In Fig. 3.2, for example, a perturbation with electrostatic energy of 10^{-4} times the thermal energy may be studied up to $\omega_p t \simeq 40$ for $\delta = v_t/8$, and longer for $\delta = v_t/16$.

In practice, δ cannot always be made as small as is desirable, because the smaller δ is to be, the more particles are necessary. Also, it is often necessary to follow the behavior in nonlinear problems for considerable periods of time. Making the beam spacing δ small enough for such a simulation may become prohibitively expensive. As is shown in Section 3.4, periodic smoothing makes a long-time simulation possible with a relatively small number of beams.

3.3.2 Recurrence Phenomenon

In a simulation using the quiet start tehcnique, a perturbation with wavenumber k first damps to a low level at the Landau damping rate[39], and then reappears suddenly at time $t = 2\pi/k\delta$ with higher amplitude than its initial one. After its reappearance, the perturbation decays with a damping rate slightly different from the Landau damping rate. This is clearly demonstrated by Fig. 3.3, which was obtained from a result of our simulation. This recurrence results from approximating the continuous distribution function by a finite number of delta-function beams: the perturbation with wavenumber k on each beam

comes back into phase after a time $\tau_R = 2\pi/k\delta$, and with larger amplitude than its initial value due to the streaming instability. This phenomenon was also observed by Denavit.[6] In the limit of infinitely many beams, phase-mixing prevents recurrence of the initial state. Similar recurrence phenomena have been observed in the numerical solution of the Vlasov equation by the Fourier-Hermite method,[40] the finite difference method,[40] and the Lewis variational method.[41]

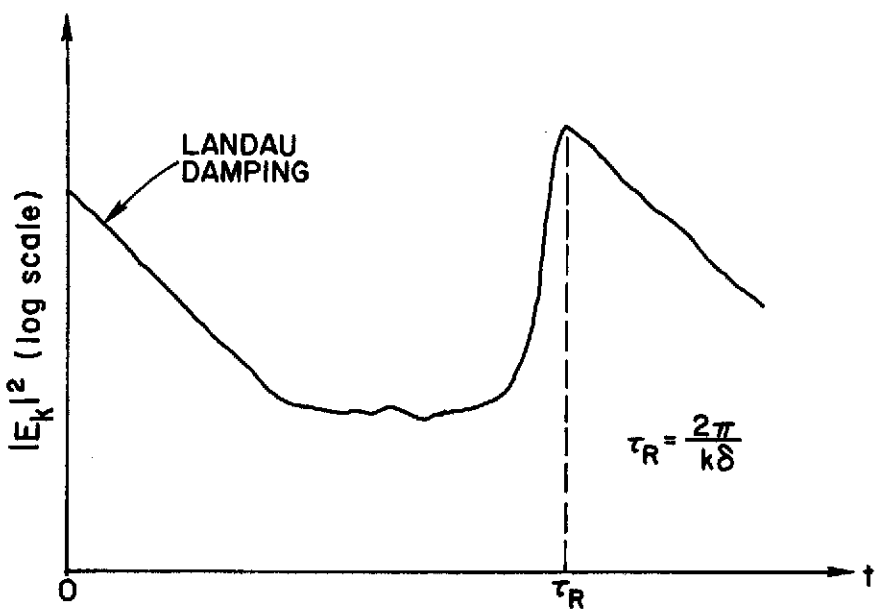

FIG. 3.3. Recurrence of initial state. Wavenumber and recurrence time are given by $k\lambda_D = 3\pi/16$, and $\omega_p\tau_R \simeq 75$. [$\delta = v_t/7$, N = 2048, L = 32 Δx, H = $\Delta x = \lambda_D$, $\delta = \Delta v$, $v_1 = -4.5v_t$, $v_2 = 4.5\ v_t$, $\omega_p\Delta t = 0.25$] .

The recurrence phenomenon has not been found to pose any problems in our simulations to be described in Sections 4-6. For example, it is observed that a growing perturbation does not show any irregularity at $t = \tau_R$. Another example is that of a large amplitude wave, which involves particle trapping; as is seen in Section 4, the behavior of the wave demonstrates no irregularity at the recurrence time, τ_R . We may conclude that in strongly nonlinear cases, or in unstable situations, the recurrence phenomenon is not significant. It should be noted that periodic smoothing alone would not suffice to prevent the recurrence.

3.4 Diffusion in Phase-Space

Since the weighting functions mentioned in Section 3.2.2, and derived in the Appendix, do not conserve all of the moments of the velocity distribution function when the smoothing expressed by Eq. (3.1) is performed, a diffusion of the distribution function occurs in phase-space due to reconstruction. In this section, the diffusion rate is estimated following Denavit.[6]

Before smoothing, the microscopic distribution function is given by

$$f(v) = \sum_j f_j \delta(v - v_j) \ , \tag{3.12}$$

where f_j represents the mass of particle j , with velocity v_j , and $\delta(v)$ is the Dirac delta-function. The smoothed distribution function is

$$\tilde{f}(v) = \frac{1}{\Delta v} \sum_j f_j w(v - v_j) \ , \tag{3.13}$$

where $w(v)$ is the weighting function, and Δv is the velocity grid size.

Introducing the Fourier transforms of $f(v)$ and $\tilde{f}(v)$,

$$H(q) = \int_{-\infty}^{\infty} f(v) \exp(iqv)dv = \sum_j f_j \exp(iqv_j) ,$$

$$\tilde{H}(q) = \int_{-\infty}^{\infty} \tilde{f}(v) \exp(iqv)dv = W(q) \sum_j f_j \exp(iqv_j) , \tag{3.14}$$

where $W(q)$ denotes the Fourier transform of the weighting function $w(v)/\Delta v$, we obtain

$$\tilde{H}(q) = W(q)H(q) . \tag{3.15}$$

A plot of $W(q)$ is shown in Fig. 3.4 for the weighting functions given in the Appendix. Since q represents frequency of velocity-space oscillation, Eq. (3.15) implies that the fine structure of the distribution function in velocity-space is smoothed out by reconstruction.

To estimate the diffusion rate, we define

$$D(q) = 1 - W(q) . \tag{3.16}$$

Then, after m reconstructions, we have

$$\tilde{H}_m(q) = [1 - D(q)]^m H(q) . \tag{3.17}$$

Since $D(q) \ll 1$, for $q\Delta v/\pi \gg 1$, Eq. (3.17) may be approximated in this region by

$$\tilde{H}_m(q) \simeq \exp[-mD(q)] H(q) . \tag{3.18}$$

Thus, $D(q)$ represents the diffusion rate of a feature of scale $2\pi/q$.

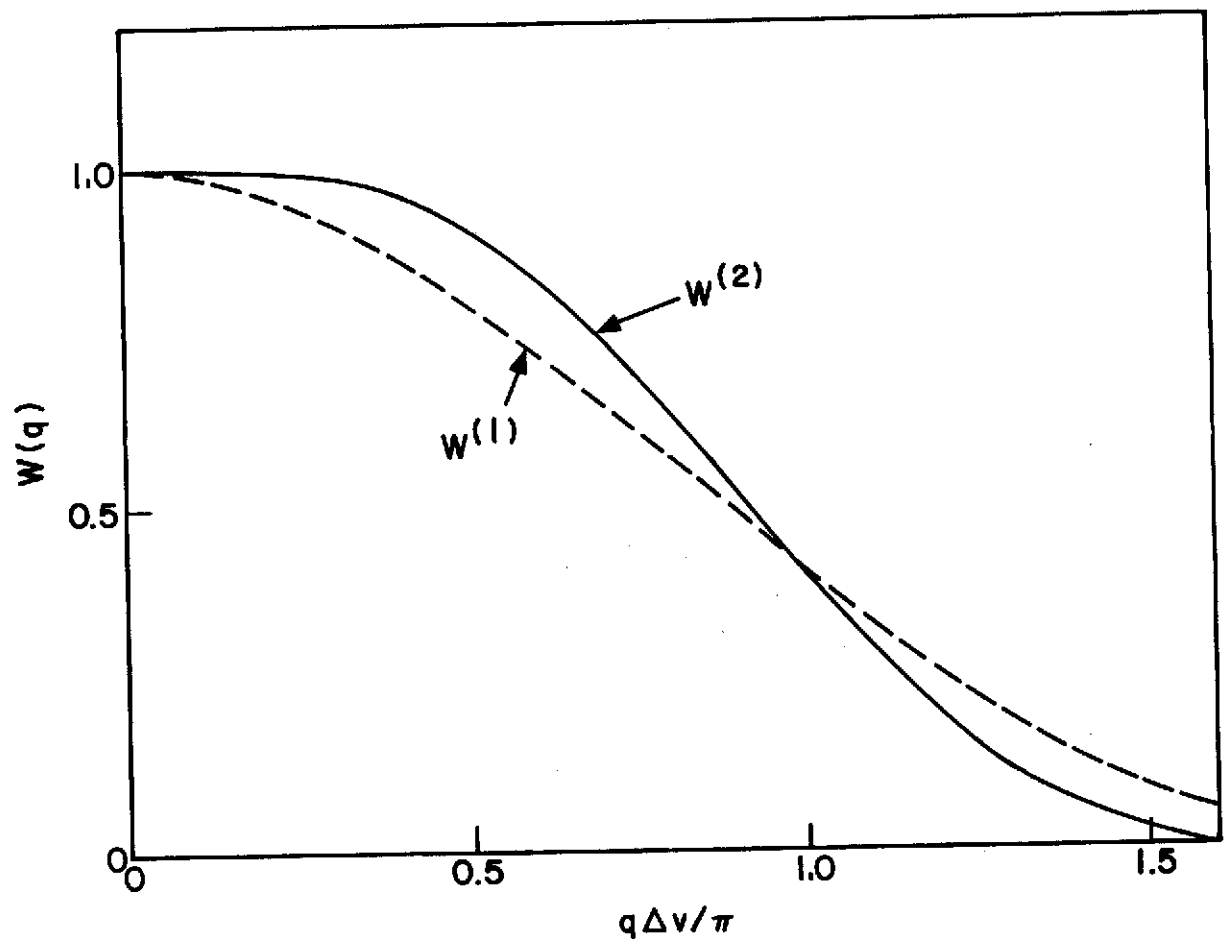

FIG. 3.4. Fourier transform of linear $[w^{(1)}]$ and quadratic $[w^{(2)}]$ weighting functions. (Adapted from Fig. 4 of Ref. 6.).

In order to suppress the streaming instability, features of scale-length $q \simeq \pi/\Delta v$ have to be smoothed out. Consider a perturbation with wavenumber k. The growth rate of this perturbation due to the streaming instability is obtained from Eq. (3.11) as

$$\beta \simeq \frac{k\Delta v}{2\pi} \ln \frac{v_t}{\Delta v} , \tag{3.19}$$

when Δv is small, where $\delta = \Delta v$ has been assumed. Assuming that the instability is suppressed by balancing this growth with the attenuation due to diffusion, we can obtain the frequency with which reconstruction is necessary. Thus, from

$$\exp\left(t \frac{k_m \Delta v}{2\pi} \ln \frac{v_t}{\Delta v}\right) W(q) \lesssim 1 \qquad \left(q \simeq \frac{\pi}{\Delta v}\right) , \tag{3.20}$$

we have,

$$t \lesssim \tau_s \equiv \frac{2\pi}{k_m \Delta v} \left[\frac{\ln(1/W)}{\ln(v_t/\Delta v)}\right] , \tag{3.21}$$

where τ_s is the time interval within which at least one reconstruction is necessary.

Substituting $k_m = \pi/\Delta x = \pi/\lambda_D$, $v_t/\Delta v = 7$, which will be used in most of our simulations in subsequent sections, and $q \simeq \pi/\Delta v$, $W(q) \simeq 0.4$ (obtained from Fig. 3.4 for the quadratic weighting function), into Eq. (3.20), yields

$$\omega_p \tau_s \simeq 7 . \tag{3.22}$$

So far, we have only discussed diffusion in velocity-space. Diffusion in coordinate-sapce is treated in the same way. Replacing

v and q , by x and k , in Eqs. (3.16)-(3.18), indicates that there is attenuation of short wavelength perturbations at a rate given by

$$\tilde{H}_m(k) \simeq \exp[-mD(k)]\, H(k) \ , \qquad (3.23)$$

after m reconstructions.

3.5 Some Tests of the Hybrid Model

To test the hybrid model, Denavit chose two-stream instability, and obtained good agreement with results from the particle code[11,20,42] and the Vlasov approach.[11] However, his simulations were carried out at relatively high electrostatic energy levels, i.e. 10^{-3} - 10^{-2} times the total energy, which is to be compared with an order of 10^{-6} in our tests to be described in Section 3.5.2.

We shall now present some results of test runs with our model, first on the equilibrium behavior of a Maxwellian plasma, and then on linear wave propagation when the system is perturbed. The results will be compared with theoretical predictions.

3.5.1 Equilibrium Behavior

Our first numerical experiments were carried out on a Maxwellian plasma with no applied perturbation or external excitation. The most important parameters are the number of time-steps, N_s , after which the smoothing operation is repeated, and the beam spacing, δ .

In Fig. 3.5, the total field energy is plotted against time for $\delta = v_t/7$. It will be seen that by increasing the frequency of smoothing, i.e. decreasing N_s , the streaming instability is suppressed; for $N_s \leq 32$, the field energy stays roughly constant throughout the simulation run. To study this further, the initial energy spectrum,

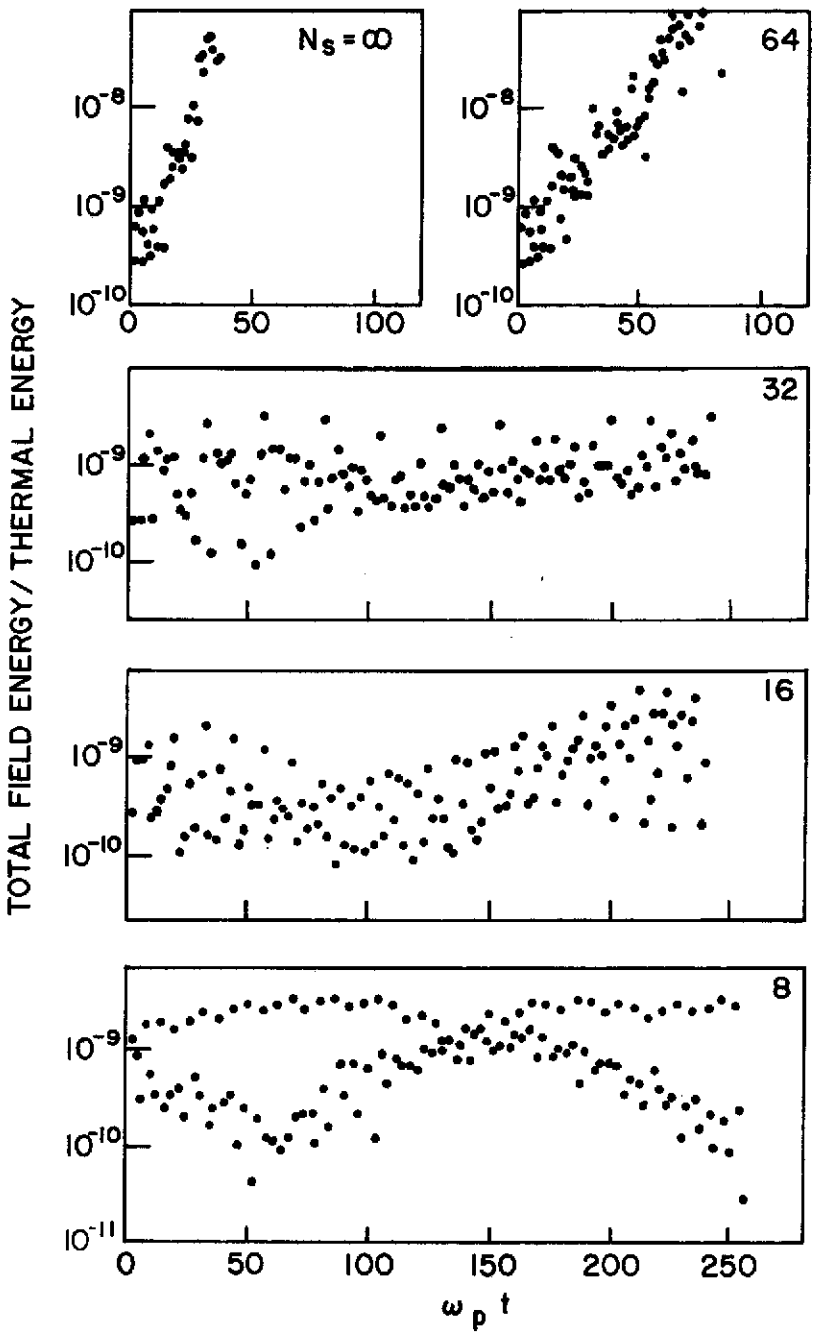

FIG. 3.5. Equilibrium behavior for various values of N_s. [$\delta = v_t/7$, $N = 2048$, $L = 32\ \Delta x$, $H = \Delta x = \lambda_D$, $\delta = \Delta v$, $v_1 = -4.5\ v_t$, $v_2 = 4.5\ v_t$, $\omega_p \Delta t = 0.25$].

and the time averaged energy spectrum are shown in Fig. 3.6. The energy spectrum for $N_s = 32$ shows that mode energy tends to increase as time increases. For $N_s = 16$ and 8, the mode energy seems to stay at roughly the same level, i.e., the streaming instability is stabilized. This observation agrees with the rough estimate given by Eq. (3.22). The total energy of the system, i.e., the particle kinetic energy plus the field energy, was found to be conserved to within 0.1% up to $\omega_p t \simeq 270$.

In Figs. 3.7 and 3.8 are plotted analogous results to Figs. 3.5 and 3.6 for $\delta = v_t/14$. As expected, the growth rate of the field energy is greatly reduced compared with the case, $\delta = v_t/7$. Figure 3.8 seems to indicate that values of N_s between 16 and 32 are adequate to suppress the streaming instability.

The important fact here is that for stable cases the total field energy is fluctuating at a level 10^{-8} times lower than the thermal energy of the plasma during the whole run. Since the level of fluctuations in the particle model for a system of length $32\lambda_D$ with 4096 particles is of the order of 10^{-3} - 10^{-2} times the thermal energy, we have achieved 50 - 60 dB reduction in fluctuations.

3.5.2 Linear Wave Propagation

The purpose of this simulation was to verify predictions of Landau damping for electron plasma waves.[39] Waves were excited at $t = 0$ by applying the perturbations

$$\Delta x_i = \epsilon\lambda_D \cos kx_i , \qquad \Delta v_i = \epsilon v_t \sin kx_i , \tag{3.23}$$

where x_i , Δx_i , and Δv_i are the position, displacement, and velocity

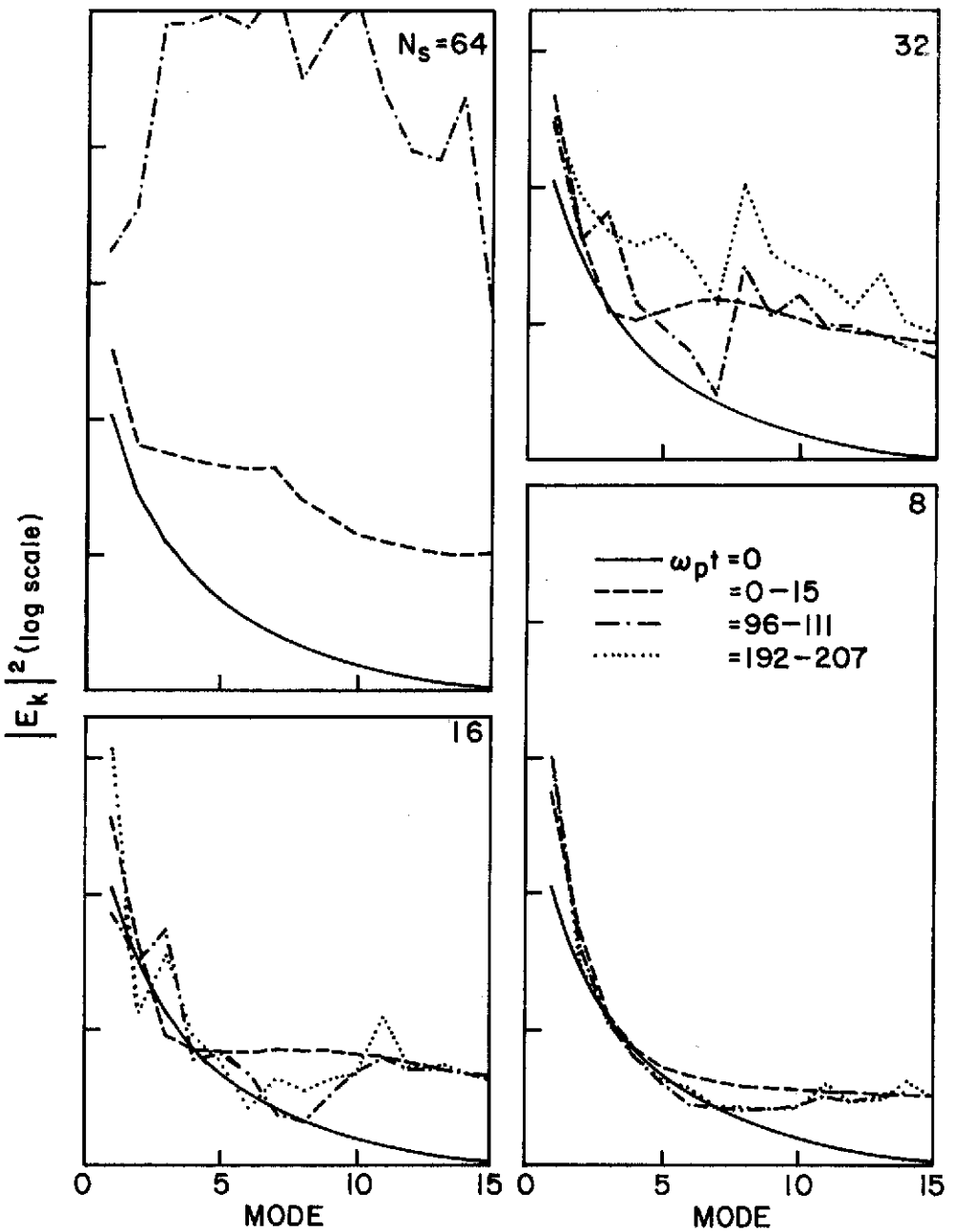

FIG. 3.6. Time-averaged energy spectrum of the system shown in Fig. 3.5.

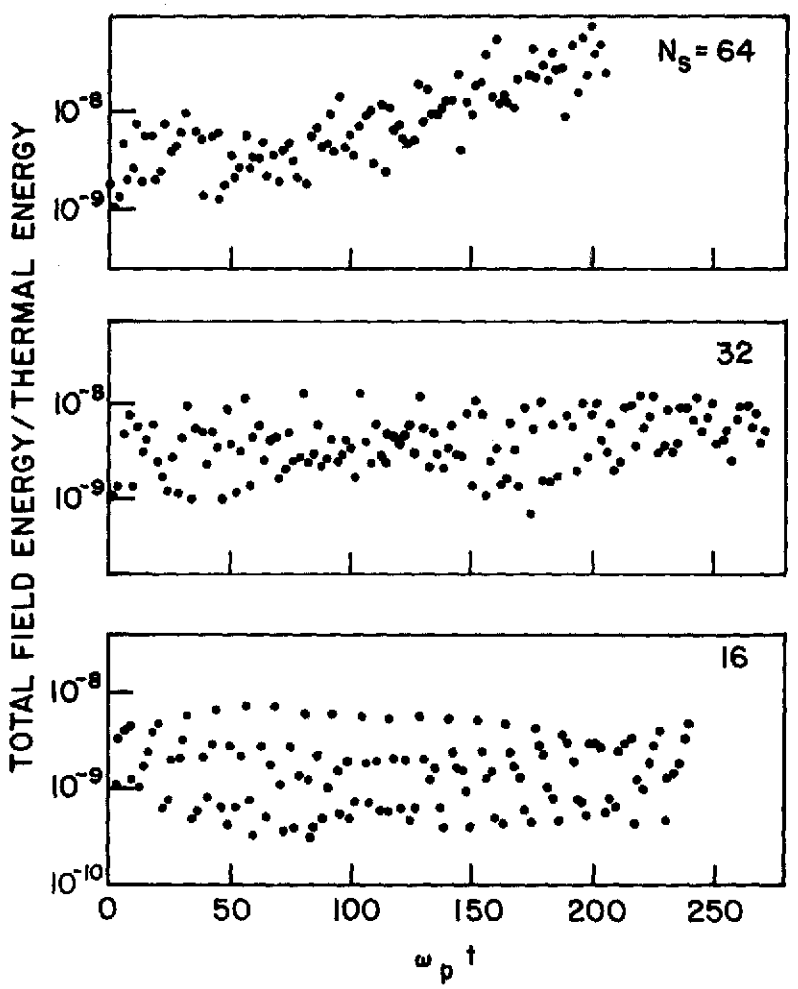

FIG. 3.7. Equilibrium behavior for various values of N_s. [$\delta = v_t/14$, $N = 4096$, $L = 32\ \Delta x$, $H = \Delta x = \lambda_D$, $\delta = \Delta v$, $v_1 = -4.54\ v_t$, $v_2 = 4.54\ v_t$, $\omega_p \Delta t = 0.25$] .

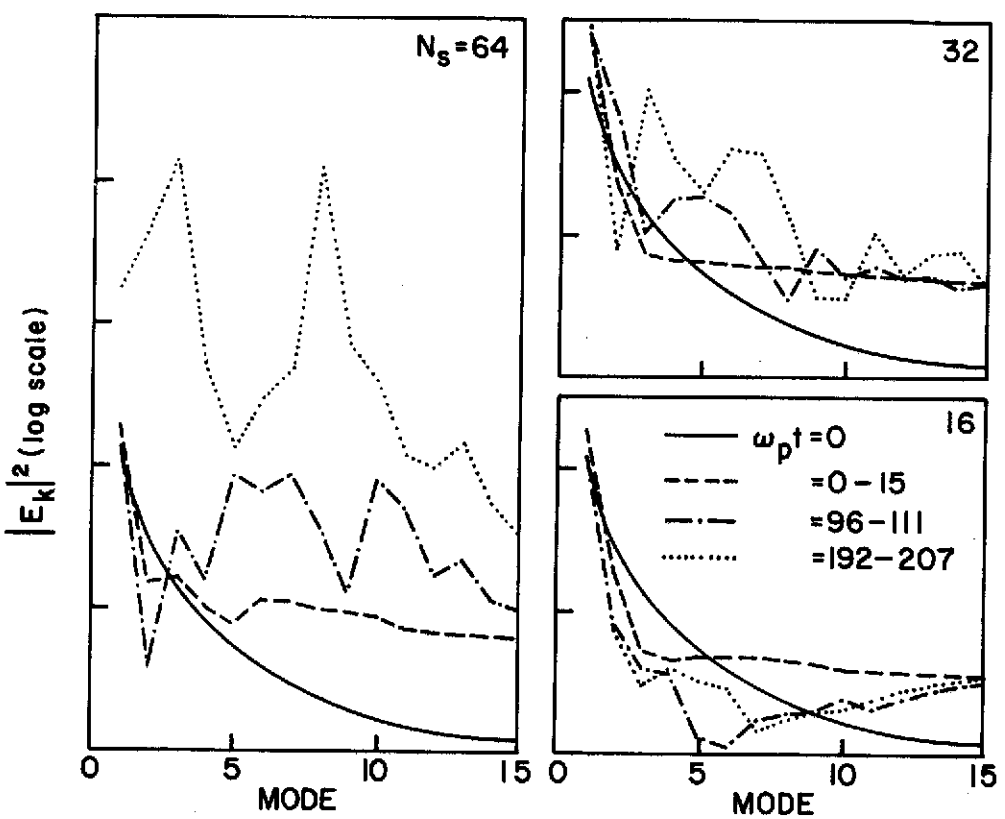

FIG. 3.8. Time-averaged energy spectrum of the system shown in Fig. 3.7.

perturbation of particle i, ϵ is the amplitude, and $k[= 2\pi n/L]$ is the wavenumber. In this simulation, only Mode 2 ($n = 2$, i.e., there are two wavelengths in the system) was excited. The results are shown in Fig. 3.9. For $N_s \leq 16$, there is excellent agreement with the theoretical prediction by Langdon,[31] shown by solid lines, which takes into account finite-size particle effects and spatial grid effects.

Although the fluctuation amplitude in Fig. 3.9 increases with time, it is important to note that the ratio of electrostatic energy to thermal energy, $[(eE/m_e\omega_p)^2/v_t^2]$, at $t = 0$ is 4.25×10^{-6} in this simulation. Particle simulation with such good quality, at such a low electrostatic energy level, has not been feasible with previous models. For example, in order to reduce the fluctuation level to 10^{-6} times the thermal energy in a particle simulation with the same system length, it would require $10^3 - 10^4$ times more particles than are used in this simulation. Since the computing cost increases roughly in proportion to the number of particles, it would be prohibitively expensive. In contrast, the computing cost in this simulation was found to be less than twice that with the corresponding CIC model. Suppose the smoothing operation is performed every 16 time-steps. One smoothing operation in our computer code takes about 7 sec on an IBM 360/67 for 8192 particles. It is equivalent to an increase of about 0.44 sec per time-step. Since it takes our computer code about 0.75 sec per time-step for the CIC model with 8192 particles and a system with 128 cells, the total computing time per time-step is about 1.2 sec.

In addition to our check on temporal Landau damping of a signal, we have verified the predicted linear dispersion characteristics of

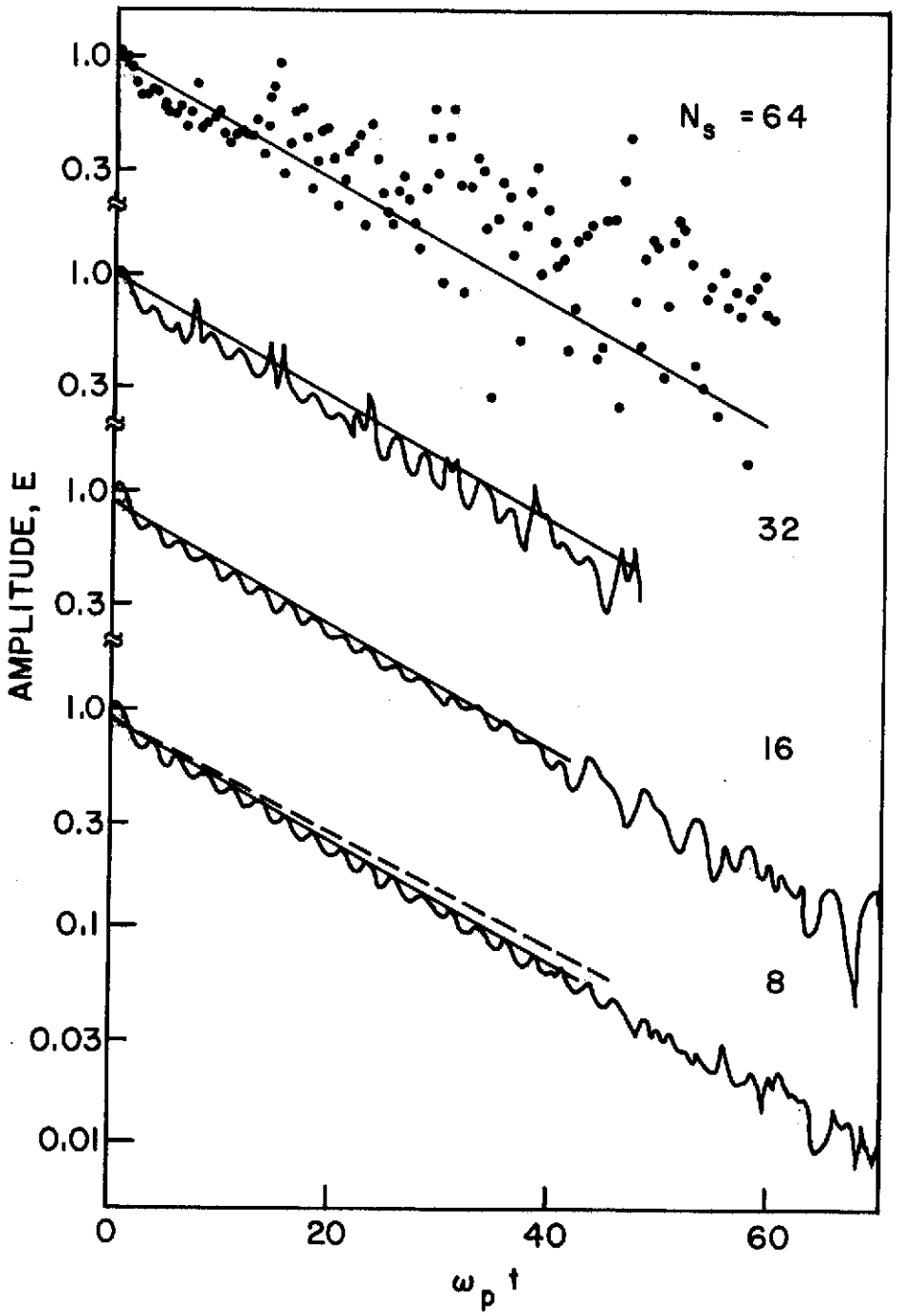

FIG. 3.9. Simulation of Landau damping. Solid lines are the prediction of the Langdon theory [Eq. (2.66), $\ell = 0$ term only]. Dashed line is the prediction of point particle theory.

electron plasma waves. The results are shown in Fig. 3.10, and agree well with theory. The initial perturbations were applied for Modes 7-20 with random phases. The electrostatic energy of the individual modes excited was about 4×10^{-6} times the thermal energy at $t = 0$.

The simulation results presented in this section serve to demonstrate that the hybrid approach provides quantitatively accurate results on the collective behavior of plasma in the linear régime. Since there is no reason why it should not be equally effective in the nonlinear régime, for which analytical results are not so readily available, the hybrid approach is clearly a powerful tool for plasma simulation. In succeeding sections, we shall employ it in the study of a number of nonlinear problems.

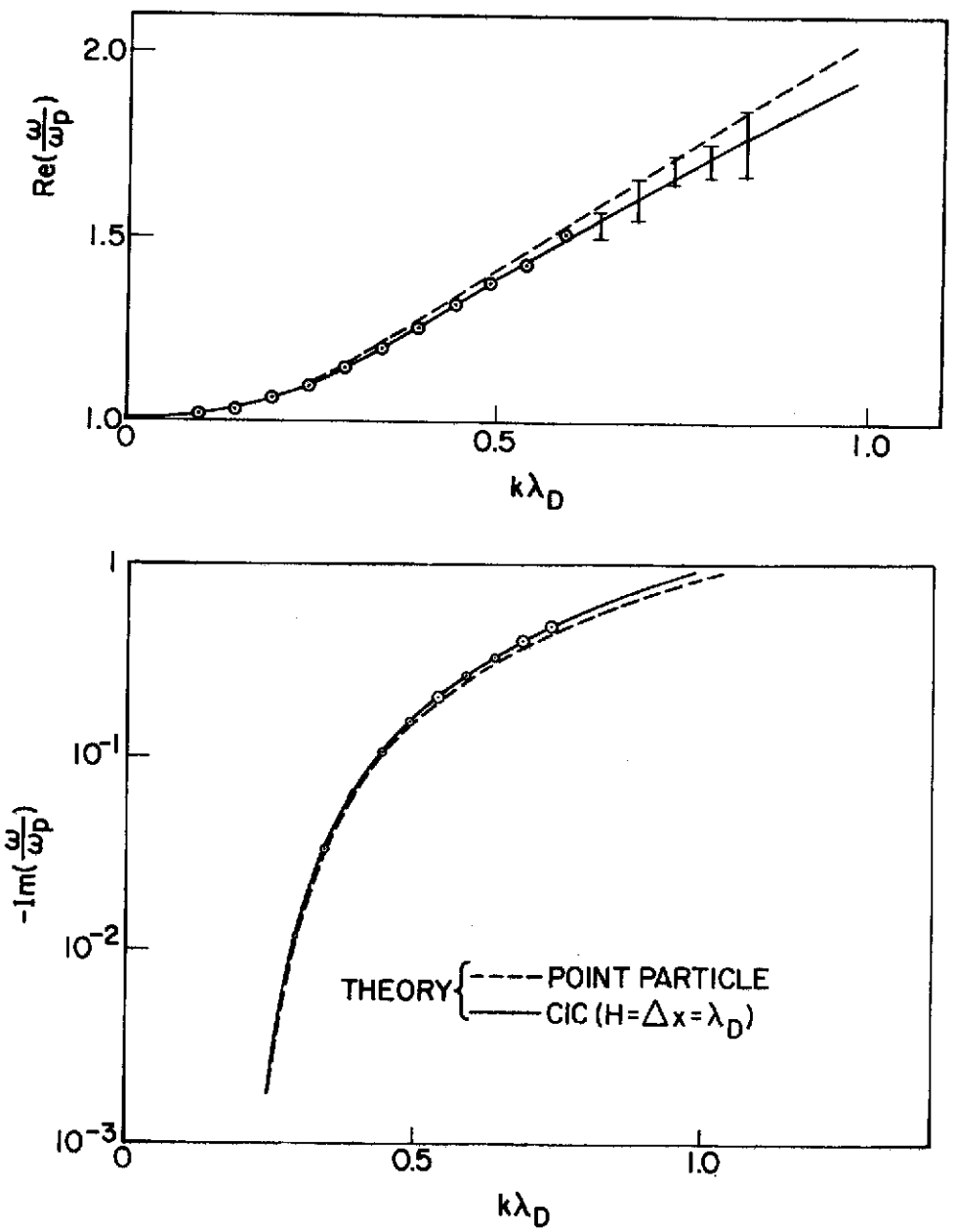

FIG. 3.10. Linear wave dispersion. Simulation results are shown by circles and bars whose sizes indicate errors involved. [$\delta = v_t/7$, $N_s = 16$, $N = 8192$, $L = 128\ \Delta x$, $H = \Delta x = \lambda_D$, $\delta = \Delta v$, $v_1 = -4.5\ v_t$, $v_2 = 4.5\ v_t$, $\omega_p \Delta t = 0.25$].

4. NONLINEAR BEHAVIOR OF MONOCHROMATIC PLASMA WAVES

4.1 Introduction

In Section 3.5.2, we have studied numerically the collisionless damping to which small amplitude longitudinal electron plasma waves are subject. This phenomenon is due to wave-particle interaction: charged particles moving faster than the wave transfer energy to it, while those moving slower absorb wave energy. In a Maxwellian plasma, where there are less fast particles than slow ones in the neighborhood of the wave phase velocity, a net absorption of energy by the particles occurs. Although first studied by Landau in 1946,[39] the predicted damping was not verified in laboratory experiments until about ten years ago. Spatial damping was then observed both for electron waves,[43-46] and ion waves.[47] It was also verified that the measurements of wave dispersion agree with theoretical predictions.

Since plasma is a highly nonlinear medium, the linearized analysis gives only a limited description of its behavior. The question arises of what will happen to Landau damping and wave dispersion when the wave amplitude is increased. Theroetical studies of this question were first made by O'Neil,[48] and Al'tshul and Karpman.[49] These authors found that the amplitude changes in time in an oscillatory manner, rather than being continuously attenuated. The amplitude oscillation is due to periodic exchange of energy between the wave and electrons trapped in the potential wells of the wave. The exchange occurs on a time scale of $1/\omega_B$, where $\omega_B[= (ekE_0/m_e)^{1/2}]$ is the bounce frequency of an electron oscillating at the bottom of a potential well, k is the wavenumber, and E_0 is the wave electric field amplitude.

The foregoing theories establish that Landau damping is valid only for short times, before particle trapping comes into play. The smaller the initial amplitude, the longer is the time for which the Landau solution applies. Because of analytical difficulties in dealing with phenomena involving particle trapping, the theoretical studies have been limited to special cases. For example, O'Neil assumed that the amplitude variation is so small that it may be neglected in calculating the particle orbits.[48] His theory is consequently valid only for $\gamma_L/\omega_B \ll 1$, where γ_L is the Landau damping rate. The same restriction applies to the theory of Al'tshul and Karpman.[49] Bailey and Denavit have taken into account the effects of the slowly-varying amplitude, and obtained essentially the same amplitude oscillation, except that the time at which the amplitude begins to grow again after the initial damping is delayed.[50] However, they still assume $\gamma_L/\omega_B \ll 1$. Gary has treated the case $\gamma_L/\omega_B > 1$ analytically, and shown that the wave starts to decay at a rate smaller than the Landau damping rate at a time when the linear theory is expected to break down.[51]

The restriction on γ_L/ω_B was removed in work by Sugihara and Kamimura, who investigated the behavior of Landau damping for a wide range of γ_L/ω_B values.[52] Recent work by Oei and Swanson has also taken into account the time-varying property of the bounce frequency.[53] They have obtained solutions for $0 < \gamma_L/\omega_B \leq 1$ which are similar to those of Sugihara and Kamimura. An important feature of the contributions by Sugihara and Kamimura, and Oei and Swanson, is that their theory is self-consistent: it includes the interaction of the electric field and the averaged particle velocity distribution. None of the other

theories mentioned so far is self-consistent. For example, O'Neil calculated the effect of the electric field on the particles, but not vice versa.

All of the theoretical studies discussed so far assume that the electric field is so small that the distribution function in the resonant region can be expressed by a Taylor expansion about the wave phase velocity up to the first order term in velocity. This condition may be written as $\omega/\omega_B >> (v_p/v_t)^2$, where v_p is the phase velocity of the wave (ω,k) . This is such a stringent condition that it is not easy to meet in laboratory experiments, especially when also satisfying the condition $\gamma_L/\omega_B << 1$.

A few experimental data on Landau damping of large amplitude waves have been reported. Malmberg and Wharton[54] observed spatial amplitude oscillation in qualitative agreement with the O'Neil theory[48] modified to fit the spatial case by Lee and Schmidt.[55] Oei and Swanson compared their theoretical results with the experiments of Malmberg and Wharton, and found agreement on the amplitude oscillation lengths but not on the detailed behavior of the amplitude.[53] One of the reasons may be that their experimental parameters do not meet the condition $\omega/\omega_B >> (v_p/v_t)^2$. Specifically, they have $\gamma_L/\omega_B \sim 0.1$ and $\omega/\omega_B \sim (v_p/v_t)^2$ for the results which exhibit amplitude oscillation. Franklin et al. have made detailed measurements of the spatial dependence of amplitude for electron plasma waves with different initial amplitudes, i.e., for different values of ω_B .[56] However, for large initial amplitude, they failed to obtain results in agreement with the theory. This was ascribed to the appearance of sideband growth due to trapped particle

instability.[57] Their experimental parameters for the measured results corresponding to $\gamma_L/\omega_B \lesssim 0.45$ yield $\omega/\omega_B \lesssim 4(v_p/v_t)^2$. This suggests that comparison of the available theories with the experiments is inappropriate.

In view of the foregoing difficulties, computer simulation suggests itself as a means of bridging the gap between the theoretical assumptions and readily attainable experimental parameters. It allows conditions to be studied for which analytical approaches are not tractable. Such simulations have been carried out by Knorr,[1] using the Fourier-Fourier method (see Section 2.2.2), by Armstrong,[3] using the Fourier-Hermite method (see Section 2.2.2), and by Dawson and Shanny,[58] using the particle simulation model. Knorr observed a decrease in the damping rate for large amplitude waves at times such that $\omega_B t \sim 1$. Armstrong considered the same problem and found in addition to Knorr's results that large amplitude waves grow again after damping initially. He also found that the initial damping of a large amplitude wave is stronger than is predicted by the Landau theory. A similar observation of the enhanced initial damping was made by Dawson and Shanny. It is not certain, however, to what extent the large fluctuations inherent in particle simulation models influenced the behavior of the wave: in their computation, the field energy of the wave is of a comparable order of magnitude to that of the total fluctuation energy.

One of our purposes has been to use the hybrid model described in Section 3 to investigate the nonlinear behavior of longitudinal monochromatic plasma waves more comprehensively than has been possible previously. The hybrid approach is very well suited to this study

because it does not generate troublesome fluctuation, and is free from numerical instabilities of the type encountered in the Vlasov approach (see Section 2.2). In Section 4.2, we shall consider amplitude oscillation and Landau damping.

Another of our aims has been to investigate the nonlinear frequency shift of electron plasma waves. In a plasma of infinite extent, or of finite length with periodic boundary conditions, the frequency of a wave of large amplitude deviates from that of a small amplitude wave due to nonlinear effects. In an experimental plasma, in which a wave is excited at a fixed frequency, the shift should occur in wavelength instead of frequency.

The frequency shift has been studied analytically by Manheimer and Flynn,[59] Morales and O'Neil,[60] Dewar,[61] and Lee and Pocobelli,[62] and found to be proportional to $E_0^{1/2}$. So far, there has been no report of laboratory observations of nonlinear wavelength shift for comparison with these theories. In Section 4.3, we shall test the theoretical predictions of nonlinear frequency shift against computer simulations carried out by use of the hybrid model.

4.2 Amplitude Oscillation and Landau Damping

4.2.1 Computations

We have performed a series of computer simulations to demonstrate the nonlinear behavior of monochromatic electron plasma waves in a collisionless plasma. The electrostatic energy of the waves in these simulations was of the order of 10^{-4} times the thermal energy. This is about two orders of magnitude smaller than in the simulations of

Dawson and Shanny.[58] Some of the simulations by Knorr,[1] and Armstrong,[3] are in our range of energy. The computations have not, however, been carried out for long enough times to demonstrate amplitude oscillation.

In Fig. 4.1, we demonstrate the amplitude oscillation phenomenon for a large amplitude wave predicted by O'Neil.[48] In this simulation, 8192 particles were followed in a system 64 λ_D long, divided into 64 cells. The continuous Maxwellian velocity distribution was replaced by 128 beams $v_t/14$ apart. Velocity-space was covered from $-4.25\ v_t$ - $4.82\ v_t$ by a grid with mesh size equal to the beam spacing. Periodic smoothing was carried out after every 16 time-steps, a time-step being $0.25/\omega_p$. Mode 3 was excited initially according to Eq. (3.23), and the evolution of the amplitude was followed in time, with periodic boundary conditions applied in space. It is clear from Fig. 4.1 that the amplitude oscillates, as predicted.

The initial amplitude of the wave was $eE_0/m_e v_t \omega_p \simeq 3.4 \times 10^{-2}$, corresponding to a bounce frequency of $\omega_B/\omega_p \simeq 0.09$. The measured initial damping rate is $\gamma_L/\omega_p \simeq 0.0119$. These combine to give $\gamma_L/\omega_B \simeq 0.13$. The measured frequency is $\omega/\omega_p \simeq 1.15$. The corresponding wave phase velocity is $v_p/v_t \simeq 3.91$, so that $\omega/\omega_B \simeq 13$ and $(v_p/v_t)^2 \simeq 15$ are of the same order.

Figure 4.2 shows the temporal behavior of the distribution function, in the vicinity of the wave phase velocity, averaged over space. The changes in the distribution are relatively small; for example, at $\omega_p t = 48$, the ratio of the peak value to the maximum value of the (nearly) Maxwellian distribution is of the order of 10^{-3}. A bump is formed in the distribution for $\omega_p t \simeq 48$, and reappears for $\omega_p t \simeq 144$ and 240.

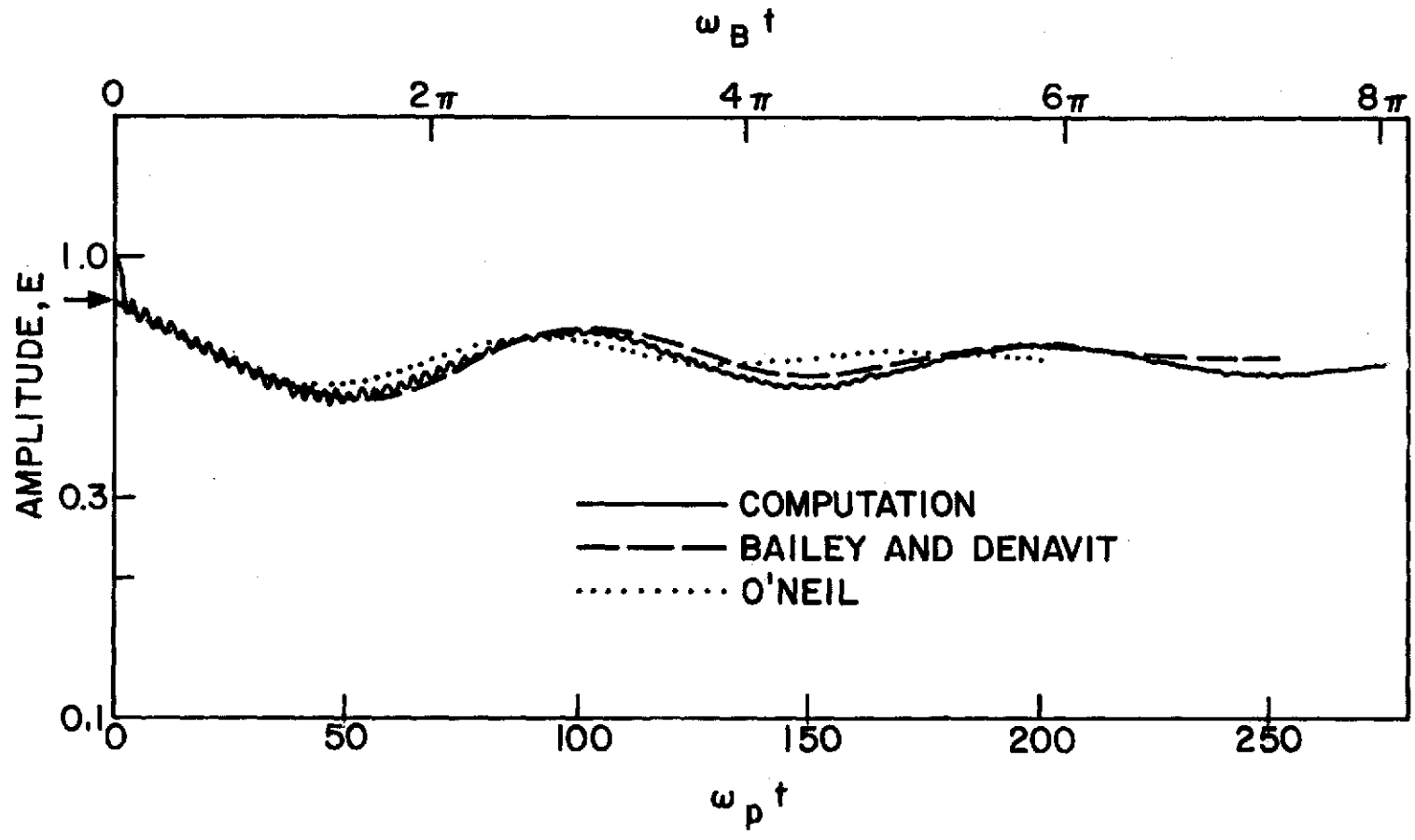

FIG. 4.1. Amplitude oscillation of a large amplitude monochromatic wave. [$H = \Delta x = \lambda_D$, $\omega_p \Delta t = 0.25$] .

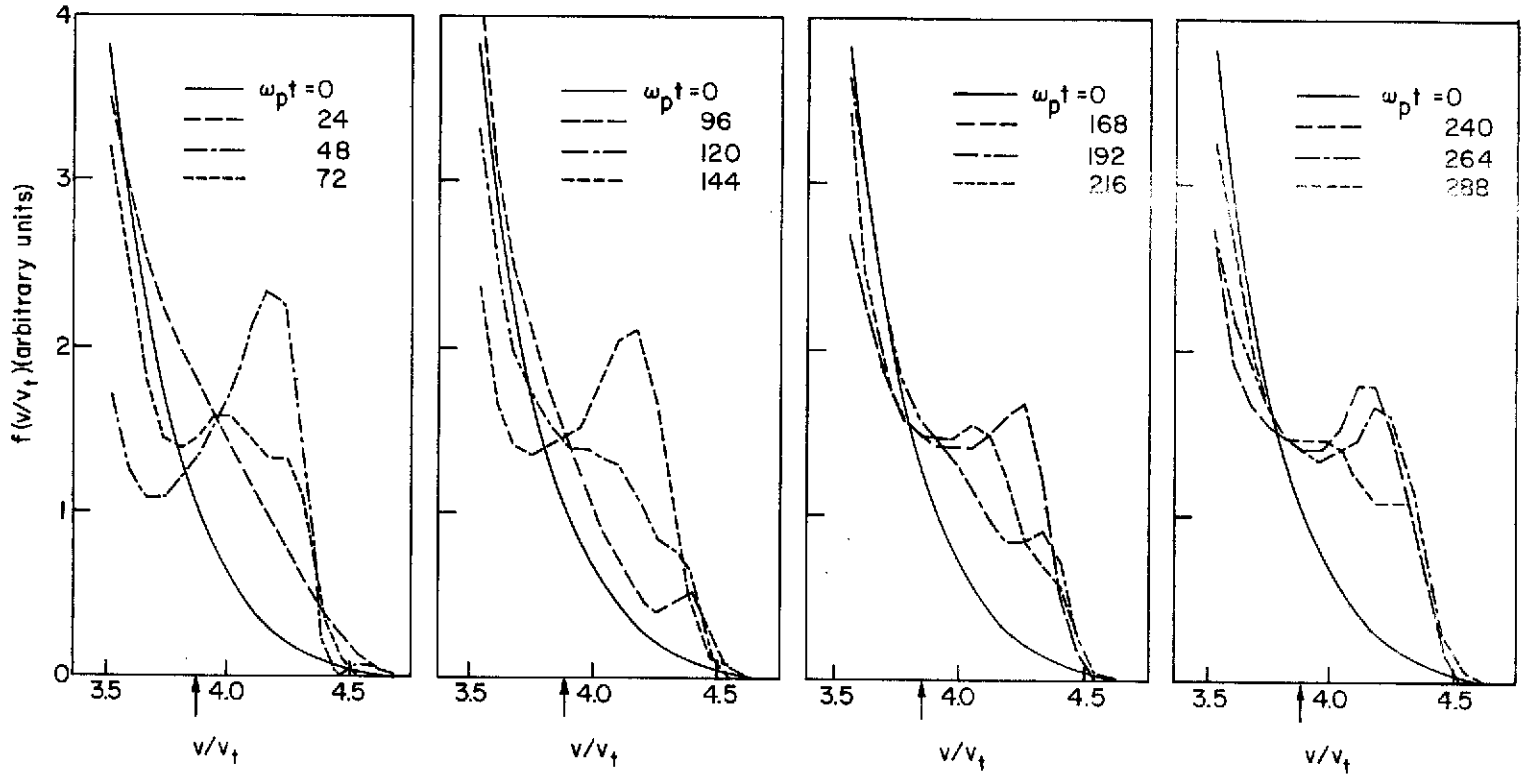

FIG. 4.2. Temporal behavior of the spatially averaged distribution function in the simulation shown in Fig. 4.1. The phase velocity of the wave is marked by an arrow.

Comparison with Fig. 4.1 indicates that these times correspond approximately to minima in the amplitude. The height of the bump becomes progressively smaller on its reappearances, because of phase-mixing of the trapped particles.[48] A similar bump was observed by Armstrong, and considered to cause growth of waves with phase velocities lying in that region of the bump that has positive slope.[3]

The bump on the tail of the distribution function has spatial structure. This is shown in Fig. 4.3, and may be contrasted with the initially spatially homogeneous distribution whose evolution is considered in the quasilinear theory of a warm beam-plasma system.[63,64] The figure shows that the particles rotate by a half-cycle in phase-space from $\omega_p t = 48$ to 96, and another half-cycle from $\omega_p t = 96$ to 144. The cycle is repeated for $\omega_p t = 144$ to 240. It is clear that the phase-space structure becomes progressively less distinct as time increases.

In Fig. 4.4, we present the results of a series of simulations for various values of the initial electric field, E_0, expressed in terms of the convenient parameter γ_L/ω_B, where we recall that $\omega_B = (ekE_0/m_e)^{1/2}$. Only one mode was excited at $t = 0$ for each simulation run, and a different mode and amplitude were used in each run. The amplitude was normalized to unity at $t = 0$ in the plots. It will be seen from Fig. 4.4 that amplitude oscillation occurs for small values of γ_L/ω_B, and that the oscillation becomes less pronounced, with Landau damping extended for a longer period, as γ_L/ω_B increases. The fluctuations in the curves for large values of γ_L/ω_B are due to the round-off errors made in representing numbers by a finite number of digits in

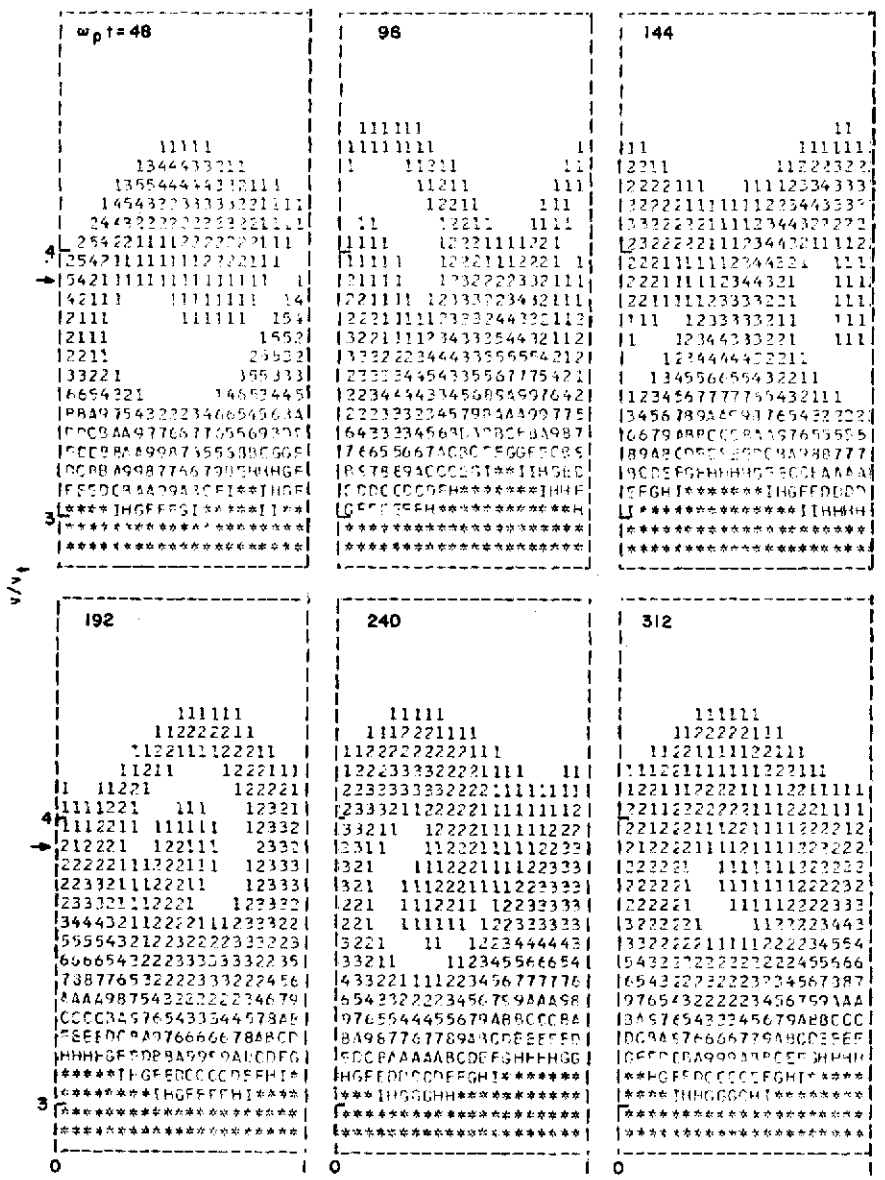

FIG. 4.3. Phase-space plot at six different times, in the simulation shown in Fig. 4.1. The phase velocity of the wave is marked by an arrow. The numbers represent the value of the distribution function.

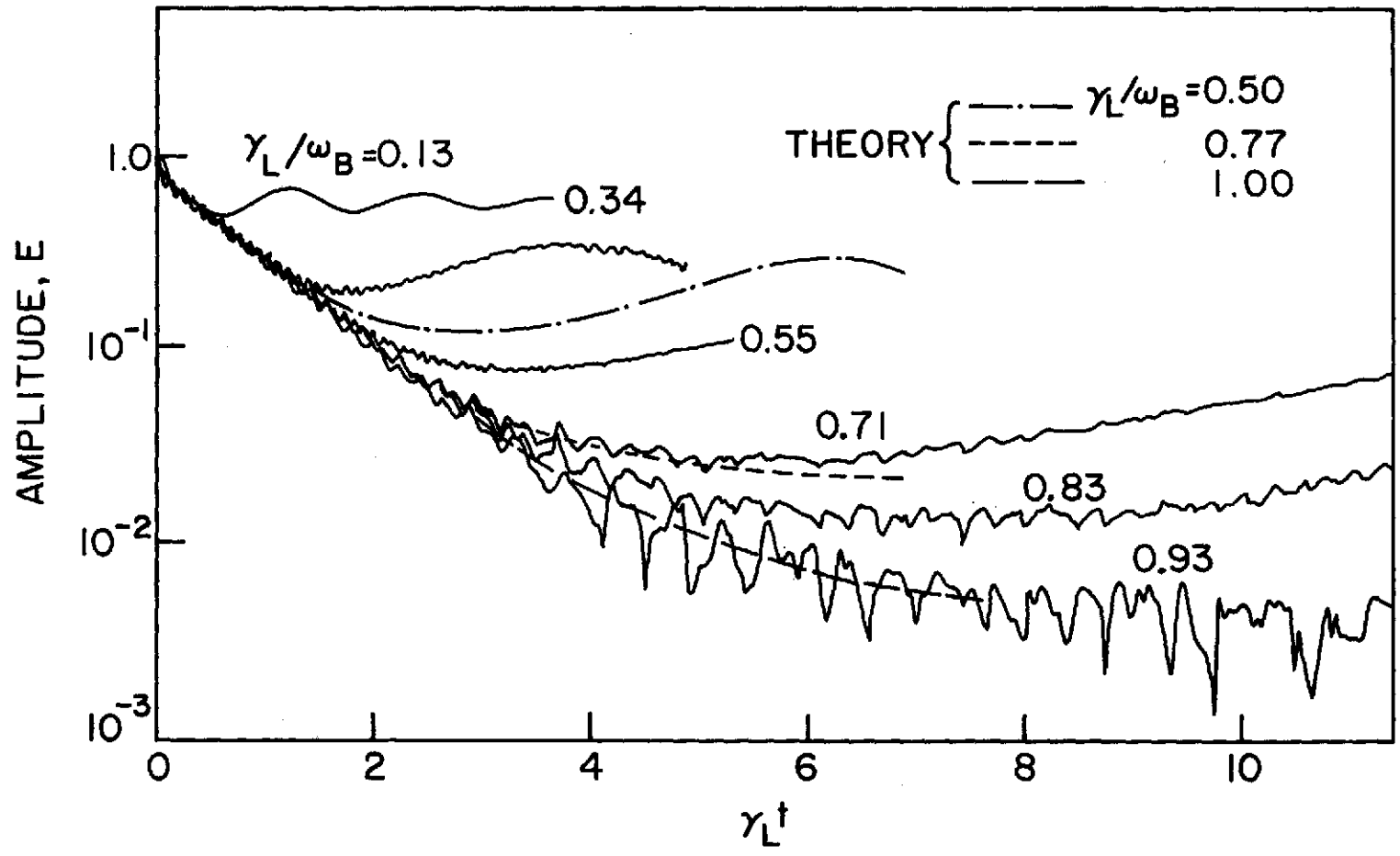

FIG. 4.4. Temporal evolution of amplitude for various initial amplitudes, i.e. γ_L/ω_B, listed in Table 4.1.

the computer. The mode numbers and other parameters used in this series of simulations are tabulated in Table 4.1.

TABLE 4.1. Parameters in the series of simulations presented in Fig. 4.4.

	Mode n	L/λ_D	ω_B/ω_p	γ_L/ω_B	$(\omega/\omega_B)/(v_p/v_t)^2$
a	6	128	0.092	0.13	0.9
b	7	128	0.097	0.34	1.0
c	7	128	0.061	0.55	1.5
d	2	32	0.093	0.71	1.3
e	2	32	0.079	0.83	1.4
f	1	15	0.092	0.93	1.4

4.2.2 Comparison with Theory

There are a number of theories available with which we can make comparisons: the linear theory of Langdon,[31] the amplitude oscillation theory of O'Neil,[48] and Bailey and Denavit,[50] and the nonlinear theory of Sugihara and Kamimura.[52]

Langdon: The theoretical values of the damping rate, γ_L, and frequency, ω_L, are calculated from Eq. (2.66), which includes finite-size particle and spatial grid effects. Retaining only the $\ell = 0$ term in the summation, we obtain $\gamma_L/\omega_p = 0.0118$, and $\omega_L/\omega_p = 1.145$ for Mode 3 plotted in Fig. 4.1. We see very good agreement with the measurements described in Section 4.2.1. The theoretical predictions for each mode presented in Fig. 4.4 have also been found to agree with the measured initial damping and frequency with errors of less than 1%.

O'Neil: We may compare the theoretical predictions of O'Neil with the simulation results shown in Fig. 4.1. By solving the Vlasov equation for a large amplitude wave, O'Neil obtained the time-dependent damping rate,[48]

$$\gamma(t) = \gamma_L \sum_{n=0}^{\infty} \frac{64}{\pi} \int_0^1 d\kappa \left\{ \frac{2n_\pi{}^2 \sin\left[\frac{n_\pi t}{\kappa F(\kappa)\tau}\right]}{\kappa^5 F(\kappa)^2 (1+Q^{2n})(1+Q^{-2n})} \right.$$

$$\left. + \frac{(2n+1)\pi^2 \kappa \sin\left[\frac{(2n+1)\pi t}{2F(\kappa)\tau}\right]}{F(\kappa)^2 (1+Q^{2n+1})(1+Q^{-2n-1})} \right\} , \qquad (4.1)$$

where $F(\kappa)$ $[=F(\kappa,\pi/2)]$ is the complete elliptic integral of the first kind, $Q = \exp\left\{-\pi F[(1-\kappa^2)^{1/2}]/F(\kappa)\right\}$, and $\tau = 1/\omega_B$. It can be shown that $\gamma(t)$, given by Eq. (4.1), reduces to the Landau damping rate in the limit $t/\tau \ll 1$. In the time-asymptotic limit, $\gamma(t)$ vanishes due to phase-mixing, and a Bernstein-Green-Kruskal (BGK) mode[65] is formed. In contrast, the solution of Al'tshul and Karpman, obtained by using the quasilinear approximation, does not demonstrate the phase-mixing but predicts that the amplitude continues to oscillate.[49] O'Neil has indicated, however, that it is not certain whether their solution is correct to order $\gamma_L \tau$.[48]

We have computed Eq. (4.1), including terms up to $n = 3$. We have substituted the numerical value $\gamma_L/\omega_p = 0.0119$ obtained from our computer simulation (Fig. 4.1). For the bounce frequency, we have used $\omega_B/\omega_p = 0.09$, calculated from the initial amplitude in the same simulation (Fig. 4.1). The amplitude variation thus obtained is plotted

in Fig. 4.1. After damping initially, the wave starts to grow somewhat earlier than it does in the simulation. This can be ascribed to the change in wave amplitude, which was not taken into account by O'Neil.

Bailey and Denavit: These authors incorporated the effects of slowly-varying wave amplitude to lowest order in $\dot{\alpha}/\alpha^2$, where $\alpha(t) = [ekE(t)/m_e]^{1/2}$, $\omega_B = \alpha(0)$, and $\dot{\alpha} = d\alpha/dt$, and obtained the following set of equations describing the time evolution of the amplitude,[50]

$$\frac{d\alpha}{dt} = \frac{1}{1-\gamma_L\omega_B/\pi}\left\{64\pi\gamma_L\omega_B\left(\frac{1}{2}\,I_R^T + I_R^{uT}\right) - \frac{\gamma_L^2}{2\pi\alpha\omega_B} \times\left[\cos 2\omega_B t - 2\omega_B t\left(\frac{\pi}{2} - \mathrm{Si}(2\omega_B t)\right)\right]\right\}, \tag{4.2}$$

$$\mathrm{Si}(u) = \int_0^u \frac{\sin\theta}{\theta}\,d\theta,$$

where the quantities I_R^T and I_R^{uT} are given by

$$I_R^T = \sum_{n=1}^{\infty}\int_0^1 \frac{\kappa(2n-1)(QQ_0)^{n-1/2}}{F(\kappa)F(\kappa_0)(1+Q^{2n-1})(1+Q_0^{2n-1})}\sin\left[\frac{(2n-1)\pi}{2}\int_0^t\frac{\alpha(t')dt'}{F[\kappa(t')]}\right]d\kappa, \tag{4.3}$$

$$I_R^{uT} = \sum_{n=1}^{\infty}\int_0^1 \frac{n(QQ_0)^n}{\kappa_0\kappa^4F(\kappa)F(\kappa_0)(1+Q^{2n})(1+Q_0^{2n})}\sin\left[n\pi\int_0^t\frac{\alpha(t')dt'}{\kappa(t')F[\kappa(t')]}\right]d\kappa. \tag{4.4}$$

The values of κ_0 and $\kappa(t')$ for given values of κ and t in Eq. (4.3) are obtained from

$$\alpha[E(\kappa) - (1-\kappa^2)F(\kappa)] = \text{const} , \tag{4.5}$$

while those in Eq. (4.4) are obtained from

$$\frac{\alpha E(\kappa)}{\kappa} = \text{const} , \tag{4.6}$$

where $E(\kappa)[= E(\kappa,\pi/2)]$ is the complete elliptic integral of the second kind. We have solved Eqs. (4.2)-(4.6) numerically, for the same values of γ_L and ω_B used above, and with the results plotted in Fig. 4.1. There is very good agreement between the theory and the simulation. We note, however, that there is a slight difference in amplitude, and that the phase-mixing is somewhat slower in the simulation results than the theory predicts. These differences are probably due, first, to the fact that the condition, $\omega/\omega_B \gg (v_p/v_t)^2$, is not satisfied in the simulation, and second, that the theory of Bailey and Denavit is not self-consistent.

Sugihara and Kamimura: These authors derived from the Vlasov equation a set of integro-differential equations which describe the behavior of the amplitude of a monochromatic wave. Numerical solutions of these integro-differential equations demonstrated amplitude oscillation for $\gamma_L/\omega_B \ll 1$, and Landau damping for $\gamma_L/\omega_B \gg 1$.

We may make a comparison between our simulation results and the theoretical results of Sugihara and Kamimura. First, the behavior of the distribution function obtained in the simulation (Fig. 4.3) may be compared qualitatively with that from the theory. Sugihara and Kamimura

presented phase-space plots for $\gamma_L/\omega_B = 0.1$ at three different times, corresponding to the first point of minimum amplitude, the first maximum, and to a point where the amplitude nearly ceases to oscillate (see Figs. 5-7 of Ref. 52). In our simulation, these times correspond to $\omega_p t \simeq 48$, 96, and 240. We find that their results and ours are consistent in the amount of rotation in phase-space, and the distinctive pattern. However, in our simulation, the wave amplitude still shows oscillatory behavior for $\omega_p t \sim 240$, in contrast to the solution of Sugihara and Kamimura. For $\omega_p t > 240$, our results show continuing particle rotation in phase-space, and a tendency to develop a circular plateau (see Fig. 4.3, $\omega_p t = 312$). This is consistent with the O'Neil solution in the time-asymptotic limit, i.e., formation of a BGK mode.

Next, we may compare the simulation results given in Fig. 4.4 with those of Sugihara and Kamimura. Some of their results are reproduced in that figure. First, we note that their calculation shows that, for $\gamma_L/\omega_B = 0.1$, the amplitude approaches a constant value after nearly two periods of oscillation, although the distribution function still retains nonuniform features. In our simulation, however, the amplitude oscillation lasts more than two periods, and does not seem to die out so quickly. This fact seems to be in at least qualitative agreement with a nonlinear spatial Landau damping experiment by Malmberg and Wharton[54] in which there was no clear sign of phase-mixing. A similar feature of this persistent amplitude oscillation was also observed in the behavior of an externally excited large amplitude wave in a simulation of sideband instability by Denavit and Kruer.[11] Second, we recall that Sugihara and Kamimura found that there is a critical value of

$\gamma_L/\omega_B = 0.77$, which separates waves into those with oscillatory behavior ($\gamma_L/\omega_B < 0.77$), and those which are continuously damped ($\gamma_L/\omega_B > 0.77$). Figure 4.4 indicates that there is no such critical value below $\gamma_L/\omega_B = 0.93$. Third, we note that there is a tendency in our simulation results for the amplitude to decrease to a lower level, for a given value of $\gamma_L\omega_B$, than is predicted by the theory of Sugihara and Kamimura; the first maximum is also lower than the theory predicts. Although the simulation results given in Fig. 4.4 are similar to the theoretical results obtained by Sugihara and Kamimura, it is important to note that in our simulations $\omega/\omega_B \gtrsim (v_p/v_t)^2$, whereas they implicitly assumed that $\omega/\omega_B \gg (v_p/v_t)^2$.

4.3 Nonlinear Frequency Shift

4.3.1 Computations

In Fig. 4.5, we show the variation of the nonlinear frequency shift of electron plasma waves as a function of the electric field amplitude. In this simulation, 4096 particles were followed in a system 50 λ_D long, divided into 64 cells. The continuous Maxwellian velocity distribution was replaced by 64 beams spaced $v_t/7$ apart. Velocity-space was covered from -3.79 v_t - 5.21 v_t by a grid with mesh size equal to the beam spacing. Periodic smoothing was carried out every 16 time-steps, a time-step being $0.25/\omega_p$. Periodic boundary conditions were applied in space.

Mode 3 was excited initially according to Eq. (3.23), with amplitude $(eE_0/m_e v_t \omega_p)$ varying from small values (9×10^{-3}), which exhibit Landau damping, to large values (3×10^{-1}) such as were studied in the simulations of Dawson and Shanny.[58] For each simulation with different

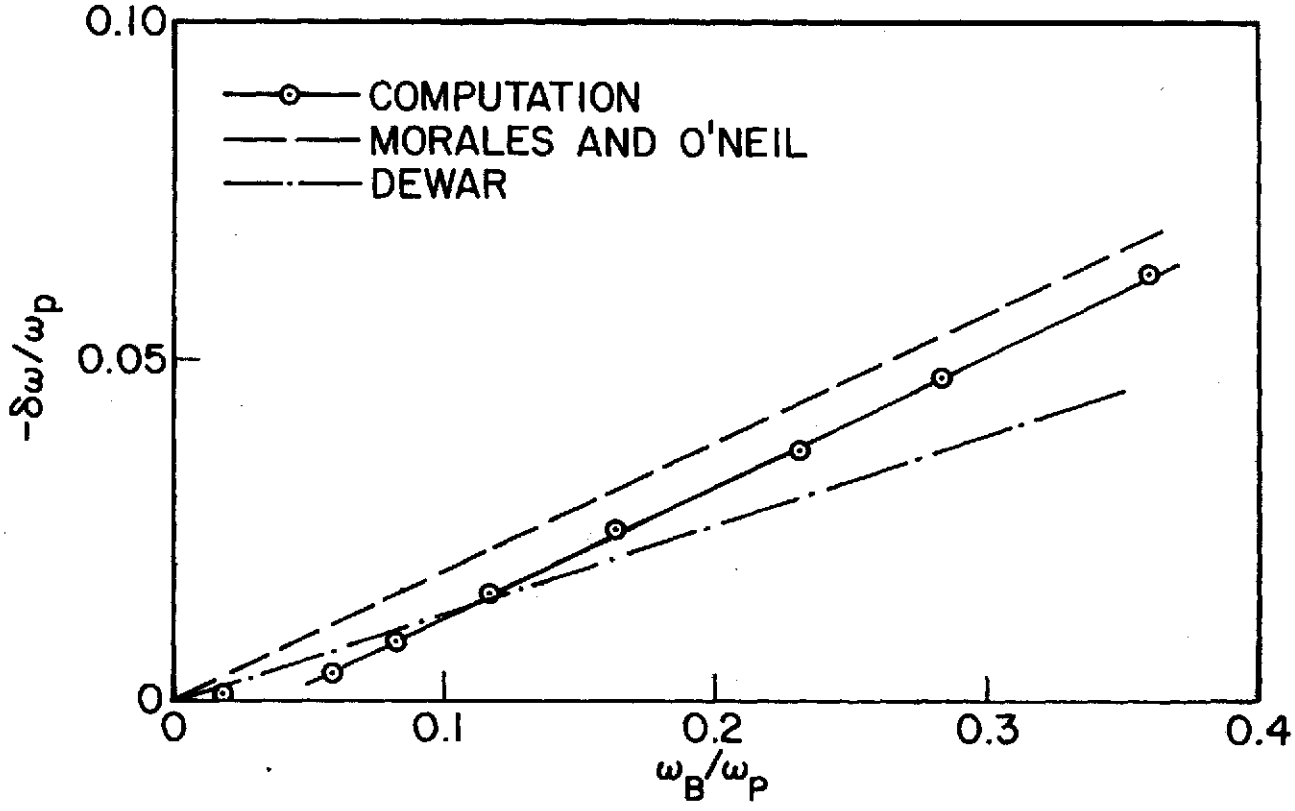

FIG. 4.5. Nonlinear frequency shift of an electron plasma wave. $[H = \Delta x = (50/64)\lambda_D$, $\omega_p \Delta t = 0.25]$.

amplitude, the frequency of Mode 3 was measured by computing the total amount of phase change in the Fourier transform of the electric field between $\omega_p t = 6$ and 60. The frequency shift plotted in Fig. 4.5 was then obtained by subtracting the linear frequency, $\omega_L = 1.247\ \omega_p$, obtained from Eq. (2.66), from the measured frequency. Except for very small amplitudes, the nonlinear frequency shift is proportional to $E_0^{1/2}$, and given by

$$\frac{\delta\omega}{\omega_p} = 0.006 - 0.2\ \frac{\omega_B}{\omega_p} \ . \qquad (4.7)$$

To check the dependence of this result on the beam spacing, the simulations were repeated with the beam spacing halved, and the same number of smoothing operations. The differences in frequency shift were not more than 3%.

A significant fact to note here is the high degree of accuracy with which it was possible to determine the frequency, and frequency shift. The model based on the hybrid approach is, therefore, much more efficient than a particle code in terms of computing cost for this measurement.

4.3.2 Comparison with Theory

Manheimer and Flynn[59] examined the self-consistency of the O'Neil solution for the time-asymptotic state[48]: they studied whether the potential created by the O'Neil solution satisfies the Poisson equation. They found that it is approximately self-consistent if a frequency shift given by

$$\delta\omega = -\beta\left(\frac{eE_0}{m_e k}\right)^{1/2}\left(\frac{\omega_p^2}{k^2}\right)\left(\frac{\partial^2 f_0}{\partial v^2}\right)_{v=v_p}\left(\frac{\partial\epsilon_p}{\partial\omega}\right)^{-1}_{\omega=\omega_L}, \qquad (4.8)$$

is included, where β is a numerical factor equal to $2^{1/2}$, f_0 is the initial distribution function, and ϵ_p is the linear plasma permittivity. In deriving Eq. (4.8), Manheimer and Flynn only considered the trapped particles with simple harmonic motions, i.e., those near the potential wells of the wave, and the untrapped particles with straight line orbits. Morales and O'Neill solved an initial value problem to find the time-dependent shift in the complex frequency of the wave.[60] They took into account the exact trajectories for both the trapped and untrapped particles, and obtained a frequency shift which varies in an oscillatory manner and approaches a constant value in the time-asymptotic limit. Their time-asymptotic frequency shift is expressed in the same form as Eq. (4.8) except that β is given by

$$\beta = \frac{16}{\pi}\int_0^1 d\kappa\left\{\frac{\kappa[2E(\kappa) - F(\kappa)]^2}{F(\kappa)} + \frac{[2(E(\kappa)-F(\kappa))+\kappa^2 F(\kappa)]^2}{\kappa^6 F(\kappa)}\right\} \simeq 1.63 . \qquad (4.9)$$

This result is more accurate than that of Manheimer and Flynn, who treated particle trajectories in the approximation mentioned above.

Lee and Pocobelli predicted frequency shifts for waves with $v_p/v_t \gtrsim 4$ up to about 50% larger than those predicted by Morales and O'Neil. These were obtained by including effects of electrons not in the vicinity of the phase velocity of the wave.[62] In contrast to these theories treating the case in which the wave is switched on suddenly at $t = 0$, Dewar considered the case of an adiabatically excited wave,

i.e., the wave was turned on gradually.[61] He obtained a time-asymptotic frequency shift similar to that expressed by Eq. (4.8), but with $\beta = 1.09$.

Substituting $\omega_L/\omega_p = 1,247$ for Mode 3, obtained from Eq. (2.66), and the Maxwellian distribution for f_0 in Eq. (4.8), we have

$$\delta\omega \simeq \begin{cases} -0.19\omega_B & \text{(Morales and O'Neil)}, \\ -0.13\omega_B & \text{(Dewar)}, \end{cases} \tag{4.10}$$

which are plotted in Fig. 4.5. We see that the slopes of the lines from the simulation, and from the theory of Morales and O'Neil, are very similar. This is to be expected because our simulation of an initial value problem resembles the Morales and O'Neil problem, rather than the Dewar problem. It should be remembered, however, that the theoretical result is the time-asymptotic value, whereas the measured frequency shift is an average over the period $\omega_p t = 6$ to 60. It should also be recalled that the value of ω_B corresponds to the initial amplitude of the wave. Since the theoretical result due to Morales and O'Neil was obtained under the condition that the amplitude variation is very small, it does not matter much whether the bounce frequency is computed from the initial amplitude or from the time-asymptotic amplitude. In our simulation, however, the amplitude variation is not negligible; if the bounce frequency were computed from the time-asymptotic amplitudes, the points in Fig. 4.5 would be moved towards the theoretical line of Morales and O'Neil.

4.4 Summary

The nonlinear behavior of monochromatic plasma waves has been studied over a wide range of wave amplitudes, by use of the low-noise model based on the hybrid approach.

In the study of amplitude oscillation and Landau damping in Section 4.2, we have attempted investigation in areas where analytical approaches are not easily tractable, i.e., in cases where the condition, $\omega/\omega_B \gg (v_p/v_t)^2$, is not satisfied. The results of our simulations show good qualitative agreement with the theories of Bailey and Denavit, and Sugihara and Kamimura, who have made the assumption, $\omega/\omega_B \gg (v_p/v_t)^2$. However, there are significant differences between our simulation results and the theoretical results of these authors; first, phase-mixing of the amplitude oscillation is slower than predicted, and second, there exists no critical value of γ_L/ω_B within our parameter range such as was found by Sugihara and Kamimura. These results will be helpful in better understanding the phenomenon, and in developing an analytical theory in cases where $\omega/\omega_B \lesssim (v_p/v_t)^2$.

In the study of nonlinear frequency shift, in Section 4.3, we have measured the frequency shift for finite amplitude waves, and compared the results with theoretical predictions. It has been demonstrated that the simulation results agree well with the theoretical predictions of Morales and O'Neil.

5. SIDEBAND INSTABILITY

5.1 Introduction

In 1968, Wharton et al. reported results of experiments on large amplitude, longitudinal electron plasma waves, in which not only was spatial amplitude oscillation of the type discussed in Section 4 observed, but also spatial growth of sidebands separated from the frequency of the large amplitude wave by the bounce frequency of trapped electrons, ω_B.[66] These experiments have stimulated a number of theoretical studies that may be classified into two types of approaches. One is based on a wave-wave interaction mechanism between the large amplitude wave and sideband waves (Kruer et al.;[57] Goldman;[67] Goldman and Berk;[68] Wong;[69] and Mima and Nishikawa[70,71]). The other is a quasi-linear approach based on wave-particle interaction (Shapiro and Shevchenko;[72] Bud'ko et al.;[73] Manheimer;[74] Yagishita and Ichikawa;[75] and Brinca[76]).

Other laboratory experiments on sideband instability have been carried out by Franklin et al.,[77] and Jahns and Van Hoven[78] for electron plasma waves, and by Ikezi et al.[79] for ion waves. These experimental results have verified some of the predictions of wave-wave interaction theory applied to a spatial case.[77,79] However, there are some observations which suggest the quasilinear mechanism as an alternative cause of the instability.[78]

Computer simulations of the sideband instability have been performed by Kruer and Dawson,[80] Denavit and Kruer,[11] and Rosen et al.[81] Kruer and Dawson studied the instability in a one-dimensional plasma driven by an external electric field of a given frequency by use of a particle

simulation model. They observed the growth of sidebands having a frequency separation consistent with the experimental results of Wharton et al. It was demonstrated later by Rosen et al. that artificial removal of trapped particles eliminates the sideband growth. Denavit and Kruer carried out simulations of a similar problem to make comparison between the particle simulation and the Vlasov approach, and found close agreement between the results of the two approaches. In these simulations, electrostatic energy of the large amplitude wave was 0.1-1.0 times the initial thermal energy of the plasma. The high wave energy is required in the particle code since such simulations are much noisier than real plasmas, as discussed in Section 2.

In laboratory experiments, however, electrostatic energy of the large amplitude wave is typically much smaller (10^{-4} - 10^{-3}) than the thermal energy. Also, in most of the analytical approaches mentioned above, it is assumed that the wave energy is much smaller than the thermal energy. In what follows we shall investigate the sideband instability, using the simulation model based on the hybrid approach, in the parameter range which allows us both to make more quantitative comparisons with existing theories, and to model more satisfactorily the conditions appropriate to laboratory experiments. The quantitatively accurate results obtainable by use of this model should lead to better understanding of the phenomena involved, and refinement of the theory.

5.2 Computations

In the series of simulations to be described in this section, we have considered an initial value problem, and imposed perturbations at time $t = 0$ according to Eq. (3.23). Mode 13 was chosen for the large

amplitude wave, which we will refer to from now on as the 'main' wave. Five simulation runs (A - E) were made with the initial main wave amplitude in the range $0.06 \lesssim eE_0/m_e v_t \omega_p \lesssim 0.5$. In terms of electrostatic energy, this is between 1.8×10^{-3} and 1.2×10^{-1} times the thermal energy. Waves were also excited initially as sidebands of Mode 13 according to Eq. (3.23), but with random phases at the energy level of 10^{-6} times the thermal energy.

In all of the computations, 16384 particles were followed in a system 256 λ_D long, divided into 256 cells. The continuous Maxwellian velocity distribution was replaced by 64 beams spaced $v_t/7$ apart. Velocity-space was covered from $-3.79\ v_t$ - $5.21\ v_t$ by a grid with mesh size equal to the beam spacing. Periodic smoothing was carried out every 16 time-steps, a time-step being $0.25/\omega_p$. Periodic boundary conditions were applied in space.

Results of a typical simulation are given in Fig. 5.1. It shows the evolution of the main wave and two test waves. The initial amplitude of the main wave was $eE_0/m_e v_t \omega_p \simeq 0.12$, corresponding to $\omega_B/\omega_p \simeq 0.19$, where $\omega_B [= (ek_0 E_0/m_e)^{1/2}]$ is the bounce frequency of an electron at the bottom of a potential well of the main wave with wavenumber k_0. Mode 11 decays first, and then begins to grow. Mode 12 shows an evolutionary pattern similar to that of Mode 11 at early times, and then begins to grow more slowly than Mode 11. The temporal behavior of the velocity distribution function at the early times is shown in Fig. 5.2. It is a plot of the spatially averaged distribution function in the vicinity of the phase velocity of the main wave. The

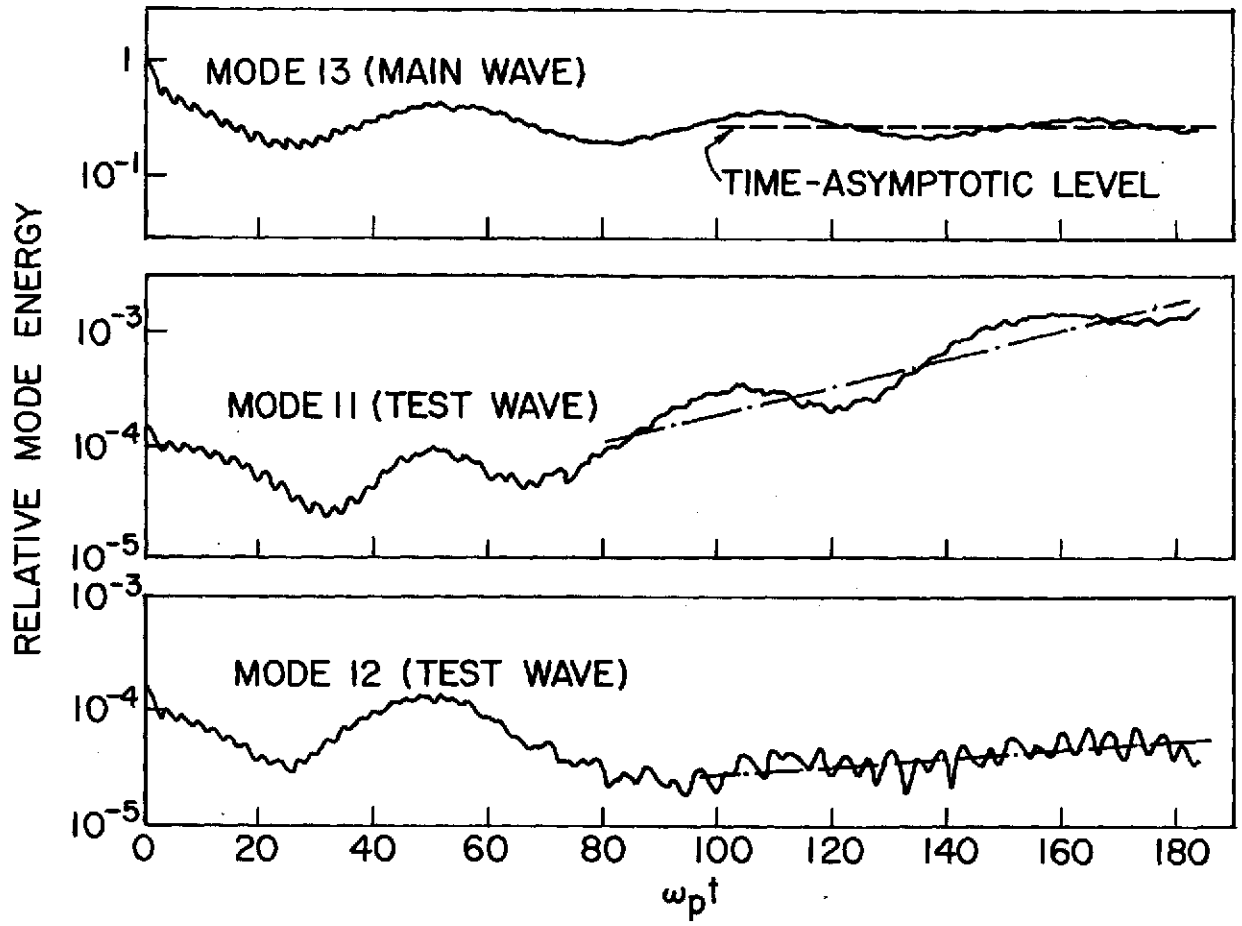

FIG. 5.1. Temporal evolution of sideband instability:
(Initial main wave electrostatic energy/thermal energy) = 7.42×10^{-3} .

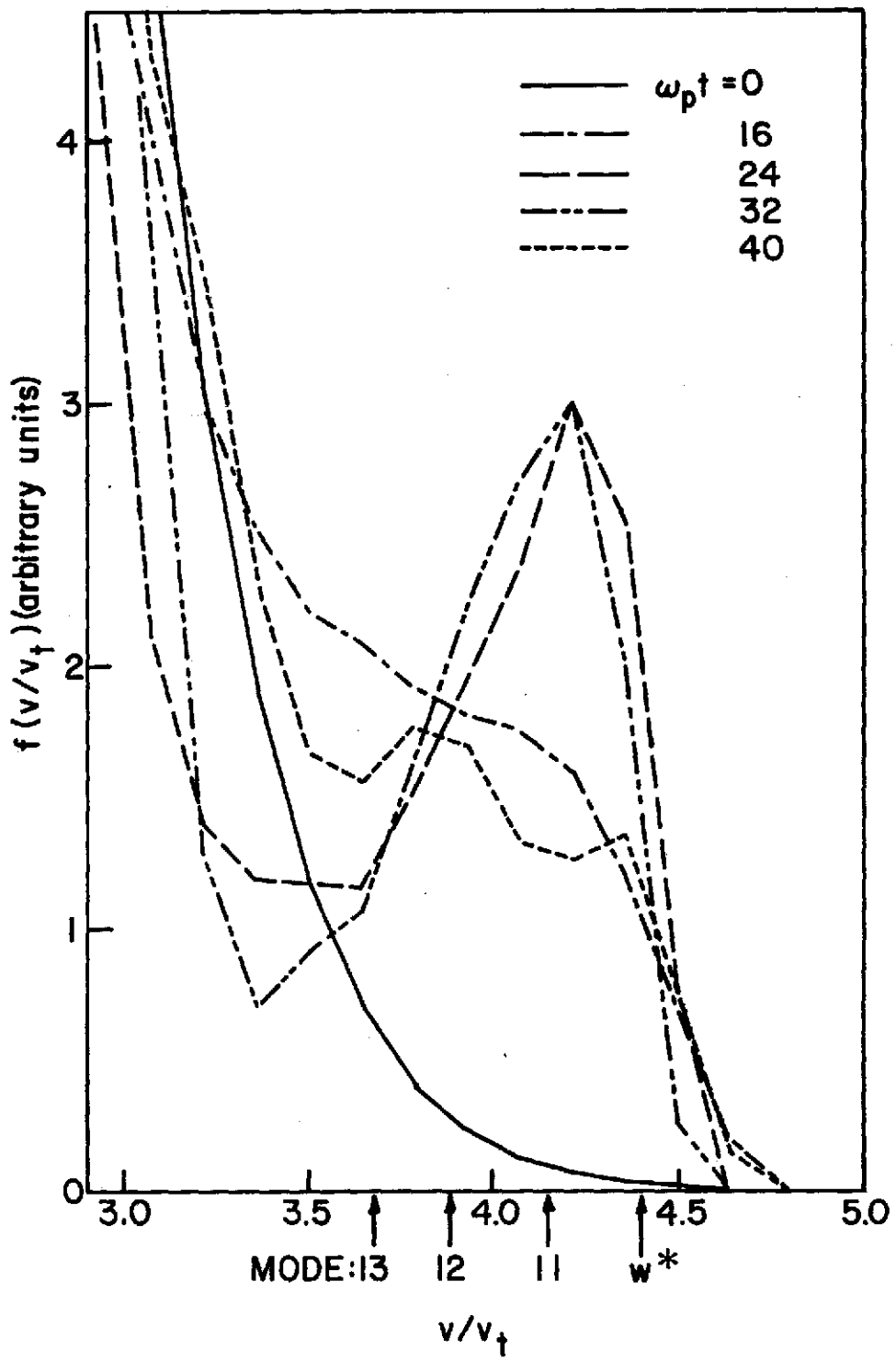

FIG. 5.2. Temporal behavior of the spatially averaged distribution function at short times in the simulation shown in Fig. 5.1. Phase velocities of Modes 11-13 are shown by arrows. w* is the velocity given by Eq. (5.13).

distribution function at later times, when the sidebands are growing steadily, is shown in Fig. 5.3 as a phase-space plot. It is seen clearly that there are particles trapped near the bottom of the wave potential wells. We have confirmed that phase-space structure similar to that shown in Fig. 5.3 persisted throughout the simulation run. This may be compared with Figs. 3 and 8 of Ref. 80, which show only a negligible number of such particles to be present. In their simulation, using a particle code, the number of particles with the velocities in the vicinity of the phase velocity ($\sim 4\ v_t$) of the main wave is very small, because the Maxwellian velocity distribution assumed falls off as $\exp(-v^2/2v_t^2)$. Since it is these particles that will stay trapped near the bottom of the potential wells, a situation such as observed in Ref. 80 may occur.

In Fig. 5.4 are given the results of two simulations with a larger amplitude of the main wave than the previous simulation. The growth of Mode 11, in the lower sideband ($k < k_0$), is shown in Fig. 5.4(a) both for growth from noise, and when it is excited as a test wave at $t = 0$. Figure 5.4(b) shows growth of a test wave in Mode 15, in the upper sideband ($k > k_0$). Though not shown, we also observed growth from noise of Mode 15, and other modes, in the simulation carried out without test waves. The distribution function demonstrated similar behavior to that shown in Figs. 5.2 and 5.3.

An energy spectrum obtained in one of the simulations is shown in Fig. 5.5. It was measured at time $\omega_p t = 175$, when the main wave amplitude reaches nearly the fifth minimum in the temporal evolution. The lower sideband is seen to be larger than the upper sideband. It

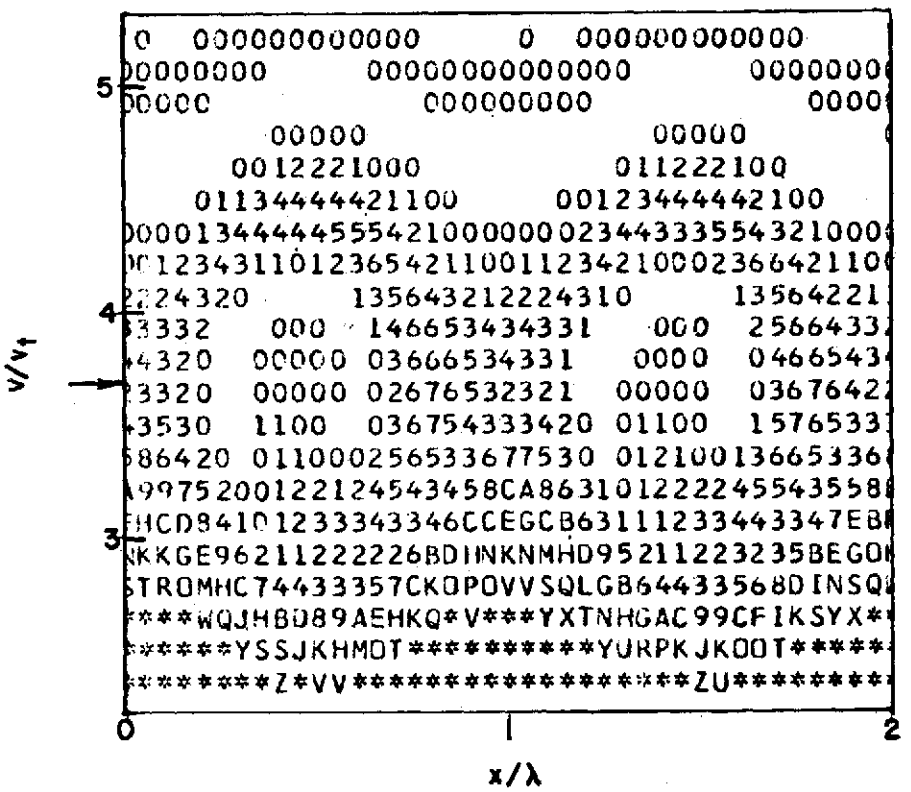

FIG. 5.3. Phase-space plot at $\omega_p t = 96$, in the simulation shown in Fig. 5.1. The phase velocity of the main wave is marked by an arrow.

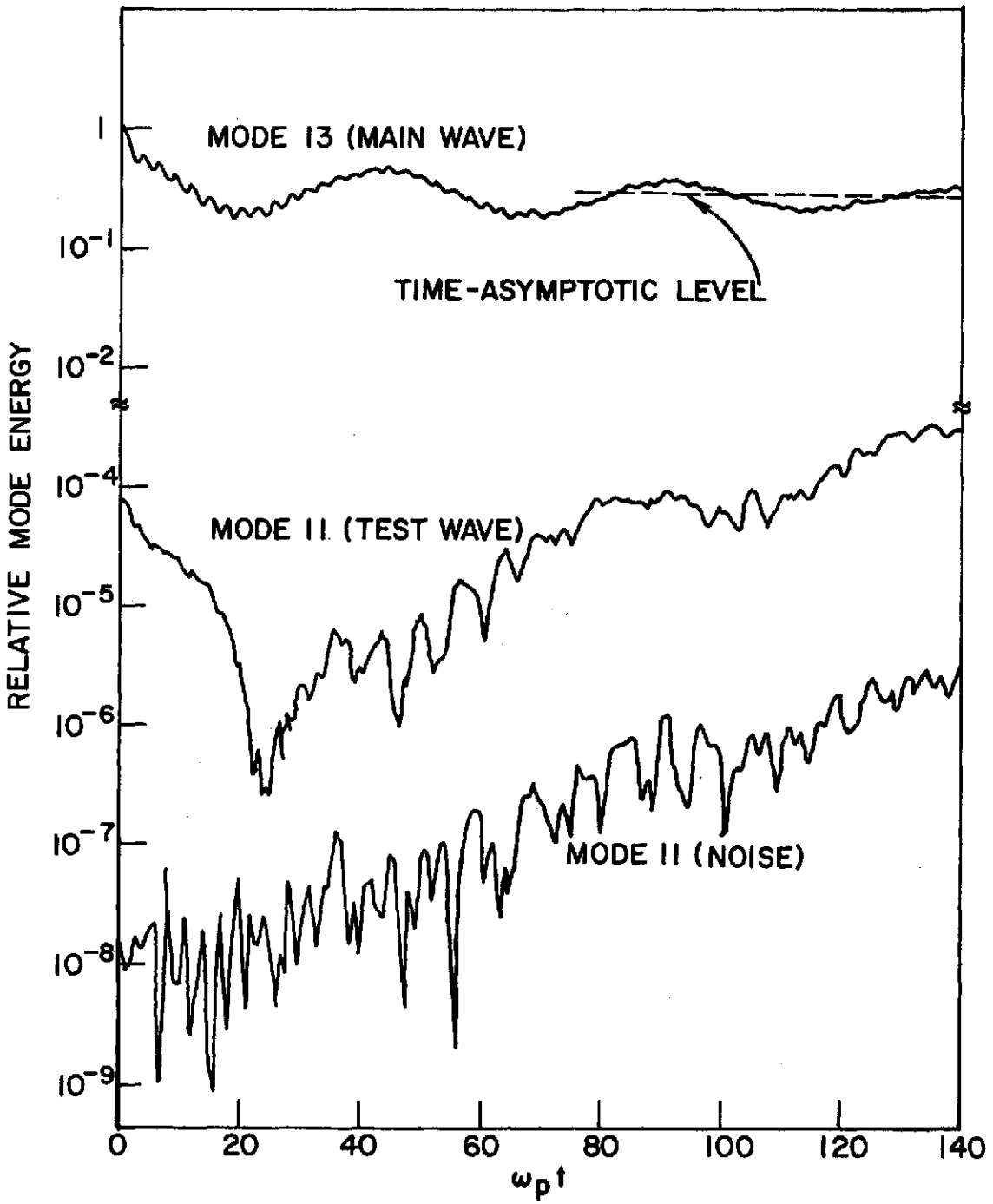

FIG. 5.4(a). Temporal evolution of sideband instability: (Initial main wave electrostatic energy/thermal energy) = 2.97×10^{-2} . Main and lower sideband waves.

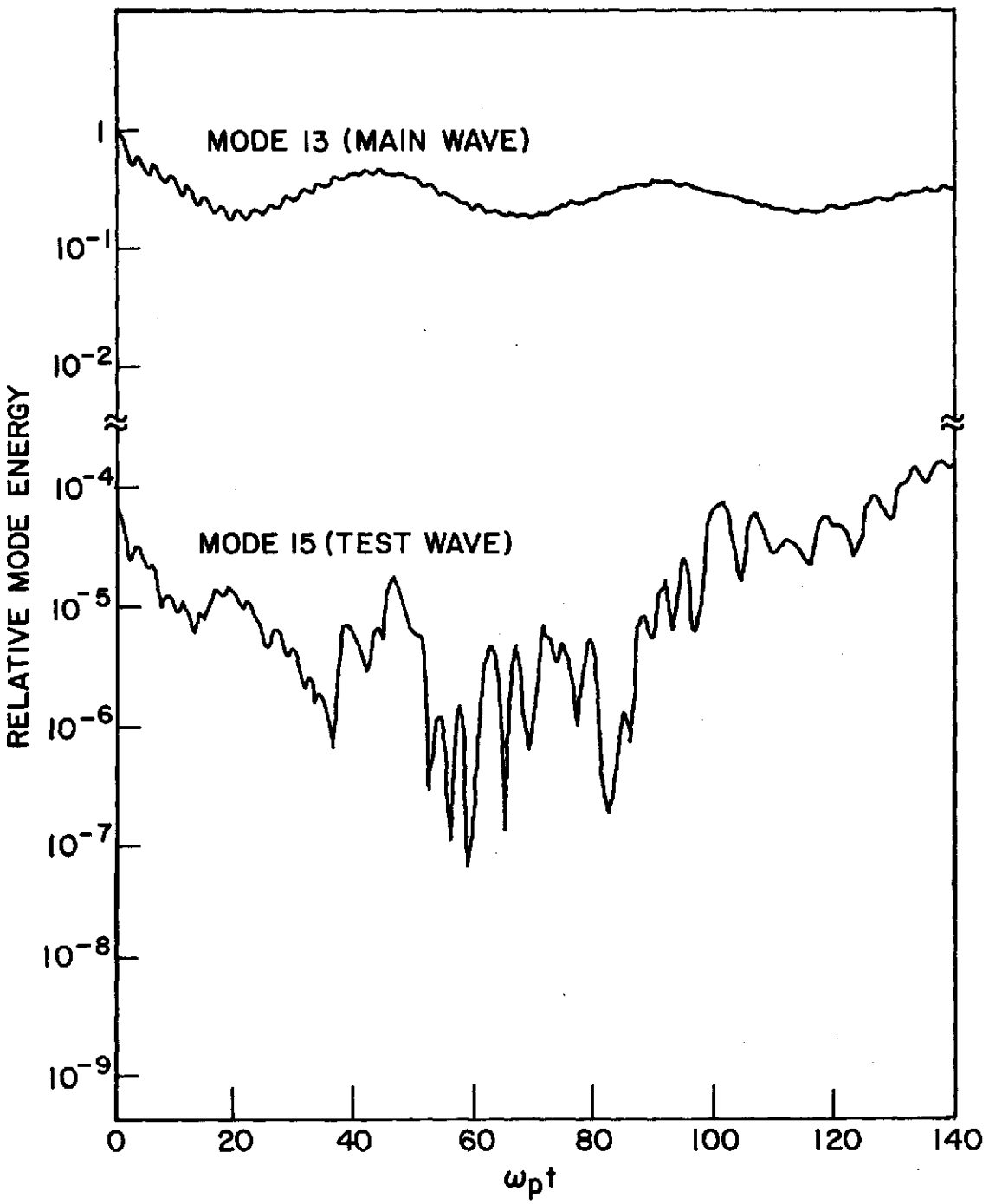

FIG. 5.4(b). Temporal evolution of sideband instability: (Initial main wave electrostatic energy/thermal energy) = 2.97×10^{-2}. Main and upper sideband waves.

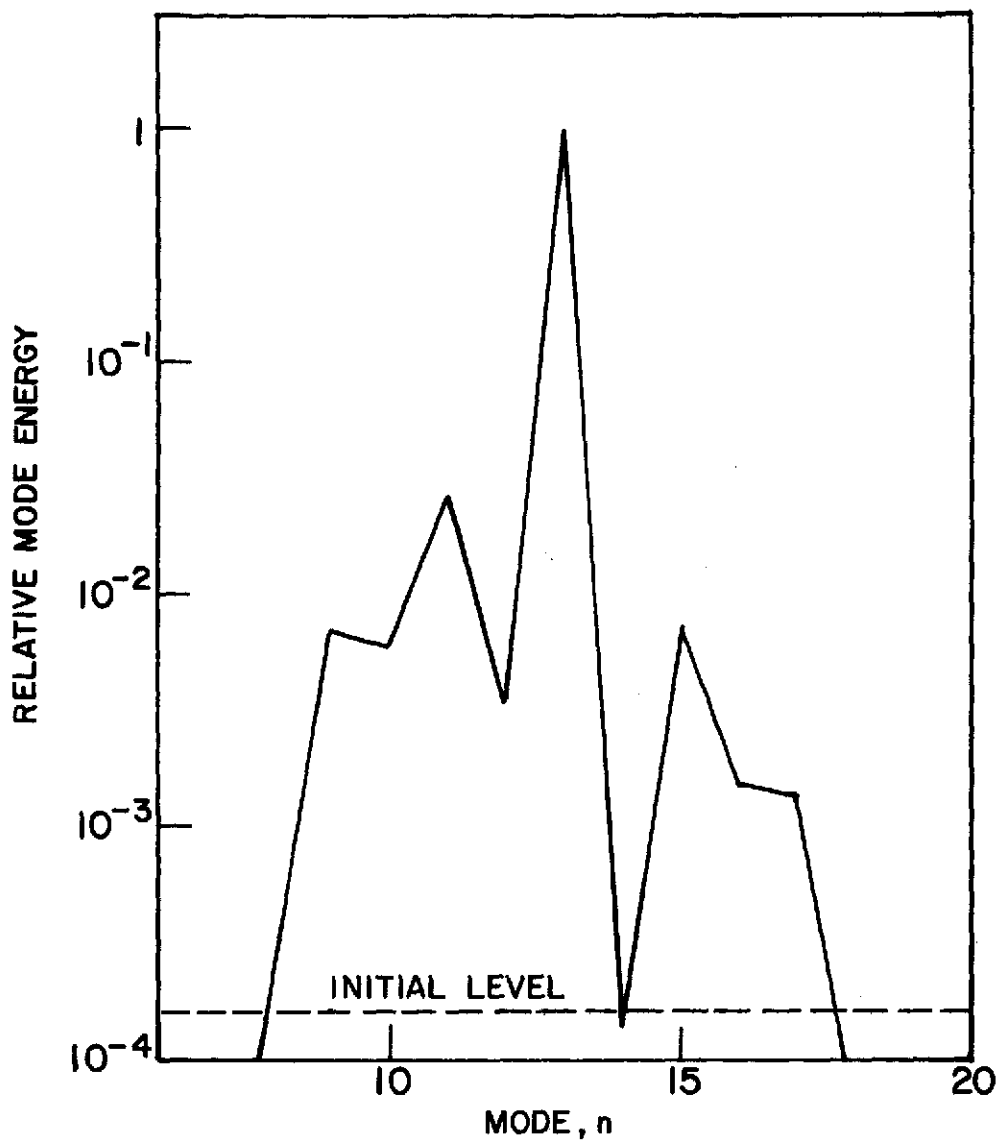

FIG. 5.5. Energy spectrum at $\omega_p t = 175$ due to sideband instability: (Initial main wave electrostatic energy/thermal energy) = 2.97×10^{-2}.

should be remembered, however, that the test waves initially decay and then begin to grow. Consequently, the fastest growing mode (Mode 10) does not necessarily appear as the sideband peak. Some of the modes, for example Mode 14, are still below their initial level at the time when the energy spectrum is measured.

A case with a heavily-damped main wave is presented in Fig. 5.6. In this simulation, Mode 17 was used as the main wave. The test wave shown was the fastest growing mode. We see that the main wave first decays, and then undergoes amplitude oscillation with slow damping. The test wave shows continued growth after it has reached an energy level comparable to, or exceeding, that of the main wave.

From the results shown, we note the following:

(a) The main wave amplitude shows oscillatory behavior, corresponding to that predicted by O'Neil for the temporal case.

(b) Test waves exhibit initial decay which is stronger than the corresponding linear Landau damping, and then show approximately exponential growth.

(c) Both sidebands grow from noise with growth rates corresponding to those of the test waves.

(d) The lower sideband is higher in amplitude than the upper sideband.

(e) There is some modulation superimposed on the growth of the sidebands. This seems to be correlated with the amplitude oscillation of the main wave.

(f) In the case of a heavily-damped main wave, test waves exhibit features similar to (a) through (e).

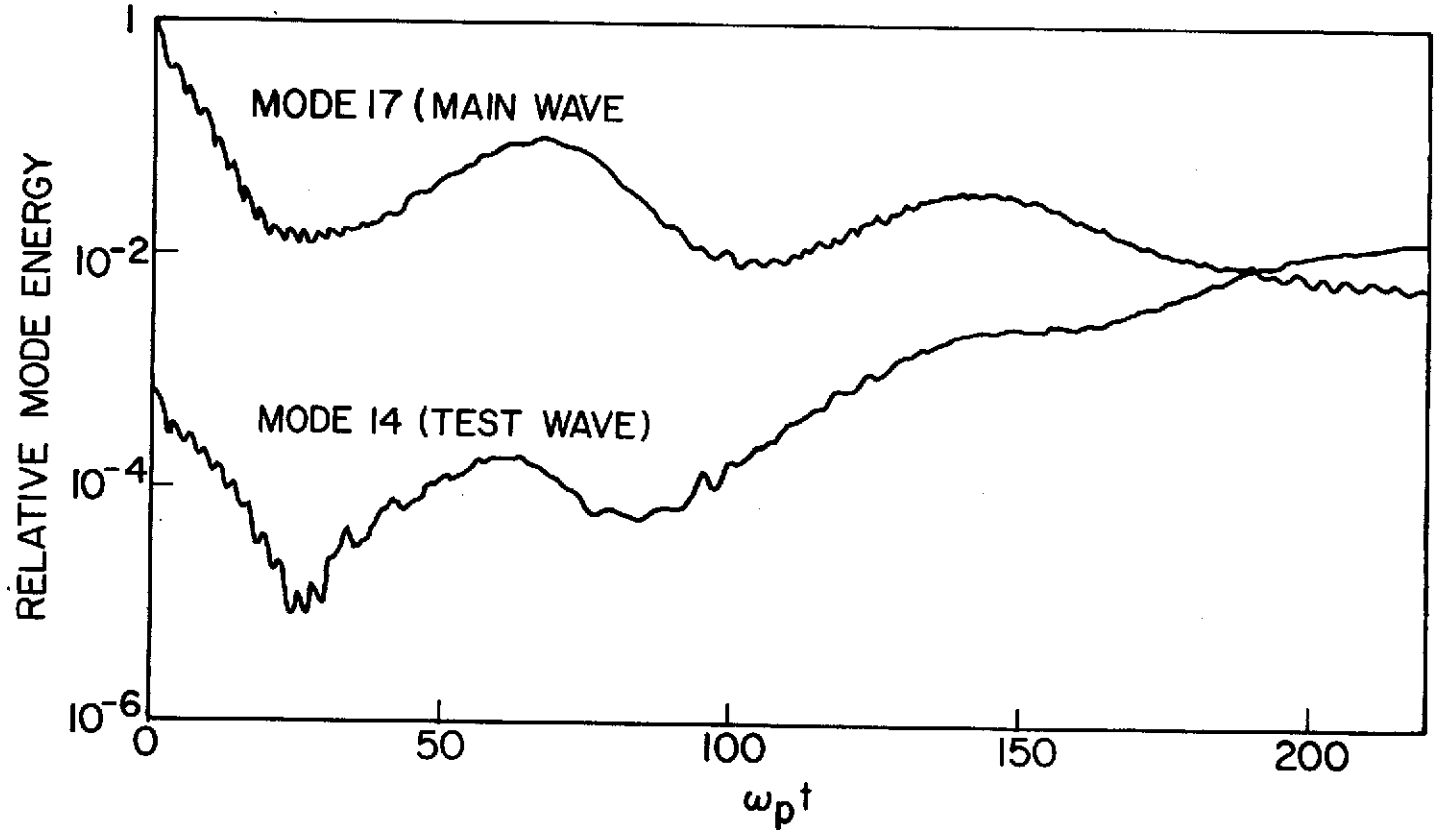

FIG. 5.6. Sideband instability with a heavily-damped main wave: (Initial main wave electrostatic energy/thermal energy) = 7.1×10^{-3}. The damping rate and phase velocity of the main wave are $\gamma_L/\omega_p \simeq 0.085$, and $v_p/v_t \simeq 3.1$ [Eq. (2.66)].

The foregoing features are common to all of our simulations, and suggest that it might be profitable to divide theoretical description into two parts: first, the transient processes occurring at the earliest stages of evolution, and second, the development at later times when the sidebands are growing steadily.

5.3 Comparison with Theory

In order to explain the sideband instability, Kruer et al.[57] considered a simple theoretical model in which the trapped electrons are treated as a bunched beam of harmonic oscillators of frequency ω_B, and obtained a sideband growth rate consistent with the experimental results of Wharton et al.[66] Goldman took a rather different approach.[67] It is known that the time-asymptotic limit of the O'Neil solution[48] is a large amplitude BGK mode.[65] As long ago as 1962, Pfirsch had speculated that a large class of BGK modes might be unstable, although he did not pursue the question.[82] Goldman examined the stability of the BGK modes, and showed that the sideband growth is due to a parametric type of coupling between waves enhanced by the trapped particles. He obtained the results of Kruer et al. as a special case in which trapped electrons are localized at the bottom of the potential wells of a BGK wave. Goldman and Berk obtained a dispersion relation, in the bunched beam approximation, including the contribution of trapped electrons to the frequency shift of the large amplitude wave.[68] They showed that the growth rate is enhanced above that of Kruer et al. Wong[69] has investigated the stability of two types of BGK modes, including the effects of resonant interaction with both trapped and untrapped electrons, and obtained results similar to those of Kruer et al. Mima

and Nishikawa have developed a theory without assuming any particular form of BGK mode, and predicted sideband instabilities over two wave-number ranges given by $|k - k_0| = (2n + 1)^{1/2}\, \omega_B/v_p$ or $|k - k_0| \ll \omega_B/v_p$, where v_p is the phase velocity of the large amplitude wave, and $n(\geq 0)$ is an integer.[70] Mima and Nishikawa later investigated the stability of a BGK mode whose untrapped particle distribution is chosen to be that given by the Landau linear theory.[71]

All of the theories discussed so far concentrated on investigation of the wave-wave interaction mechanism. An alternative approach is a quasilinear wave-particle interaction. Shapiro and Shevchenko,[72] and Bud'ko et al.,[73] have studied the excitation of sidebands due to resonant wave-particle interaction, using the O'Neil time-asymptotic solution[48] as their starting point. Bud'ko et al. found that only a lower sideband satisfying $|\omega - kv_p| \simeq 0.9\omega_B$ can be excited. However, for the parameters used in the experiment of Wharton et al., their theory does not predict instability. Shapiro and Shevchenko used a different distribution function for untrapped particles, and found that both sidebands can be excited with different growth rates. Substitution of the experimental parameters of Wharton et al. in their theory yields growing solutions, but the growth rates are much smaller than those obtained by Kruer et al.[57] The stability of the O'Neil solution has also been investigated by Manheimer, who considered only the particles trapped near the bottom of the potential wells, and predicted that the lower sideband is unstable while the upper sideband is stable.[74] His theory is considered to be a lower order approximation to the theories

of Shapiro and Shevchenko, and Bud'ko et al. In the quasilinear theory of Yagishita and Ichikawa,[75] the stability of the time-asymptotic distribution function found by Al'tshul and Karpman[49] (see Section 4) was studied. It was shown that the trapped electrons can cause sideband instability through interaction with externally excited test waves. The theories mentioned so far examine the stability of either a stationary or time-asymptotic equilibrium state, involving a large amplitude wave. In contrast, Brinca has used the quasilinear theory during the transient following application of a large amplitude wave at $t = 0$.[76] He determined the variation of the sideband growth rate, as a function of time, from the slope of the averaged velocity distribution function in the vicinity of the phase velocity of the large amplitude wave.

Examining the theories discussed so far, in the light of the results of our computer simulations in Section 5.2, it seems appropriate to compare the simulation results at early stages of temporal evolution with the theory of Brinca, and at later times with the theory of Kruer et al. In what follows, we shall, first, consider the quasilinear wave-particle interaction theory due to Brinca, and then the wave-wave interaction theory in the bunched beam approximation due to Kruer et al.

5.3.1 Quasilinear Theory

Theory: Consider a large amplitude, electron plasma wave, excited at time $t = 0$, in an infinite collisionless plasma. The electron motions are described by

$$\frac{dx}{dt} = v \ , \qquad \frac{dv}{dt} = - \frac{e}{m_e} E_0 \sin (\omega_0 t - k_0 x) \ , \tag{5.1}$$

where x and v are the position and velocity of an electron, and ω_0 is the frequency of the large amplitude wave. Since E_0 is assumed to be constant, Eq. (5.1) yields the first integral of the motion,

$$W = \frac{m_e}{2} \left(v - \frac{\omega_0}{k_0} \right)^2 + \frac{eE_0}{k_0} \cos (\omega_0 t - k_0 x) \ . \tag{5.2}$$

The distribution function in the presence of the large amplitude wave is determined by the Vlasov equation,

$$\frac{\partial f}{\partial t} + v \frac{\partial f}{\partial x} - \frac{e}{m_e} E_0 \sin (\omega_0 t - k_0 x) \frac{\partial f}{\partial v} = 0 \ . \tag{5.3}$$

Since Eq. (5.1) represents the characteristics of Eq. (5.3) in phase-space, the solution of Eq. (5.3) is given by

$$f(x,v,t) \simeq f_0 \left(\frac{\omega_0}{k_0} \right) + \frac{2}{k_0} \dot{\xi}_0(x,v,t) \ f_0' \left(\frac{\omega_0}{k_0} \right) , \tag{5.4}$$

in the resonant region, $v \simeq \omega_0/k_0$. Here, f_0 is the initial electron velocity distribution function, f_0' denotes the derivative of f_0 with respect to v , and $\dot{\xi}_0(x,v,t)$ is given by solution of Eq. (5.1) as

$$\dot{\xi}_0 = \pm \frac{1}{\kappa\tau} \, \mathrm{dn} \left[F(\kappa,\xi) \mp \frac{t}{\kappa\tau} \right] \qquad (\kappa^2 < 1) \ , \tag{5.5}$$

for untrapped particles, and by

$$\dot{\xi}_0 = \pm \frac{1}{\kappa\tau} \, \mathrm{cn} \left[F \left(\frac{1}{\kappa} \ , \ \zeta \right) \mp \frac{t}{\tau} \right] \qquad (\kappa^2 > 1) \ , \tag{5.6}$$

for trapped particles, where F represents the elliptic integral of the first kind, dn and cn are Jacobian elliptic functions, ξ_0 denotes the initial value of ξ, and κ, τ, ξ and ζ are defined by

$$\kappa^2 = \frac{2eE_0}{k_0 W + eE_0} , \qquad \tau = \frac{1}{\omega_B} = \left(\frac{m_e}{ek_0 E_0} \right)^{1/2} ,$$

$$\xi = \frac{1}{2} (k_0 x - \omega_0 t - \pi) , \qquad \sin \zeta = \kappa \sin \xi . \tag{5.7}$$

The positive or negative sign is used in Eqs. (5.5) and (5.6) according to whether $\dot{\zeta}$, $\dot{\xi} > 0$, or $\dot{\zeta}$, $\dot{\xi} < 0$. Equation (5.4) is valid provided that the amplitude is small enough to allow a Taylor expansion of the distribution function about the phase velocity of the large amplitude wave, i.e. $\omega_B/\omega_0 \ll (k_0 v_t/\omega_0)^2$.

Having found the solution of the Vlasov equation, the next step is to average Eq. (5.4) so as to remove fast oscillations occurring on a time scale $1/\omega_0$ and on a length scale $1/k_0$, and to obtain a slowly-varying velocity distribution $\langle f(v, \omega_B t) \rangle$. After some manipulation, the averaged solution

$$\langle f \rangle \simeq f_0 \left(\frac{\omega_0}{k_0} \right) + \langle w_0 \rangle \, f_0' \left(\frac{\omega_0}{k_0} \right) , \tag{5.8}$$

is obtained, in which

$$\langle w_0 \rangle = \frac{\pi \omega_B}{k_0 \kappa F(\kappa)} \left\{ 1 + 8 \sum_{n=1}^{\infty} \frac{Q^{2n}}{(1+Q^{2n})^2} \cos \left[\frac{n \pi \omega_B t}{\kappa F(\kappa)} \right] \right\} , \tag{5.9}$$

$$\langle w \rangle = w^* \frac{E(\kappa)}{\kappa} \qquad (\kappa^2 < 1) , \tag{5.10}$$

for the untrapped particles, and

$$\langle w_0 \rangle = \frac{8\pi\omega_B}{k_0 F(\eta)} \left\{ \sum_{n=1}^{\infty} \frac{Q^{2n-1}}{(1+Q^{2n-1})^2} \cos\left[\frac{(2n-1)\pi\omega_B t}{2F(\eta)}\right] \right\} , \tag{5.11}$$

$$\langle w \rangle = w^* \left[E(\eta) - (1 - \eta^2)F(\eta)\right] \quad \left(\eta^2 = \frac{1}{\kappa^2} < 1\right) , \tag{5.12}$$

for the trapped particles. In Eqs. (5.9)-(5.12), $F(\kappa)[= F(\kappa,\pi/2)]$ and $E(\kappa)[= E(\kappa,\pi/2)]$ are the complete elliptic integrals of the first and second kinds, and

$$\begin{aligned} w &= v - \frac{\omega_0}{k_0} , \qquad w^* = \frac{4\omega_B}{\pi k_0} , \\ Q &= \exp\left\{-\pi F[(1-\kappa^2)^{1/2}]/F(\kappa)\right\} . \end{aligned} \tag{5.13}$$

Since κ and η are related to the mean velocities defined by Eqs. (5.10) and (5.12), we see that $\langle w_0 \rangle$, which is a function of κ or η, is itself a function of the mean velocity.

In Fig. 5.7, $\langle w_0 \rangle$ is plotted as a function of velocity, with time as a parameter. It will be recognized from Eq. (5.8) that a plot of $\langle w_0 \rangle$ indicates the shape of the averaged velocity distribution function in the resonant region. It will be noted that $\langle w_0 \rangle$ develops finer and finer structure as time increases, resulting in progressively larger local slope of the velocity distribution function. The application of the theory is limited to the transient process at the initial stage of evolution, before the fine structure develops, i.e. up to $\omega_B t \sim 2\pi$.

If the averaged distribution function given by Eq. (5.8) is considered as a slowly-varying 'equilibrium' distribution function,

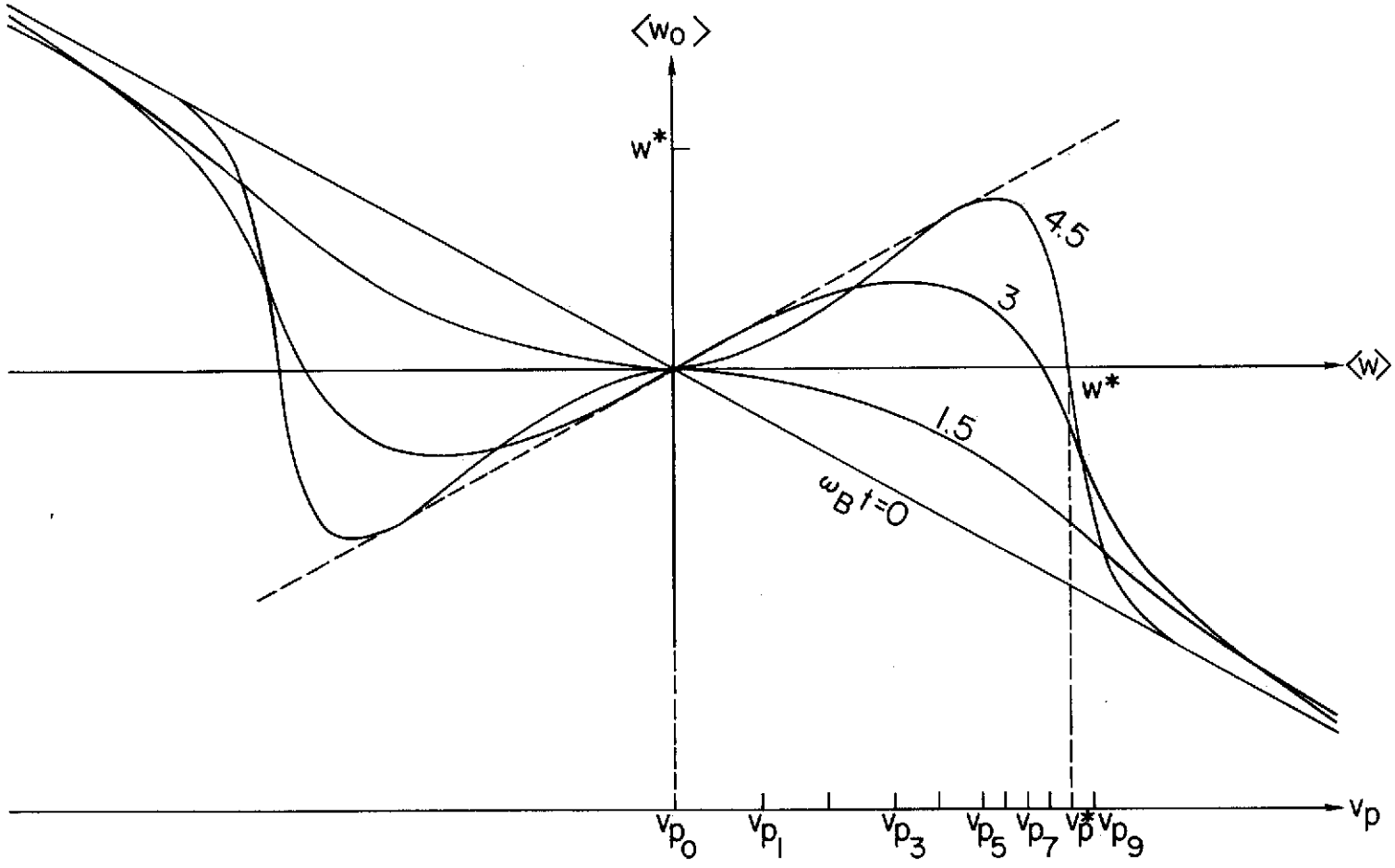

FIG. 5.7. Temporal behavior of the averaged distribution function in the resonant region. v_{p0} is the phase velocity of the main wave. The other v_p's are phase velocities of test waves. (Adapted from Fig. 1 of Ref. 76.).

then a small perturbation, f_1, due to application of a test wave may be described by the linearized Vlasov equation in the form

$$\frac{\partial f_1}{\partial t} + v \frac{\partial f_1}{\partial x} - \frac{e}{m_e} E_1 \frac{\partial \langle f \rangle}{\partial v} = 0 , \tag{5.14}$$

where E_1 is the perturbed electric field. Applying linear stability analysis for perturbations of the form $\exp[-i(\omega t - kx)]$, propagating with phase velocities near that of the large amplitude wave, yields a growth rate of

$$\gamma(t) = \frac{\pi}{2} \left(\frac{\omega_p^2}{k}\right)\left(\frac{\omega}{k} - \frac{d\omega}{dk}\right)\left(\frac{\partial \langle f \rangle}{\partial v}\right)_{v=\omega/k} , \tag{5.15}$$

where $\gamma \ll \omega$ has been assumed.

Having obtained this result, Brinca simplified it by assuming that the test waves are described by the warm plasma dispersion relation

$$\epsilon_p(k,\omega) = 1 - \frac{\omega_p^2}{\omega^2 - 3k^2 v_t^2} = 0 . \tag{5.16}$$

Equations (5.8), (5.15), and (5.16) are then sufficient to obtain the time evolution of the growth (or decay) rates of the test waves. Figure 5.8 presents some calculations. It will be seen that the sidebands decay initially (if they are above the thermal fluctuation level), and then start to grow; the larger the phase velocity separation between the test wave and the large amplitude wave, the stronger the initial damping.

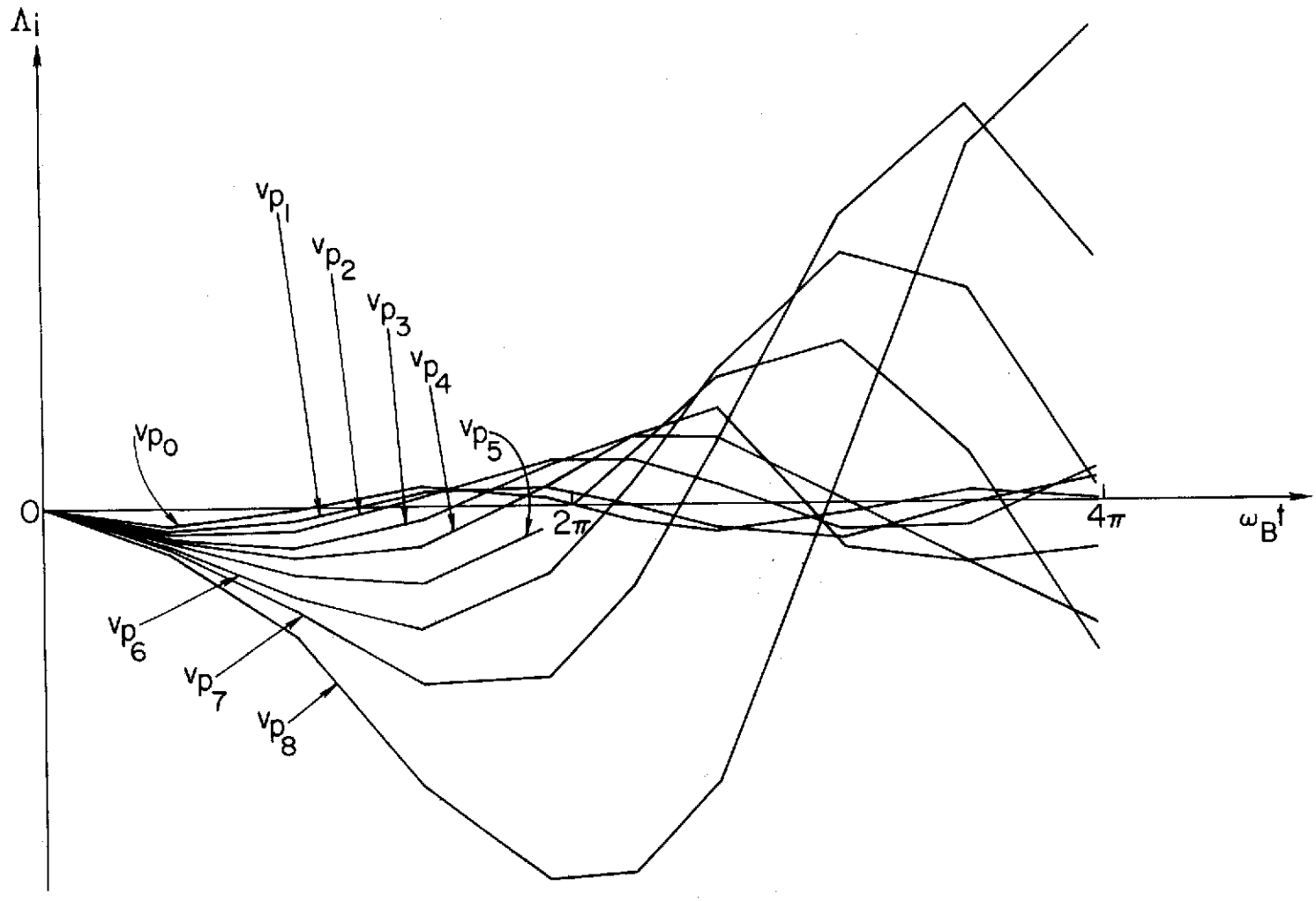

FIG. 5.8. Cumulative, logarithmic, temporal growth of test waves with phase velocities shown in Fig. 5.7. $[\Lambda_i = \int_0^t \gamma_i dt]$ (Adapted from Fig. 4 of Ref. 76.).

Comparison with Computations: The theoretical growth rate for the test waves in the initial development stage has been computed using Eqs. (5.8), (5.11), (5.12), (5.15) and (5.16). Equations (5.11) and (5.12) are used since $|\omega/k - \omega_0/k_0| < w^*$ holds for Modes 11 and 12 as shown in Fig. 5.2. The calculated results are shown in Fig. 5.9 for comparison with the growth rates measured from the simulation results presented in Fig. 5.1. Although the evolutionary patterns for Mode 12 from the theory and computation resemble each other to some extent, the agreement is not good. It should be borne in mind that the theory is applicable only to cases in which the main wave amplitude variation is negligible; in our simulation the amplitude actually varies by a factor of more than two during the period up to $\omega_p t = 30$. To obtain better agreement, we have used information from the detailed plot of the averaged velocity distribution function in Fig. 5.2. We have computed the growth rate, using Eq. (5.15), at intervals of $\omega_p t = 4$ from the local slope of the averaged velocity distribution function at the phase velocities of the test waves. The results are shown in Fig. 5.9. There is a striking similarity in evolutionary pattern for both modes between the measured growth rate and the theoretical one; there is a difference in $\omega_p t$ of about 3 for both modes until $\omega_p t \simeq 10$, and a difference of about 15 for Mode 11, and 10 for Mode 12, thereafter.

In seeking an explanation for this phenomenon, it should be recalled that in the quasilinear theory of Brinca there is an implicit assumption that the waves respond instantaneously to the slope of the averaged velocity distribution function. However, since transient phenomena

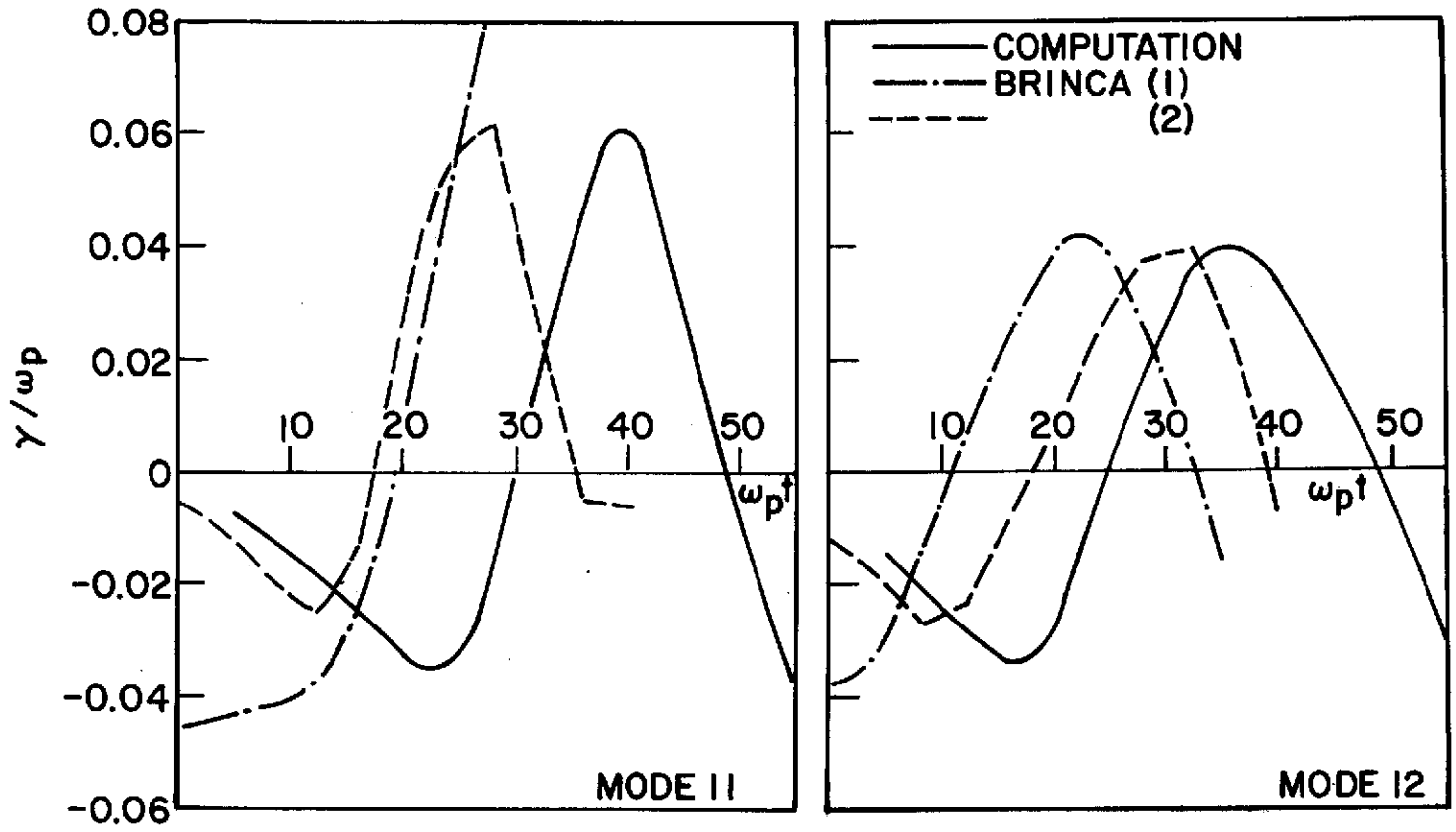

FIG. 5.9. Test wave growth rate at short times in the simulation shown in Fig. 5.1. Brinca (1) is the theoretical result calculated by the use of warm plasma dispersion relation [Eq. (5.16)]. Brinca (2) is the theoretical result obtained from Fig. 5.2.

are involved, it is more reasonable to assume that some time elapses before the macroscopic effects of the resonant wave-particle interaction appear. We may estimate this time delay as follows. From Fig. 5.2, the width of the bump in the velocity distribution function may be estimated to be $\delta v \simeq 0.6\ v_t$. Considering this bump as a set of streams with continuously distributed velocities, providing a continuous range of frequencies kv, we obtain the rise time, τ_d, of a perturbation from the approximate equality

$$k\delta v\tau_d \simeq \frac{\pi}{2} . \tag{5.17}$$

Substituting appropriate numerical values into this expression yields $\omega_p\tau_d \sim 10$ for Mode 11, and 9 for Mode 12. These results do not fully account for the discrepancies, of course, but provide a good intuitive explanation.

5.3.2 Wave-Wave Interaction Theory

Theory: The simplest model of sideband instability which incorporates wave-wave interaction is that involving the bunched beam approximation. In this approximation, the equilibrium distribution function is assumed to contain trapped particles localized at the bottom of the potential wells of a large amplitude wave propagating at phase velocity v_p. The trapped particles act coherently as harmonic oscillators of frequency $\omega_B[= (ek_0E_0/m_e)^{1/2}]$. The effects of trapped particles other than those near the bottom are neglected.

The trapped electrons are governed by the equation of motion

$$\frac{d^2x_n}{dt^2} = -\omega_B^2(x_n - x_{n0} - v_p t) - \frac{1}{(2\pi)^2}\int \frac{e}{m_e} E(k,\omega)\exp[-i(\omega t - kx_n)]dkd\omega \ , \tag{5.18}$$

where x_n is the position of a particle in the n-th potential well, $x_{n0} + v_p t$ is the position of the n-th well, and $E(k,\omega)$ is the Fourier transform of the perturbation electric field. The effects of the electric field of the large amplitude wave are taken care of by the first term on the right-hand side of Eq. (5.18).

Treating the trapped electrons as a source charge density introduced into a plasma of permittivity $\epsilon_p(k,\omega)$, we have

$$ik\epsilon_p(k,\omega)E(k,\omega) = \frac{\rho(k,\omega)}{\epsilon_0} \ , \tag{5.19}$$

where $\rho(k,\omega)$ is obtained from the Fourier transform of the displacement of the trapped particles given by Eq. (5.18). Some manipulation of Eqs. (5.18) and (5.19) yields

$$E(k,\omega) = \frac{\omega_T^2}{(\omega - kv_p)^2 - \omega_B^2}\sum_n \frac{E(k+nk_0, \omega+n\omega_0)}{\epsilon_p(k,\omega)} \ ,$$

$$\omega_T = \left(\frac{N_T e^2}{\epsilon_0 m_e \lambda_0}\right)^{1/2} \ , \qquad \lambda_0 = \frac{2\pi}{k_0} \ , \qquad \omega_0 = k_0 v_p \ , \tag{5.20}$$

where N_T is the number of trapped electrons in each potential well. Equation (5.20) shows that perturbations at ω, k are coupled to an infinity of perturbations at $\omega + n\omega_0$, $k + nk_0$.

Since plasma does not support wave propagation at frequencies greatly different from the plasma frequency, ω_p, the two waves $E(k,\omega)$ and $E(k-2k_0, \omega-2\omega_0)$ may be expected to be dominant for $\omega \sim \omega_p$. Retaining only these two terms yields two coupled mode equations for $E(k,\omega)$ and $E(k-2k_0, \omega-2\omega_0)$. The dispersion relation results from equating the determinant of their coefficients to zero. We obtain

$$1 = \frac{\omega_T^2}{\Omega^2-\omega_B^2}\left[\frac{1}{\epsilon_p(k,\omega)} + \frac{1}{\epsilon_p(k-2k_0,\ \omega-2\omega_0)}\right], \qquad (5.21)$$

where $\Omega = \omega - kv_p$. If the large amplitude wave is not too large, the warm plasma approximation for $\epsilon_p(k,\omega)$ [Eq. (5.16)] may be used.

Comparison with Computations: In Fig. 5.10 are plotted the theoretical growth rates for Modes 8-12, obtained by solving Eq. (5.21) combined with Eq. (5.16). To make quantitative comparisons, the growth rates of the unstable modes were measured in the five simulations (A-E) described in Section 5.2. The growth rates were obtained from energy/time plots for each unstable mode, similar to those shown in Figs. 5.1 and 5.4, and plotted in Fig. 5.10. The errors involved in measuring the growth rates of the sidebands were about 10%. We see that there is good agreement for small values of ω_B, but that the measured growth rates tend to be larger than the theory predicts for large values of ω_B. In considering the discrepancies, it should be remembered that the theory is not valid for very large amplitude main waves, i.e. we require $E_0^2/4\pi nk_BT \ll 1$, and that values of the bounce frequency, ω_B, used in this plot are not those corresponding to the initial amplitudes

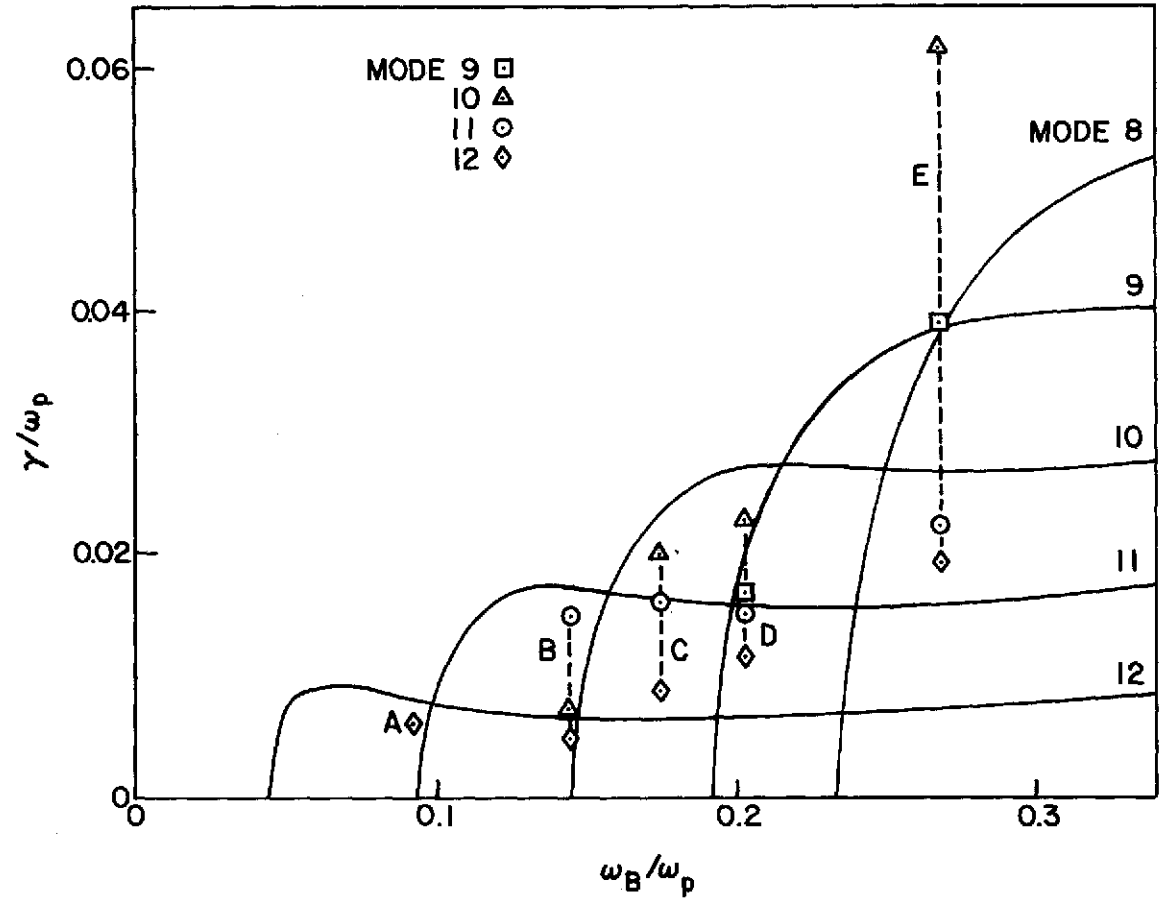

FIG. 5.10. Sideband growth rate at later times vs. bounce frequency. Solid lines are solutions of Eq. (5.21) combined with Eq. (5.16).

of the main wave, but have been estimated from the expected time-asymptotic amplitudes indicated by dashed lines in Figs. 5.1 and 5.4.

5.4 Comparison with Experiments

In comparing the results of our simulations with those of laboratory experiments,[66,77,78] it should be noted that the simulations were carried out for an initial value problem, rather than a boundary value problem. Since laboratory experiments deal with spatial phenomena, direct quantitative comparison may not be appropriate. Under certain conditions, however, it may be possible to transform an initial value problem into a boundary value problem so as to allow quantitative comparison with the experimental data. For example, as found by Lee and Schmidt,[55] the O'Neil solution for a temporal case can be transformed into a spatial solution by replacing the normalized time, $\omega_B t$, and the parameter γ_L/ω_B, by x/λ_B and $\beta_L\lambda_B$, where $\lambda_B = \omega/k\omega_B$ and $\beta_L = \gamma_L/(\partial\omega/\partial k)$.

In making this transformation, it should be remembered that in the simulation the system length is finite, and only a finite number of wavenumbers are available with equal separation $2\pi/L$. As a consequence, it may well be that the fastest growing mode observed in the simulation is not the fastest growing mode predicted by theory for an infinite plasma. This implies that an accurate measurement of the dependence of the sideband peak frequency separation, $\Delta\omega$, and sideband growth rate, γ, is not available from our simulations. Nevertheless, the data plotted in Fig. 5.10 seem to suggest $\gamma \propto E_0^{\alpha}$, with $\alpha > 1/2$, which is to be compared with the experimental observations that $\Delta\omega \propto E_0^{1/2}$, $\gamma \propto E_0^{1/2}$ by Franklin et al.,[77] that

$\Delta\omega \propto E_0^{1/2}$, $\gamma - \gamma_0 \propto E_0^{1.2}$ (γ_0 is a constant) by Jahns and Van Hoven,[78] and that $\Delta\omega \simeq \omega_B$ by Wharton et al.[66] These measurements could be made in the simulation, of course, by making the system longer, but we did not pursue this because of the high costs involved. Even so, a number of characteristic features of the laboratory observations on sideband instability correspond to those described in Section 5.2. In fact, all of the features (a)-(e) predicted by the computer simulation were observed in the laboratory experiments.

In terms of the strength of the main wave, our simulations lie between previous computer simulations[11,80,81] and the laboratory experiments.[66,77,78] Our simulations were carried out in the main wave amplitude range $0.06 \lesssim eE_0/m_e v_t \omega_p \lesssim 0.50$. In the previous simulations, the range was $0.5 \lesssim eE_0/m_e v_t \omega_p \lesssim 0.7$. Note, however, that the amplitude quoted is the maximum level reached at the end of the period during which the system was excited externally at the frequency of the main wave. On the other hand, the main wave amplitude in the laboratory experiments was $2 \times 10^{-3} \lesssim eE_0/m_e v_t \omega_p \lesssim 0.02$ (Wharton et al.), $0.02 \lesssim eE_0/m_e v_t \omega_p \lesssim 0.1$ (Franklin et al.), and $0.03 \lesssim eE_0/m_e v_t \omega_p \lesssim 0.3$ (Jahns and Van Hoven). It will be seen, therefore, that our simulations were performed for conditions more appropriate to the laboratory experiments than the previous simulations of sideband instability.

5.5 Summary

In this section, we have simulated the sideband instability as an initial value problem for comparison with existing theories and experimental results. The initial development has been shown to be explicable by the quasilinear theory of Brinca in cases where the main wave

amplitude is relatively small ($\omega_B/\omega_p \leq 0.2$), and the test wave growth (or damping) rate is not too large compared with its frequency ($\gamma \ll \omega$) .

The later stages of evolution of the sideband instability, after one or two phase-space rotations of the particles have been completed, have been shown to be well described by the wave-wave interaction theory in the bunched beam approximation of Kruer et al. For very large main wave amplitude ($\omega_B/\omega_p \geq 0.2$), the simulation gives higher growth rate than the theory predicts.

Comparison with the laboratory experiments has shown that many features of the instability observed in our simulation at similar signal levels are consistent with the experimental observations, account always being taken of the fact that the simulation is for temporal evolution, and laboratory experiments for spatial evolution. The dependence of the frequency separation, $\Delta\omega$, and sideband growth rate, γ , upon the wave amplitude, E_0 , still need to be checked.

6. SATELLITE GROWTH

6.1 Introduction

The computer simulations to be described in this Section were stimulated by laboratory observations by Jahns and Van Hoven of satellite growth at frequency $\omega_2 (= 2\omega_0 - \omega_1)$ when a large amplitude signal at ω_0, and a small amplitude signal at ω_1 were excited simultaneously.[83] Jahns and Van Hoven interpreted the satellite growth as being due to four-wave passive coupling. They applied a perturbation expansion method[84] of solving the Vlasov and Poisson equations to a spatial problem appropriate to their experiment, and obtained a solution, describing the spatial evolution of the satellite.[85] However, the predicted dependence of the satellite growth rate upon the amplitude of the signal at ω_0 did not fit the observed dependence. Jahns and Van Hoven ascribed the discrepancies to dissipation, higher-order processes, and wavenumber mismatch.

DeNeef made similar observations to those of Jahns and Van Hoven in his experiments with a large amplitude wave and a small amplitude wave launched simultaneously.[86] He considered the small amplitude wave as a slow modulation of the amplitude and phase of the large amplitude wave, and calculated the amplitudes of the small amplitude wave and the satellite wave as a function of position. His calculation showed agreement with the experiments for the former, but not for the latter. In particular, the energy level of the satellite wave observed in the experiment was 90 dB below the theoretical prediction. DeNeef suggested that the discrepancy might be due to the strong dependence of the satellite behavior on the nonlinear wavelength shift of the

large amplitude wave. In his theory, he used the wavelength shift calculated from the theory of Morales and O'Neil.[60]

Brinca considered such a process for the analogous temporal problem in which the synchronism relations

$$2k_0 = k_1 + k_2 , \qquad 2\omega_0 = \omega_1 + \omega_2 , \tag{6.1}$$

are satisfied.[87] He obtained coupled-mode equations which describe the temporal evolution of the wave amplitudes. The theory failed, however, to give either the observed rapid growth rate, or the observed satellite energy level.

In what follows, we shall demonstrate good agreement between computer simulations and theoretical predictions based on DeNeef's method applied to a temporal problem rather than a spatial one. Unlike DeNeef, we use the measured nonlinear frequency shift in the calculation of the wave evolution. The computer simulation is discussed in Section 6.2. The theory is described in Section 6.3, and compared with the simulation in Section 6.4.

6.2 Computations

In the simulations to be described, 16348 particles were followed in a system 256 λ_D long, divided into 256 cells. The continuous Maxwellian distribution was replaced by 64 beams spaced $v_t/7$ apart. Velocity-space was covered from $-4.5\ v_t$ - $4.5\ v_t$ by a grid with mesh size equal to the beam spacing. Periodic smoothing was carried out every 16 time-steps, a time-step being $0.25/\omega_p$. Periodic boundary conditions were applied in space.

Perturbations of the form given by Eq. (3.23) were applied in Modes 13 and 12 at $t = 0$. Figure 6.1 shows the results of the simulation for two different main (large amplitude) wave amplitudes, and three different test (small amplitude) wave amplitudes. It will be seen that in each case the main wave evolves almost exactly as a single large amplitude wave (compare with Fig. 4.1), i.e. the main wave amplitude is not large enough to cause appreciable sideband growth, due to trapped particle instability of the type studied in Section 5, on the time scale for which the satellite grows and saturates. The test wave follows a very similar evolution to that of the main wave. The satellite grows from noise, saturates at a level comparable to that of the test wave, and seems to show oscillatory behavior thereafter.

From Fig. 6.1(a)-(c), we observe that the behavior of the test wave and the satellite is almost identical for different test wave amplitudes, except that the curves are shifted vertically by an amount which scales linearly with the test wave amplitude. This is so only when the test wave amplitude remains small compared with the main wave amplitude. If increased progressively it finally disrupts the particle trapping by the main wave, and hence affects the main and test wave evolution. From Fig. 6.1(c)-(e) it will be seen that the growth rate of the satellite seems to decrease as the main wave amplitude decreases.[88]

When the roles of Modes 12 and 14 are switched, Mode 12 is observed to grow from noise, reach the level of Mode 14, and finally exceed it. We have confirmed that halving the beam spacing changes the results only in minor details.

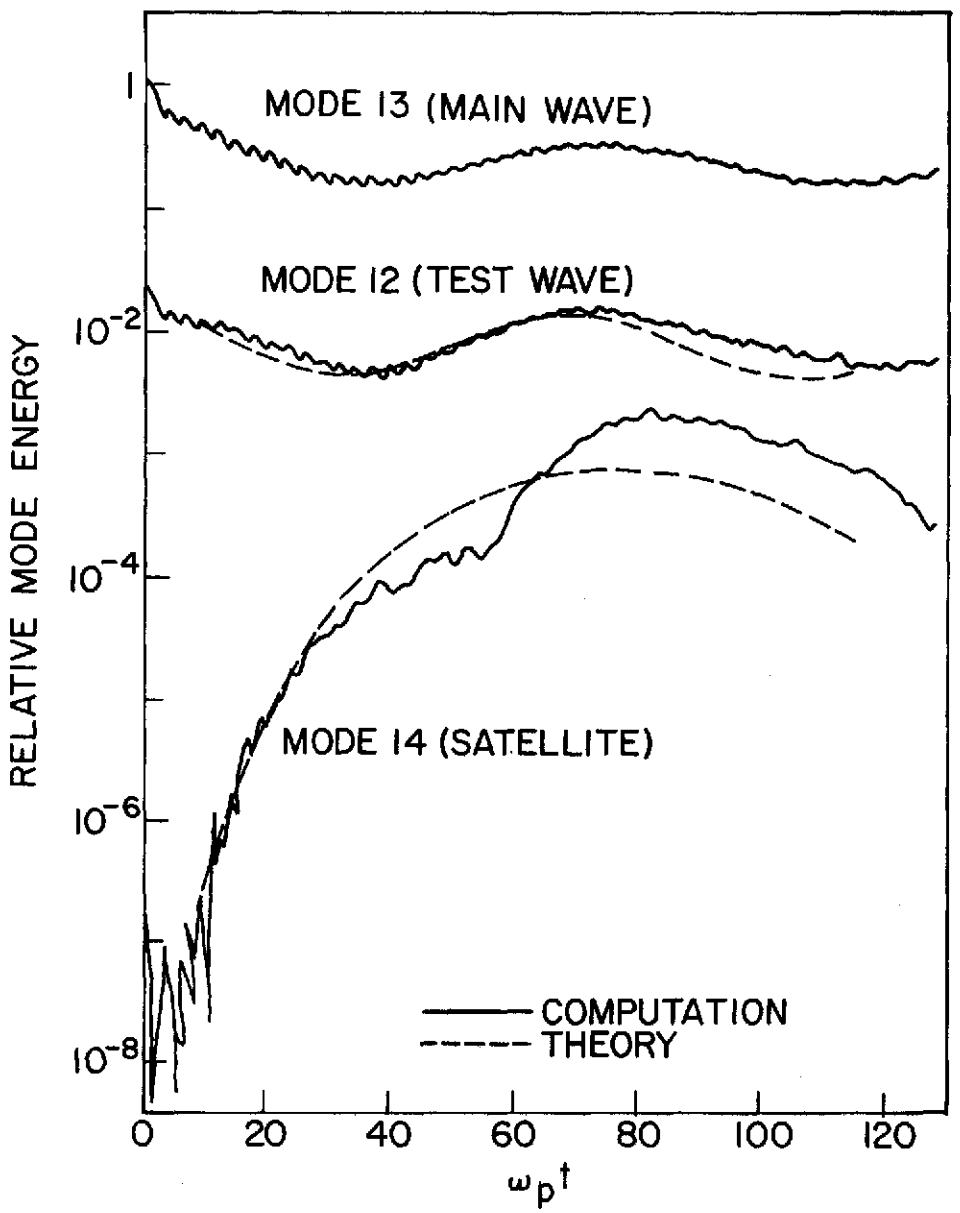

FIG. 6.1. Temporal evolution of main, test, and satellite waves.
(a) (Main wave electrostatic energy/thermal energy) = 1.86×10^{-3}.
(Test wave electrostatic energy/thermal energy) = 4.18×10^{-5}.

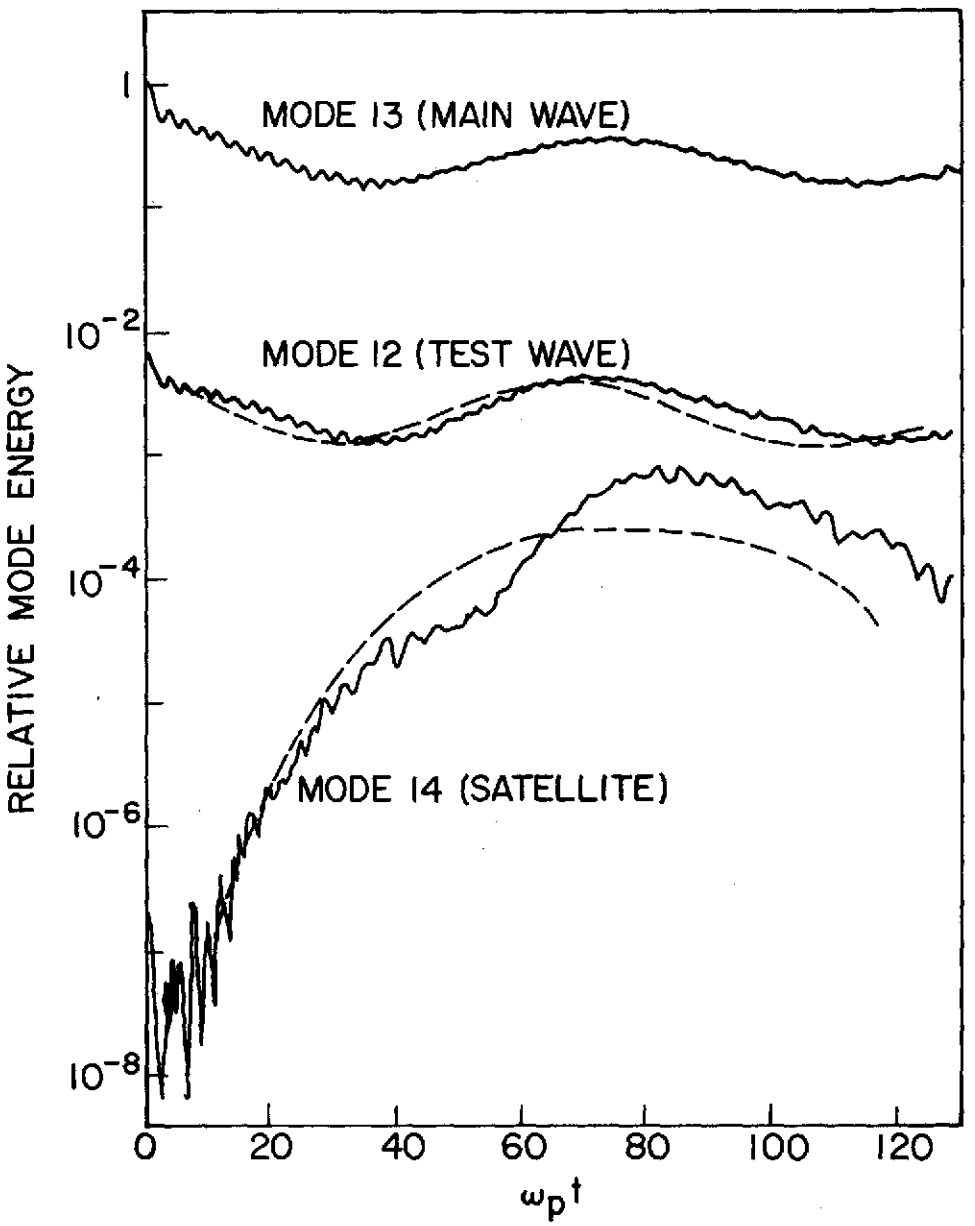

FIG. 6.1. Temporal evolution of main, test, and satellite waves.
(b) (Main wave electrostatic energy/thermal energy) = 1.86×10^{-3}.
(Test wave electrostatic energy/thermal energy) = 1.16×10^{-5}.

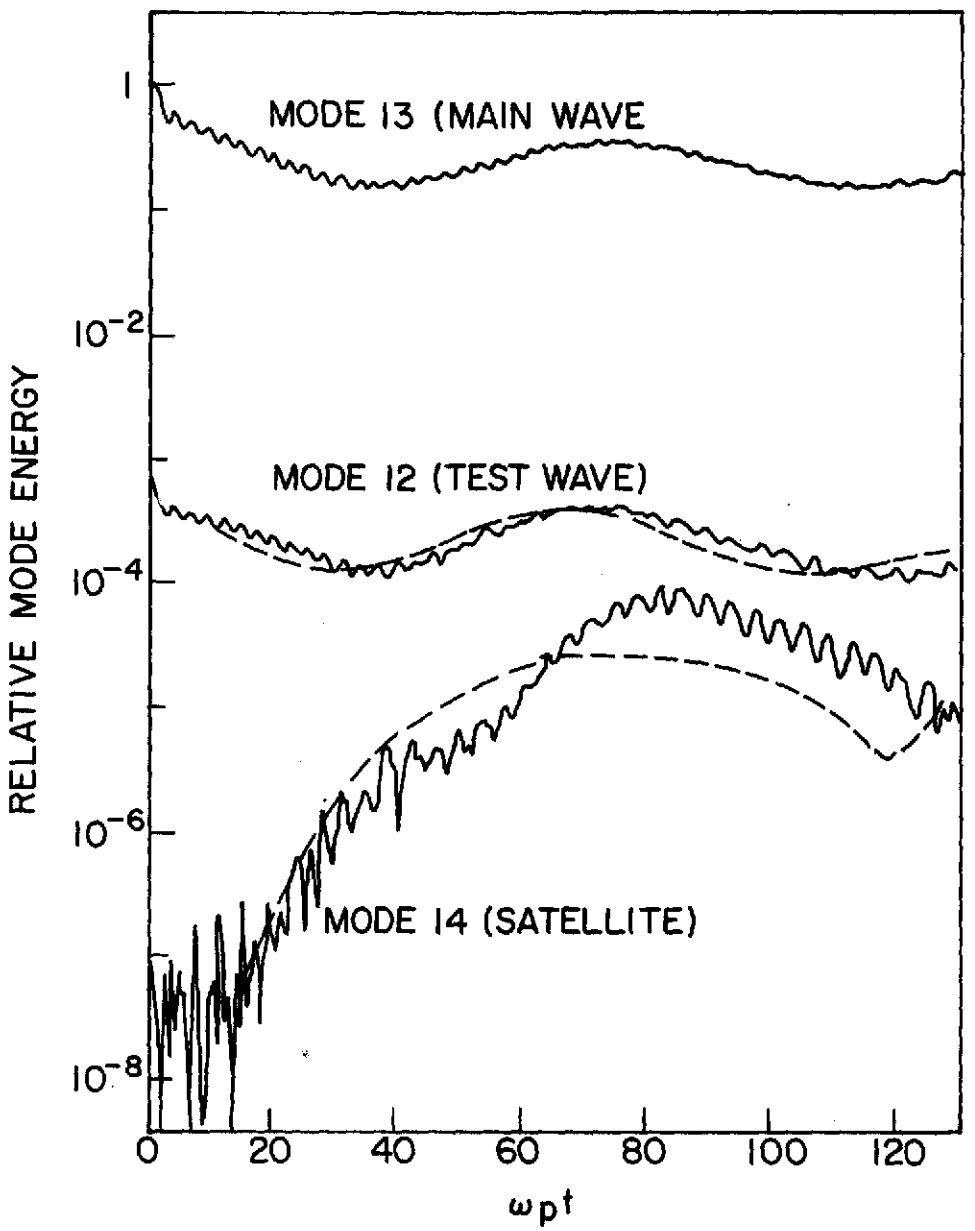

FIG. 6.1. Temporal evolution of main, test, and satellite waves.
(c) (Main wave electrostatic energy/thermal energy) = 1.86×10^{-3}.
(Test wave electrostatic energy/thermal energy) = 1.16×10^{-6}.

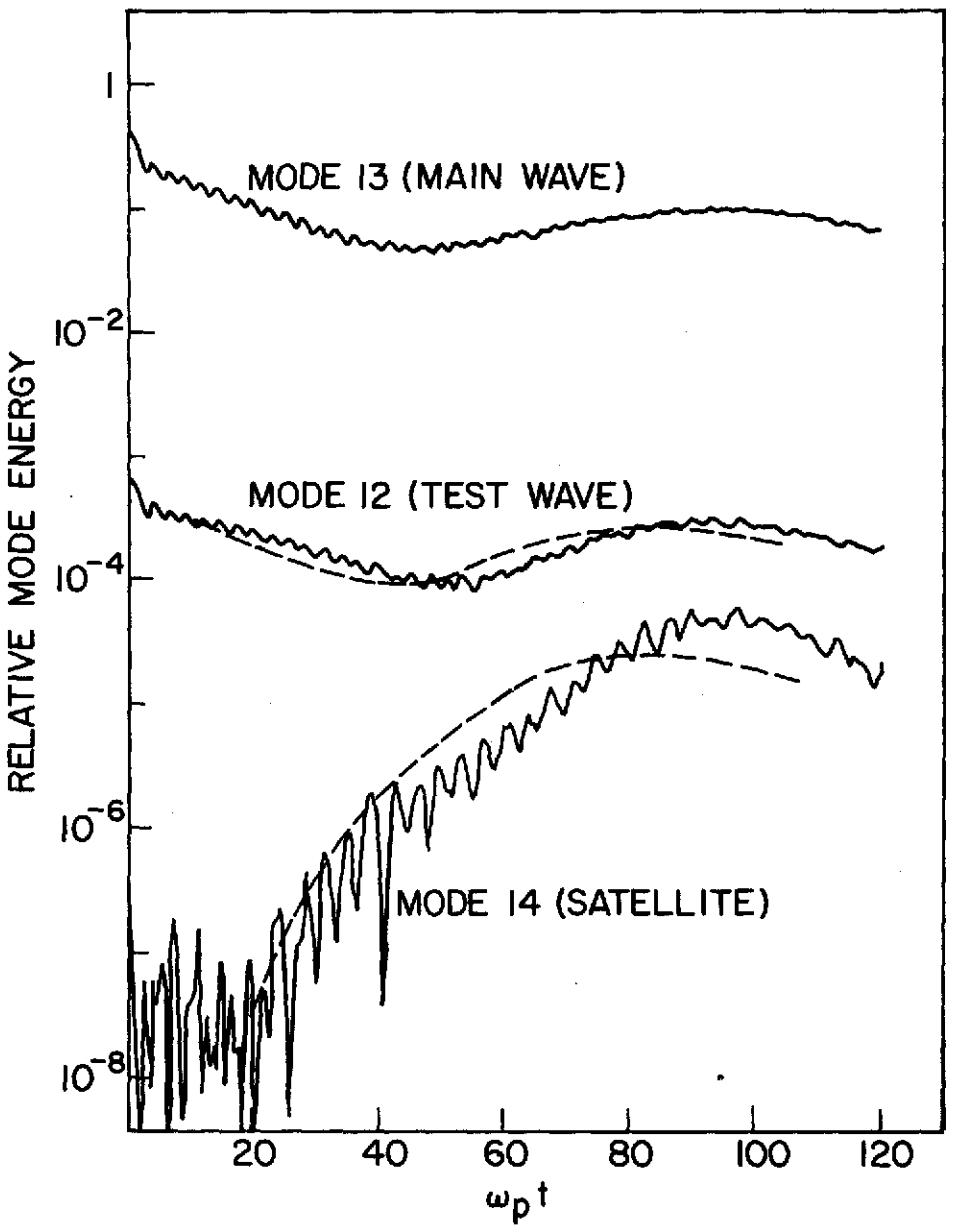

FIG. 6.1. Temporal evolution of main, test, and satellite waves.
(d) (Main wave electrostatic energy/thermal energy) = 7.25×10^{-4}.
(Test wave electrostatic energy/thermal energy) = 1.16×10^{-6}.

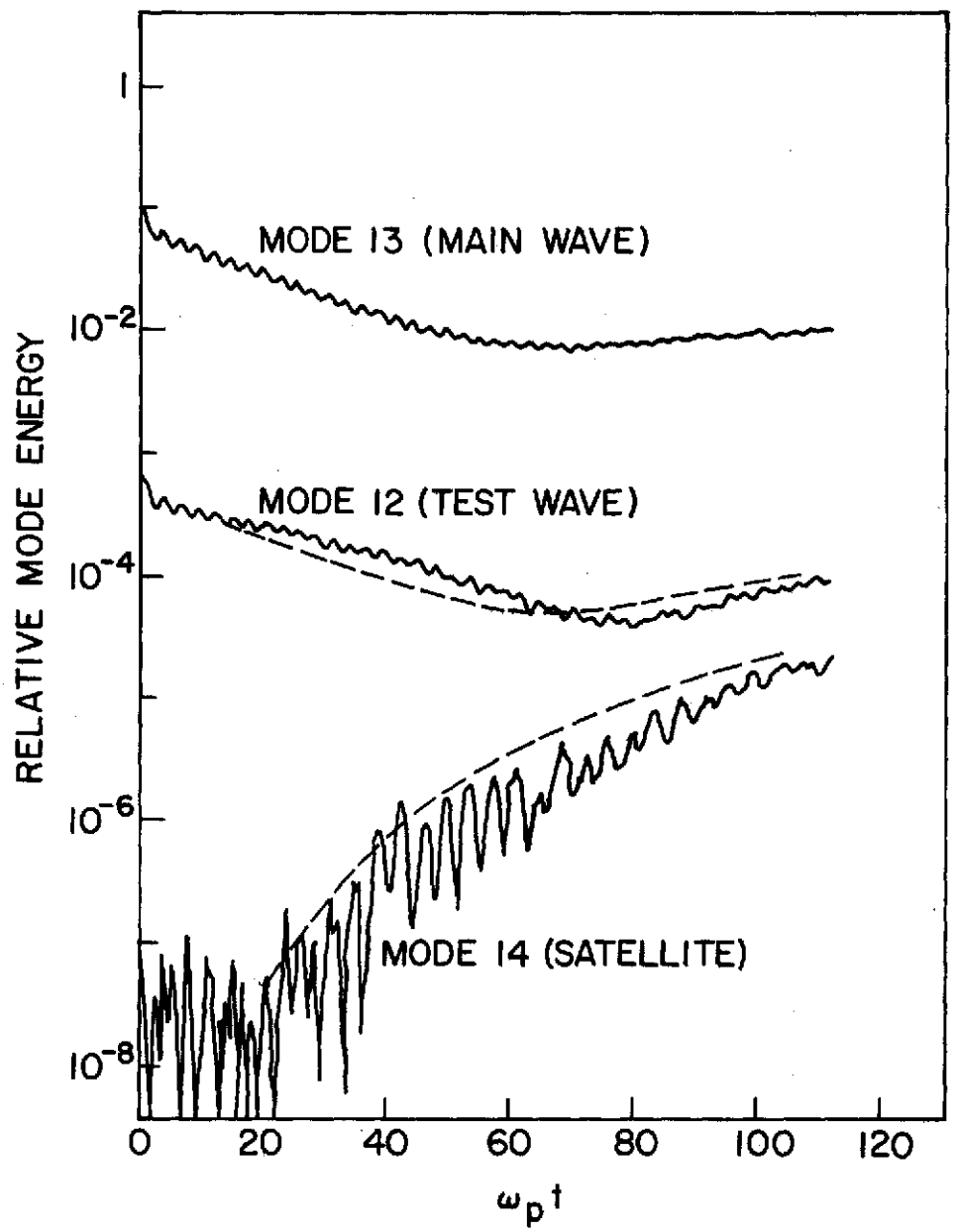

FIG. 6.1. Temporal evolution of main, test, and satellite waves.
(e) (Main wave electrostatic energy/thermal energy) = 1.96×10^{-4}.
(Test wave electrostatic energy/thermal energy) = 1.16×10^{-6}.

6.3 Theory

At time $t = 0$, the total electric field due to the main wave and the test wave is given by

$$E(x,0) = \{E_0 \exp ik_0x + \epsilon E_0 \exp i(k_0 - \Delta k)x\} + \{c.c.\} , \quad (6.2)$$

where E_0 is the test wave amplitude, and c.c. denotes complex conjugate. When ϵ is small, Eq. (6.2) can be written as

$$\begin{aligned} E(x,0) &\simeq c^2(x)E_0 \exp[ik_0x - \theta(x)] + \{c.c.\} , \\ c^2(x) &= \exp(\epsilon \cos \Delta kx) \simeq 1 + \epsilon \cos \Delta kx , \\ \theta(x) &= \epsilon \sin \Delta kx . \end{aligned} \quad (6.3)$$

This shows that the test wave can be regarded as (spatial) modulation of the amplitude and phase of the main wave when $\epsilon \ll 1$.

In the absence of modulation, the electric field of the main wave is given by

$$E_u(x,t) = E_0\left[\exp \frac{1}{\omega_B}\int_0^{\omega_B t} \Omega(t')dt'\right] \exp[-i(\omega_0 t - k_0 x)] + \{c.c.\}, \quad (6.4)$$

$$\Omega(t') = -[i\delta\omega(t') + \gamma(t')] , \qquad t' = \omega_B t ,$$

where $\delta\omega$ is the nonlinear frequency shift, and γ is the damping rate of the main wave. It is assumed that $\delta\omega$ and γ are functions of amplitude and time only through the product $\omega_B t$, and that ω_B is independent of time. The use of the form given by Eq. (6.4) would be valid if $\gamma_L/\omega_B \ll 1$, where γ_L is the linear Landau damping rate of the main wave.[48]

To incorporate the slow amplitude and phase variations in space due to the presence of the test wave, E_0 is replaced by $c^2(x)E_0$, and the phase $\theta(x)$ defined in Eq. (6.3) is included. The modulated wave is then given by,

$$E_m(x,t) = c^2(x)E_0 \exp\left[\frac{1}{c(x)\omega_B}\int_0^{c(x)\omega_B t}\Omega(t')dt'\right] \times \exp\left(-i[\omega_0 t - k_0 x + \theta(x)]\right) + \{c.c.\} \quad . \tag{6.5}$$

Equation (6.5) gives a solution in space for a given amplitude, $c^2(x)E_0$, and initial phase, $\theta(x)$. If Δk is given, the solution of Eq. (6.5) is correct only for time $t < 2\pi/\Delta k v_p$, where v_p is the phase velocity of the main wave.

To obtain the temporal evolution of the Fourier modes, Eq. (6.5) is Fourier-transformed in space by the relation,

$$E_m(k,t) = \int dx \exp(-ikx)E_m(x,t) \quad . \tag{6.6}$$

We obtain, after some manipulation,

$$|E_m(k,t)| = E_u(t)\left\{\delta(k-k_0) + \epsilon\left[(1+A(t))^2 + B^2(t)\right]^{1/2}\delta(k-k_0+\Delta k) + \epsilon\left[A^2(t) + B^2(t)\right]^{1/2}\delta(k-k_0-\Delta k) + O(\epsilon^2)\right\} , \tag{6.7}$$

where $\delta(\ )$ is the Dirac delta-function, and

$$E_u(t) = E_0 \exp\left[-i\omega_0 t + \frac{1}{\omega_B}\int_0^{\omega_B t} \Omega(t')dt'\right] + \{c.c.\} ,$$

$$A(t) = \frac{1}{4}\left[\gamma(t)t - \frac{1}{\omega_B}\int_0^{\omega_B t} \gamma(t')dt'\right] ,$$

$$B(t) = \frac{1}{4}\left[\delta\omega(t)t - \frac{1}{\omega_B}\int_0^{\omega_B t} \delta\omega(t')dt'\right] . \qquad (6.8)$$

Equation (6.7) shows that the main wave is unchanged to order ϵ, and predicts the existence of a satellite at $k_0 + \Delta k$. Note that the satellite is linear in the test wave amplitude, ϵE_0, consistent with the results of the simulation shown in Fig. 6.1(a)-(c). The change in the growth rate to be seen in Fig. 6.1(c)-(e) when the main wave amplitude is varied, is suggested by Eq. (6.7), since $A(t)$ and $B(t)$ depend on the main wave evolution.

6.4 Comparison with Simulation

To make calculations from Eq. (6.7), we need to know values of $\delta\omega$ and γ to be substituted in Eq. (6.8). Although the nonlinear frequency shift, $\delta\omega$, and growth rate, γ, have been predicted theoretically,[48,60] we prefer to use $\delta\omega(t)$ and $\gamma(t)$ determined from the results of our simulation. This avoids error due to the observed main wave evolution not being exactly as these theories predict. To determine $\delta\omega(t)$ and $\gamma(t)$, we have first tabulated the phase change and amplitude of the complex Fourier amplitude of the main wave after every time-step.

Since these quantities contain large ripples, we have smoothed them using the least-square polynomial of degree one through five successive amplitudes. In Fig. 6.1 are plotted the theoretical calculations from Eq. (6.7) using these values. We see that there is good agreement between the theory and the simulation. In particular, the theoretical growth rate of the satellite at the earliest stage increases as the main wave amplitude increases, in very good agreement with the simulation. It is also significant that in each case the observed satellite energy level is in agreement with the calculated one. Although the calculated behavior of the test wave agrees well with the simulation, detailed observation shows that the simulated test wave first damps at the linear Landau damping rate, and then at the increased rate in agreement with the calculated one.

6.5 Summary

We have studied the temporal behavior of the satellite wave produced when a large amplitude electron plasma wave and a small amplitude test wave are launched simultaneously. It has been shown that a theory which treats the test wave as a slow modulation of the amplitude and phase of the main wave explains well quantitatively the rapid growth and energy level of the satellite observed in our computer simulation.

7. CONCLUSIONS

In Sections 2-6, we have studied linear and nonlinear phenomena associated with electron plasma waves, using a low-noise hybrid simulation model. Despite its attractive features, little use had previously been made of this model since it was proposed by Denavit in 1972.[6]

In Section 3, the model was first studied in detail, and demonstrated to simulate precisely the linear wave dispersion characteristics predicted by theory for long wavelength collective behavior. This verification of the validity and effectiveness of the simulation model is very important as a starting point for the subsequent study of nonlinear phenomena. It also serves to establish the validity of the widely-used Cloud-in-Cell model, and the Langdon theory describing the finite-size particle model. Quantitative results in the very low energy range discussed here have never been obtained previously with such a high degree of accuracy with the simple particle models of Section 2.

In Section 4, the low-noise model was used to investigate the behavior of a monochromatic wave in both the linear and nonlinear régimes. It was found that existing nonlinear theories are qualitatively in good agreement with the simulation results, but that there are some significant differences. In particular, the phase-mixing has been found to be slower than predicted. A new contribution of this section is a measurement of the nonlinear frequency shift, which is shown to vary as $E_0^{1/2}$.

Section 5 was devoted to the investigation of the sideband, or trapped-particle, instability. Very good agreement was obtained for

$\omega_B/\omega_p \leq 0.2$ between the results of the simulation, and a simple theory by Kruer et al. and a quasilinear theory by Brinca. We have not studied in detail the characteristics of the sideband instability for a heavily-damped main wave. This problem remains to be investigated further by both simulation and theory.

In Section 6, we have studied nonlinear process involving coupling between a test wave and a large amplitude wave to produce a satellite wave. A simple theory, based on modulation of the large amplitude wave, was shown to explain the behavior of the satellite wave. This process may have important consequences in connection with the sideband instability discussed in Section 5: when a test wave in one sideband is launched at a level above the fluctuation level, as is often done in experiments on the sideband instability, a corresponding wave in the other sideband may grow rapidly to a comparable level to that of the test wave, before the effects of the trapped particle instability discussed in Section 5 come into play. As a consequence, this nonlinear process may, for example, affect the measured energy spectrum independently of the sideband instability.

We wish to emphasize in connection with Sections 3-6 that all of the simulations that have been presented were carried out under conditions for which the assumptions of relevant theoretical models could be approached, and in realistic energy ranges compared with those under which laboratory experiments are performed. It should be noted in relation to the latter, however, that our simulations have been concerned with temporal variations in a periodically bounded system, rather than with spatial variations in an effectively unbounded system.

Although we have investigated only one-dimensional problems, it seems straightforward to extend the hybrid simulation model to two and three dimensions. The effects of magnetic field could also be included at the cost of increased complication. The smoothing operation becomes more involved and time-consuming as the dimensionality is increased, and magnetic field is included. Even if it may not yet be economically feasible to extend its use to multidimensional problems with magnetic field included, the hybrid simulation model can serve very well, with reasonable cost, to achieve a very low fluctuation level given the capacity of currently available computers.

APPENDIX: DERIVATION OF WEIGHTING FUNCTIONS

Derivation:

Consider a smoothing operation in velocity-space,[6]

$$\tilde{f}(v_i) = \sum_v f(v) w(v_i - v) \ , \tag{A.1}$$

where v_i denotes the i-th velocity grid point, and the summation is over particle velocity, v. The n-th order moment of the distribution function before smoothing is

$$\langle v^n \rangle = \sum_v v^n f(v) \ . \tag{A.2}$$

After smoothing, the n-th order moment is given by

$$\langle \tilde{v}^n \rangle = \sum_i v_i^n \, \tilde{f}(v_i) \ . \tag{A.3}$$

Substituting Eq. (A.1) into Eq. (A.3) and equating $\langle v^n \rangle$ and $\langle \tilde{v}^n \rangle$ yields

$$\sum_i v_i^n \, w(v_i - v) = v^n \ , \tag{A.4}$$

for any value of v.

Velocity, v, can always be expressed as

$$\begin{aligned} v &= v_j + \delta v_j \\ &= (j + r)\Delta v \qquad (0 \le r \le 1) \ , \end{aligned} \tag{A.5}$$

where v_j $[= j\Delta v]$ denotes the nearest velocity grid point such that $v_j \leq v$, δv_j is the increment from the grid point, and Δv is the velocity grid size. Substituting Eq. (A.5) into Eq. (A.4), and letting $p = i - j$, gives

$$\sum_p (j + p)^n w[(p - r)\Delta v] = (j + r)^n . \qquad (A.6)$$

Using the binomial expansion, it will be seen that Eq. (A.6) is satisfied if

$$\sum_p p^m w[(p - r)\Delta v] = r^m \qquad (m = 0, 1, \ldots n) . \qquad (A.7)$$

Consider the Lagrangian interpolation of the function r^m, with $n + 1$ points, given by[89]

$$\sum_{p=1-s}^{s} p^m A_p^{(n+1)}(r) = r^m , \qquad (A.8)$$

where the $A_p^{(n+1)}(r)$ are the Lagrangian coefficients with $0 \leq r \leq 1$, and s is an integer. Since $m \leq n$, the interpolation is exact. Comparing Eqs. (A.7) and (A.8), it follows that the desired weighting function may be given by

$$w[(p - r)\,\Delta v] = A_p^{(n+1)}(r) . \qquad (A.9)$$

Rewriting Eq. (A.9) gives

$$w(v) = A_p^{(n+1)}\left(p - \frac{v}{\Delta v}\right) \qquad [(p - 1)\Delta v \leq v \leq p\,\Delta v] , \qquad (A.10)$$

where $1 - s \leq p \leq s$.

When n is odd, the weighting function is given by Eq. (A.10) with $s = (n+1)/2$. When n is even, the Lagrangian coefficients do not give even weighting functions. In this case, they may be obtained by symmetrization as follows,

$$w(v) = \begin{cases} \frac{1}{2} A^{(n+1)}_{-(n/2)}\left(1 + \frac{n}{2} + \frac{v}{\Delta v}\right) & \left[-\left(\frac{n}{2}+1\right)\Delta v \le v \le -\frac{n}{2}\Delta v\right], \\ \frac{1}{2} A^{(n+1)}_{p}\left(p - \frac{v}{\Delta v}\right) + A^{(n+1)}_{1-p}\left(1-p + \frac{v}{\Delta v}\right) & \left[(p-1)\Delta v \le v \le p\Delta v\right], \\ \frac{1}{2} A^{(n+1)}_{-(n/2)}\left(1 + \frac{n}{2} - \frac{v}{\Delta v}\right) & \left[\frac{n}{2}\Delta v \le v \le \left(\frac{n}{2}+1\right)\Delta v\right], \end{cases} \tag{A.11}$$

where $1 - s \le p \le s$, and $s = (n+2)/2$.

Although the weighting functions were derived for velocity-space, Eqs. (A.10) and (A.11) can be used for coordinate-space by replacing v by x.

Examples: For $n=1$, Eq. (A.10) is written as

$$w^{(1)}(v) = \begin{cases} A^{(2)}_{0}\left(-\frac{v}{\Delta v}\right) = 1 + \frac{v}{\Delta v} & (-\Delta v \le v \le 0), \\ A^{(2)}_{1}\left(1 - \frac{v}{\Delta v}\right) = 1 - \frac{v}{\Delta v} & (0 \le v \le \Delta v). \end{cases} \tag{A.12}$$

The smoothing operation using this weighting function conserves particles and momentum.

For $n=2$, applying Eq. (A.11) yields

$$w^{(2)}(v) = \begin{cases} \frac{1}{2}\left[A_1^{(3)}\left(1 - \frac{v}{\Delta v}\right) + A_0^{(3)}\left(\frac{v}{\Delta v}\right)\right] = 1 - \frac{3v}{\Delta v} - \frac{1}{4}\left(\frac{v}{\Delta v}\right)^2 \\ \qquad\qquad (0 \le v \le \Delta v) , \\ \frac{1}{2} A_{-1}^{(3)}\left(2 - \frac{v}{\Delta v}\right) = \frac{1}{4}\left(2 - \frac{v}{\Delta v}\right)\left(1 - \frac{v}{\Delta v}\right) \qquad (\Delta v \le v \le 2\Delta v) . \end{cases}$$

In the interval, $-2\Delta v \le v \le 0$, $w^{(2)}(v)$ is defined by symmetry. This weighting function conserves particles, momentum, and energy. The functions $w^{(1)}(v)$ and $w^{(2)}(v)$ are shown in Fig. A.1.

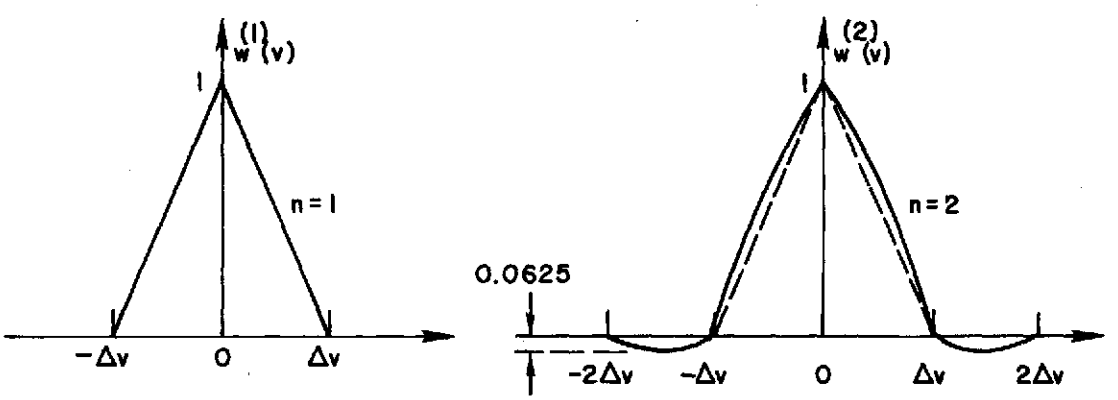

FIG. A.1. Linear (n = 1) and quadratic (n = 2) weighting functions. (Adapted from Fig. 3 of Ref. 6.).

REFERENCES

1. G. Knorr, Z. Naturforsch. 18a, 1304 (1963).
2. P. J. Kellogg, Phys. Fluids 8, 102 (1965).
3. T. P. Armstrong, Phys. Fluids 10, 1269 (1967).
4. O. Buneman, Phys. Rev. 115, 503 (1959).
5. J. M. Dawson, Phys. Fluids 5, 445 (1962).
6. J. Denavit, J. Comp. Phys. 9, 75 (1972).
7. R. D. Richtmyer and K. W. Morton, Difference Methods for Initial Value Problems (Wiley-Interscience, New York, N. Y. 1967).
8. J. A. Byers and J. Killeen, in Methods in Computational Physics, edited by B. Alder, S. Fernbach, and M. Rotenberg (Academic Press, New York, N. Y., 1970), Vol. 9, p. 135.
9. K. Estabrook, Proc. Sixth Conference on Numerical Simulation of Plasmas, July 1973, Lawrence Livermore Laboratory Report CONF-730804, Berkeley, California, p. 13.
10. T. P. Armstrong, R. C. Harding, G. Knorr, and D. Montgomery, in Methods in Computational Physics, edited by B. Alder, S. Fernbach, and M. Rotenberg (Academic Press, New York, N. Y., 1970), Vol. 9, p. 29.
11. J. Denavit and W. L. Kruer, Phys. Fluids 14, 1782 (1971).
12. T. P. Armstrong and D. Montgomery, Proc. APS Topical Conference on Numerical Simulation of Plasma, September 1968, Los Alamos Scientific Laboratory Report No. LA-3990, Los Alamos, New Mexico, p. A3-1.
13. F. C. Grant and M. R. Feix, Phys. Fluids 10, 696 (1967).

14. A. Ralston and H. S. Wilf, Mathematical Methods for Digital Computers, (Wiley, New York, N. Y. 1960).

15. G. Joyce, G. Knorr, and H. K. Meier, J. Comp. Phys. 8, 53 (1971).

16. P. Burger, D. A. Dunn, and A. S. Halsted, Phys. Fluids 8, 2263 (1965).

17. R. W. Hockney, Phys. Fluids 9, 1826 (1966).

18. R. W. Hockney, Stanford University Institute for Plasma Research Report No. 53 (May 1966).

19. C. K. Birdsall and D. Fuss, J. Comp. Phys. 3, 494 (1969).

20. R. L. Morse and C. W. Nielson, Phys. Fluids 12, 2418 (1969).

21. R. L. Morse, in Methods in Computational Physics, edited by B. Alder, S. Fernbach, and M. Rotenberg (Academic Press, New York, N. Y., 1970), Vol. 9, p. 213.

22. J. M Dawson, C. G. Hsi, and R. Shanny, Proc. APS Topical Conference on Numerical Simulation of Plasma, September 1968, Los Alamos Scientific Laboratory Report No. LA-3990, Los Alamos, New Mexico, p. A1-1.

23. J. M. Dawson, in Methods in Computational Physics, edited by B. Alder, S. Fernbach, and M. Rotenberg (Academic Press, New York, N. Y., 1970), Vol. 9, p. 1.

24. W. L. Kruer and J. M. Dawson, Proc. Third Annual Numerical Plasma Simulation Conference, September 1969, Stanford University, Stanford, California.

25. H. R. Lewis, J. Comp. Phys. 6, 136 (1970).

26. H. R. Lewis, in Methods in Computational Physics, edited by B. Alder, S. Fernbach, and M. Rotenberg (Academic Press, New York, N. Y., 1970), Vol. 9, p. 307.

27. P. Burger, Stanford Electronics Laboratory Technical Report No. 0254-1 (April 1964).

28. C. W. Barnes, Stanford University Institute for Plasma Research Report No. 344 (March 1970).

29. A. B. Langdon and C. K. Birdsall, Phys. Fluids 13, 2115 (1970).

30. W. M. Gentleman and G. Sande, Proc. American Federation of Information Processing Societies, 1966 Fall Joint Computer Conference, (Spartan Books, New York, N. Y., 1966), Vol. 29, p. 563.

31. A. B. Langdon, J. Comp. Phys. 6, 247 (1970).

32. B. D. Fried and S. D. Conte, The Plasma Dispersion Function, (Academic Press, New York, N. Y., 1961).

33. A. B. Langdon, University of California, Berkeley, Electronics Research Laboratory, Second Quarterly Progress Report on Plasma Research, 1969.

34. H. Okuda, Phys. Fluids 15, 1268 (1972).

35. H. Okuda, J. Comp. Phys. 10, 475 (1972).

36. P. C. Clemmow and J. P. Dougherty, Electrodynamics of Particles and Plasmas (Addison-Wesley Publishing Company, Reading, Mass., 1969), p. 405.

37. J. A. Byers, Proc. Fourth Conference on Numerical Simulation, November 1970, Naval Research Laboratory, Washington, D. C., p. 496.

38. J. M. Dawson, Phys. Rev. 118, 381 (1960).

39. L. D. Landau, J. Phys. (USSR) 10, 25 (1946).

40. J. Canosa, and J. Gazdag, Proc. Sixth Conference on Numerical Simulation of Plasmas, July 1973, Lawrence Livermore Laboratory Report No. CONF-730804, Berkeley, California, p. 104.

41. H. R. Lewis, Phys. Fluids 15, 103 (1972).

42. T. P. Armstrong and C. W. Nielson, Phys. Fluids 13, 1880 (1970).

43. J. H. Malmberg and C. B. Wharton, Phys. Rev. Letters 13, 184 (1964).

44. G. Van Hoven, Phys. Rev. Letters 17, 169 (1966).

45. H. Derfler and T. C. Simonen, Phys. Rev. Letters 17, 172 (1966).

46. J. H. Malmberg and C. B. Wharton, Phys. Rev. Letters 17, 175 (1966).

47. A. Y. Wong, R. W. Motley, and N. D'Angelo, Phys. Rev. 133A, 436 (1964).

48. T. M. O'Neil, Phys. Fluids 8, 2255 (1965).

49. L. M. Al'tshul and V. I. Karpman, Sov. Phys. JETP 22, 361 (1966).

50. V. L. Bailey and J. Denavit, Phys. Fluids 13, 451 (1970).

51. S. P. Gary, Phys. Fluids 10, 570 (1967).

52. R. Sugihara and T. Kamimura, J. Phys. Soc. Japan 33, 206 (1972).

53. I. H. Oei and D. G. Swanson, Phys. Fluids 15, 2218 (1972).

54. J. H. Malmberg and C. B. Wharton, Phys. Rev. Letters 19, 775 (1967).

55. A. Lee and G. Schmidt, Phys. Fluids 13, 2546 (1970).

56. R. N. Franklin, S. M. Hamberger, and G. J. Smith, Phys. Rev. Letters 29, 914 (1972).

57. W. L. Kruer, J. M. Dawson, and R. N. Sudan, Phys. Rev. Letters 23, 838 (1969).

58. J. M. Dawson and R. Shanny, Phys. Fluids 11, 1506 (1968).

59. W. M. Manheimer and R. W. Flynn, Phys. Fluids 14, 2393 (1971).

60. G. J. Morales and T. M. O'Neil, Phys. Rev. Letters 28, 417 (1972).

61. R. L. Dewar, Phys. Fluids 15, 712 (1972).

62. A. Lee and G. Pocobelli, Phys. Fluids 15, 2351 (1972).

63. W. E. Drummond and D. Pines, Nucl. Fusion Suppl. Pt. 3, 1049 (1962).

64. A. A. Vedenov, E. P. Velikhov, and R. Z. Sagdeev, Nucl. Fusion Suppl. Pt. 2, 465 (1962).

65. I. B. Bernstein, J. M. Green, and M. D. Kruskal, Phys. Rev. 108, 546 (1957).

66. C. B. Wharton, J. H. Malmberg, and T. M. O'Neil, Phys. Fluids 11, 1761 (1968).

67. M. V. Goldman, Phys. Fluids 13, 1281 (1970).

68. M. V. Goldman and H. L. Berk, Phys. Fluids 14, 801 (1971).

69. H. V. Wong, Phys. Fluids 15, 632 (1972).

70. K. Mima and K. Nishikawa, J. Phys. Soc. Japan 30, 1722 (1971).

71. K. Mima and K. Nishikawa, J. Phys. Soc. Japan 33, 1669 (1972).

72. V. D. Shapiro and V. I. Shevchenko, Sov. Phys. JETP 30, 1121 (1970).

73. N. I. Bud'ko, V. I. Karpman, and D. R. Shklyer, Sov. Phys. JETP 34, 778 (1972).

74. W. M. Manheimer, Phys. Rev. 3, A1402 (1971).

75. T. Yagishita and Y. H. Ichikawa, J. Phys. Soc. Japan 28, 1559 (1970).

76. A. L. Brinca, J. Plasma Phys. 7, 385 (1972).

77. R. N. Franklin, S. M. Hamberger, H. Ikezi, G. Lampis, and G. J. Smith, Phys. Rev. Letters 28, 1114 (1972).

78. G. Jahns and G. Van Hoven, Phys. Rev. Letters 13, 436 (1973).

79. H. Ikezi, Y. Kiwamoto, K. Nishikawa, and K. Mima, Phys. Fluids 15, 1605 (1972).

80. W. L. Kruer and J. M. Dawson, Phys. Fluids 13, 2747 (1970).

81. B. Rosen, G. Schmidt, and W. L. Kruer, Phys. Fluids 15, 2001 (1972).

82. V. D. Pfirsch, Z. Naturforsch. 17a, 861 (1962).

83. G. Jahns and G. Van Hoven, Bull. Am. Phys. Soc. 17, 1038 (1972).

84. D. F. DuBois and M. V. Goldman, Phys. Rev. 164, 207 (1967).

85. G. Van Hoven and G. Jahns, University of California, Irvine, Physics Department Report No. 73-79 (1973).

86. P. DeNeef, Phys. Rev. Letters 31, 446 (1973).

87. A. L. Brinca, Proc. XIth International Conference on Phenomena in Ionized Gases, Prague, 1973 (Czechoslovak Academy of Sciences, Prague 1973), p. 341.

88. Y. Matsuda, F. W. Crawford, and S. A. Self, Proc. XIth International Conference on Phenomena in Ionized Gases, Prague, 1973 (Czechoslovak Academy of Sciences, Prague 1973), p. 340.

89. M. Abramowitz and I. A. Stegun, Handbook of Mathematical Functions (Dover, New York, N. Y., 1965).